การวิเคราะห์รอยร้าวบริเวณใกล้ส่วนต่อประสานโดยระเบียบวิธีสมการปริพันธ์เอกฐานต่ำ

นายพิสิษฐ์ วัฒนวิทย์

วิทยานิพนธ์นี้เป็นส่วนหนึ่งของการศึกษาตามหลักสูตรปริญญาวิศวกรรมศาสตรมหาบัณฑิต
สาขาวิชาวิศวกรรมโยธา ภาควิชาวิศวกรรมโยธา
คณะวิศวกรรมศาสตร์ จุฬาลงกรณ์มหาวิทยาลัย
ปีการศึกษา 2560

ANALYSIS OF NEAR INTERFACE CRACKS BY WEAKLY SINGULAR BOUN DARY INTEGRAL EQUATION METHOD

Mr. Pisit Watanavit

A Thesis Submitted in Partial Fulfillment of the Requirements
for the Degree of Master of Engineering Program in Civil Engineering
Department of Civil Engineering
Faculty of Engineering
Chulalongkorn University
Academic Year 2017

Thesis Title	ANALYSIS OF NEAR INTERFACE CRACKS BY WEAKLY SINGULAR BOUNDARY INTEGRAL EQUATION METHOD
By	Mr. Pisit Watanavit
Field of Study	Civil Engineering
Thesis Advisor	Associate Professor Jaroon Rungamornrat, Ph.D.
Thesis Co-Advisor	Assistant Professor Watanachai Smittakorn, Ph.D.

Accepted by the Faculty of Engineering, Chulalongkorn University in Partial Fulfillment of the Requirements for the Master's Degree

.....Dean of the Faculty of Engineering
(Associate Professor Supot Teachavorasinskun, Ph.D.)

THESIS COMMITTEE

.....Chairman
(Professor Teerapong Senjuntichai, Ph.D.)
.....Thesis Advisor
(Associate Professor Jaroon Rungamornrat, Ph.D.)
.....Thesis Co-Advisor
(Assistant Professor Watanachai Smittakorn, Ph.D.)
.....Examiner
(Associate Professor Akhrawat Lenwari, Ph.D.)
.....External Examiner
(Assistant Professor Kitjapat Phuvoravan, Ph.D.)

พิสิษฐ์ วัฒนวิทย์ : การวิเคราะห์รอยร้าวบริเวณใกล้ส่วนต่อประสานโดยระเบียบวิธีสมการปริพันธ์เอกฐานต่ำ (ANALYSIS OF NEAR INTERFACE CRACKS BY WEAKLY SINGULAR BOUNDARY INTEGRAL EQUATION METHOD) อ.ที่ปรึกษาวิทยานิพนธ์หลัก: รศ. ดร. จรูญ รุ่งอมรรัตน์, อ.ที่ปรึกษาวิทยานิพนธ์ร่วม: ผศ. ดร. วัฒนชัย สมิทธากร, 74 หน้า.

วิทยานิพนธ์นี้นำเสนอระเบียบวิธีสมการปริพันธ์พื้นผิวเอกฐานต่ำสำหรับวิเคราะห์รอยร้าวใกล้ผิวรอยต่อในตัวกลางยืดหยุ่นเชิงเส้นหลายวัสดุสามมิติ สมการกำกับสร้างขึ้นภายใต้กรอบทั่วไปทำให้สามารถจำลองวัตถุที่มีขอบเขตจำกัด วัสดุที่มีคุณสมบัติขึ้นกับทิศทาง เงื่อนไขแรงกระทำ รูปร่างรอยร้าว และลักษณะผิวรอยต่อวัสดุใดๆได้ ระบบสมการปริพันธ์ซึ่งกำกับข้อมูลไม่ทราบค่าบนขอบเขตของวัตถุ ผิวรอยร้าว และผิวรอยต่อวัสดุสามารถพัฒนาโดยใช้สมการปริพันธ์รูปแบบอ่อนเอกฐานต่ำสำหรับการเปลี่ยนตำแหน่งและแรงพื้นผิวและความต่อเนื่องบนผิวรอยต่อวัสดุ ระเบียบวิธีบาวดารีแบบสมมาตรกาเลอคินและระเบียบวิธีไฟไนต์เอลิเมนต์พื้นฐานถูกพัฒนาขึ้นเพื่อหาผลเฉลยของระบบสมการปริพันธ์ดังกล่าว โดยใช้การประมาณแบบพิเศษสำหรับผลเฉลยของการเคลื่อนที่สัมพัทธ์ของผิวรอยร้าวบริเวณขอบรอยร้าว ข้อมูลบนผิวรอยร้าวที่ได้นำมาใช้ในการคำนวณหาค่าตัวประกอบความเข้มของหน่วยแรงและหน่วยแรงทีตามแนวขอบรอยร้าว ผลเฉลยในกรณีต่างๆถูกนำเสนอเพื่อแสดงให้เห็นถึงความถูกต้อง การลู่เข้าของคำตอบ และสมมรถนะของระเบียบวิธีที่นำเสนอ รวมทั้งเพื่อศึกษาอิทธิพลของความบึ่งแกร่งของวัสดุและระยะห่างจากผิวรอยต่อวัสดุที่มีต่อข้อมูลรอยร้าว

ภาควิชา วิศวกรรมโยธา	ลายมือชื่อนิสิต .....
สาขาวิชา วิศวกรรมโยธา	ลายมือชื่อ อ.ที่ปรึกษาหลัก .....
ปีการศึกษา 2560	ลายมือชื่อ อ.ที่ปรึกษาร่วม .....

5870209521 : MAJOR CIVIL ENGINEERING
KEYWORDS: ANISOTROPY, BIEM, BI-MATERIALS, STRESS INTENSITY FACTORS, SUB-INTERFACE CRACKS

PISIT WATANAVIT: ANALYSIS OF NEAR INTERFACE CRACKS BY WEAKLY SINGULAR BOUNDARY INTEGRAL EQUATION METHOD. ADVISOR: ASSOC. PROF. JAROON RUNGAMORNRAT, Ph.D., CO-ADVISOR: ASST. PROF. WATANACHAI SMITTAKORN, Ph.D., 74 pp.

This thesis presents a weakly singular boundary integral equation method for analysis of sub-interface cracks in a three-dimensional, linearly elastic, multi-material domain. The formulation is established in a general framework allowing finite bodies, general material anisotropy and loading conditions, arbitrarily shaped cracks, and curved material interface to be treated. A system of integral equations governing the unknown data on the boundary, the crack surface and the material interface are established using a pair of weakly singular, weak-form displacement and traction integral equations and the continuity along the material interface. A symmetric Galerkin boundary element method together with the standard finite element technique is implemented to solve the governing integral equations. Special near-front approximation is employed to enhance the approximation of the relative crack-face displacement in the neighborhood of the crack front. The solved crack-face data is then used to post-process for the stress intensity factors and the T-stress along the crack front. A selected set of results is presented not only to demonstrate the accuracy, convergence and capability of the proposed technique but also to explore the influence of the material stiffness and the distance to the material interface on the fracture data along the crack front.

Department:	Civil Engineering	Student's Signature	.....
Field of Study:	Civil Engineering	Advisor's Signature	.....
Academic Year:	2017	Co-Advisor's Signature	.....

ACKNOWLEDGEMENTS

Firstly, my thesis advisor, Assoc. Prof. Dr. Jaroon Rungamornrat who supports my work. His support help me check step by step to verifying and correct my work until its finish. Secondly, my co-advisor, Asst. Prof. Dr. Watanachai Smittakorn who give advice about the writing report and listen about detail in technique. I also want to thank all the previous thesis allowing me to use their works as a reference and information towards the study of my thesis. Many friends stay with me and listening to my work. Importantly, thank you for my family. My lovely family encourage. I'm proud that I'm one of my family. Finally, the authors gratefully acknowledge the support provided by The Scholarship from the Graduate School, Chulalongkorn University to commemorate the 72th anniversary of his Majesty King Bhumibala Aduladeja is gratefully acknowledged and Thailand Research Fund.

CONTENTS

Page

CHAPTER 1

INTRODUCTION

The motivation and significance begins first and then the background and review of relevant literature concerning modeling and analysis of fractures in linear elastic media constituting dissimilar materials are presented. Next, the research objective, scope of work, methodology, and research procedure are briefly addressed. Finally, the outcome and key contribution of the present work are concluded.

1.1 MOTIVATION AND SIGNIFICANCE

Bi-materials or multi-materials are examples of advanced materials combining advantages of two or more constituents joining at the interface. These materials have been increasingly and widely employed in various applications in both engineering and industrial sectors due to their desirable mechanical properties, high strength to weight ratio, and high resistance to severe environmental conditions such as temperature rises, high humidity, corrosions and chemical attacks. With such positive features, this class of materials can therefore be commonly found in the fabrication of either modern structures such as components and parts of aerospace structures and automobiles or conventional structures such as dissimilar metal welded joints in steel structures and pavement layers of roads and highways (see Figure 1.1). Besides their advantages, understanding of the damage and failure mechanism of those materials has been found an essential component in the design to ensure the integrity and safety of the components and parts throughout their lifespan usage. Most of bi-materials and multi-materials have been found prone to fractures especially in regions near the material interfaces. For instance, fiber reinforced ceramics, which are commonly used under the high temperature condition, possess the brittle failure characteristic and low fracture toughness. During applications, cracks can initiate in the ceramic matrix near the material interface, then propagate towards the interface, and finally induce the interfacial delamination and fracture of fibers (see Figure 1.2). Another example is welded

joints in steel structures. The high temperature induced during the welding process can cause the high residual stress and cracking developed within the welding zone, and it generally leads to the brittle failure mechanism. To simulate the fracture-induced failure mechanism of bi-materials and multi-materials especially near the material interface, it still requires the development of physically sound governing physics capable of modeling complexity involved and the efficient and powerful solution procedures to ensure the applications of the mathematical model in a broad setting.

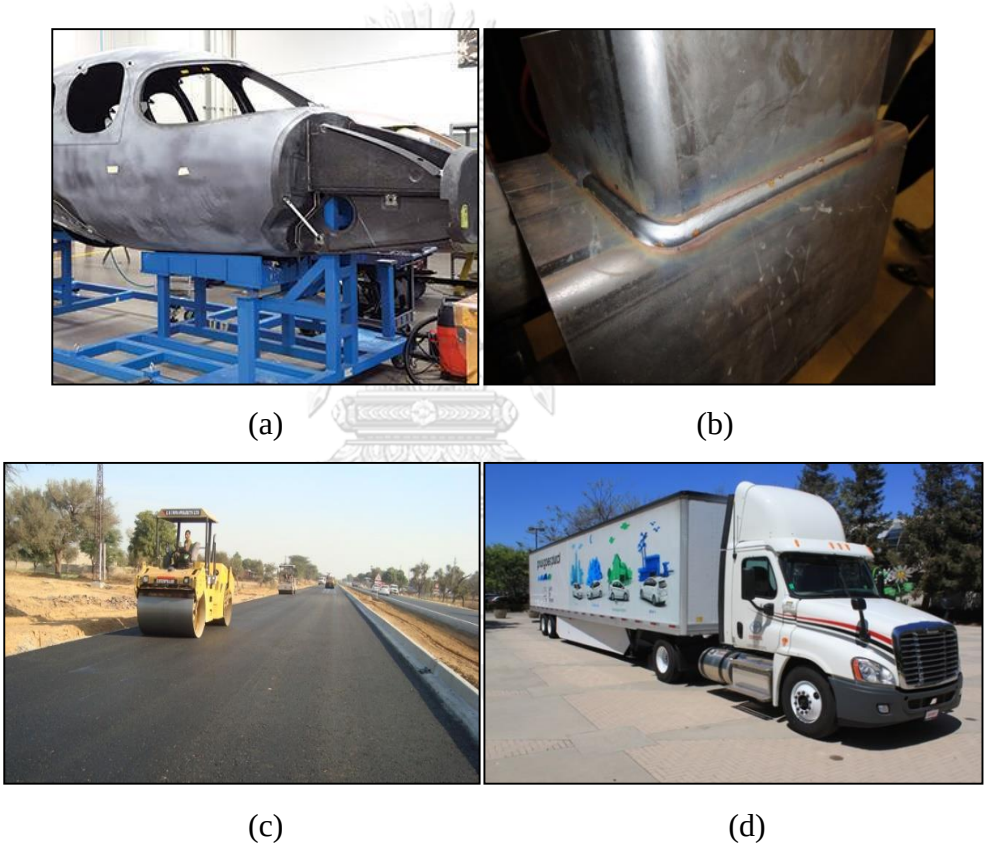

(a) (b)

(c) (d)

Figure 1.1: Application of bi-materials and multi-materials: (a) components and parts of aircrafts, (b) welded joints of steel structures, (c) pavement layers, and (d) automobiles

Studies of fracture characteristics of dissimilar media have been recognized in a wide range, both in terms of experimental investigations and mathematical simulations. While results obtained from laboratory tests offer the best data for inferring actual responses and behavior of physical phenomena, required resources

especially those associated with the preparation of test specimens, control of experimental settings, testing facilities, and time consumptions are quite significant and commonly pose the limitation on the testing scenarios. The mathematical modeling and simulations become an attractive alternative and have been extensively employed due to the advances of numerical analysis of computational technology. Applications of more sophisticated governing physics to capture complicated situations in a broader and larger scale have been increasingly found. The enhancement of solution procedures in terms of their computational efficiency and capability to handle problems in a general framework is therefore obligatory.

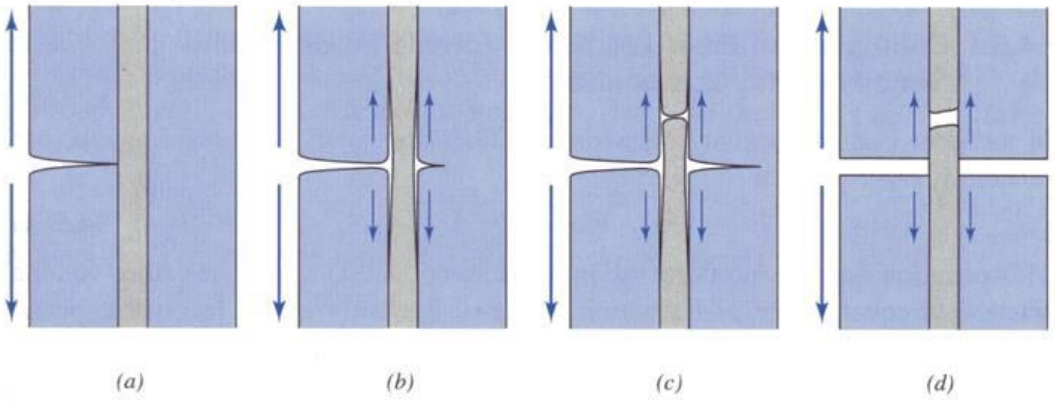

Figure 1.2: Schematics indicating the cracking behavior and failure in ceramic matrix composite (Liu, 2015)

Within the framework of linear elastic fracture mechanics (LEFM), the stress intensity factors are essential parameters providing the measure of the dominant elastic fields in a local region surrounding the crack edge. Various researchers employed the concept of LEFM to develop solution techniques for determining the stress intensity factors for cracks in dissimilar media (e.g., Lee et al., 1987; Huang and Kardomateas, 2001; Chang and Wu, 2003; Chen et al., 2005; Xiao et al., 2005; Hao, 2006; Noda et al., 2006; Rungamornrat, 2006; Chang and Xu, 2007; Yue et al., 2007; Marsavina and Sadowski, 2008; Chen et al., 2010; Tu et al., 2013; Liu, 2015). The stress intensity factors have been often utilized, as parameters in the fracture models, in the prediction the crack initiation and propagation direction. Based upon the past evidences, the influence of the non-singular part of the near-front elastic

field (e.g., T-stress representing a constant stress at the crack front) on the fracture process has also been found significant. For instance, the size and shape of the inelastic zone vicinity the crack tip affected from the T-stress, the stability of the crack growth path, and the direction of crack growth (Chen et al., 2003; Profant et al., 2008; Ševeček et al., 2012; Yu et al., 2012; Zhou et al., 2013). As a consequence, two-parameter fracture models, integrating both the stress intensity factors and the T-stress, have been increasingly used, in the past two decades, to predict the behavior and responses of the cracked media.

Boundary integral equation methods (BIEMs) have proven to be one of the most efficient numerical techniques for performing the stress analysis and determining the associated fracture data of cracks in linear elastic media. The primary advantage of this method results directly from that the key governing equations contain only unknowns on the domain boundary and crack surface. Therefore, the discretization in the solution procedure is required on a solution space of a reduced dimension. While applications of BIEMs to the analysis of cracks in a homogeneous elastic medium have been well established, work related to the modeling of cracks in dissimilar solids is relatively few. Enhancement of the techniques to be capable of handling problems in a general and broad context (e.g., material anisotropy, multi-material domains, general configurations of cracks and material interfaces, efficient and accurate post-process for various types of fracture data, etc.) still require extensive investigations.

1.2 BACKGROUND AND REVIEW

In this section, results from a careful literature survey are briefly presented not only to provide the historical breakthrough on the development of the solution procedures for obtaining both of the stress intensity factors and the T-stress for cracks in dissimilar materials but also to indicate the originality and merit of the present study. Only past studies within the framework of the classical linear elasticity and linear elastic fracture mechanics are summarized. In addition, the review focuses mainly on sub-interface cracks (i.e., cracks buried with the material near the material interface) whereas the interfacial cracks (i.e., cracks locating along the material

interface) and the cracks terminating at the materials interface are out of scope of the present study.

1.2.1 Analysis for Stress Intensity Factors

Previous researches concerning the development and use of both analytical methods and numerical schemes for determining the stress intensity factors of near interface cracks for numerous scenarios can be summarized as follows. Lee et al. (1987) analyzed an arbitrary shape of planar crack near the bi-material interface of a three dimensional, isotropic, linear elastic infinite domain. Results of the stress intensity factor were expressed in a compact form. Later, Huang and Kardomateas (2001) applied the dislocation solutions to obtain the stress intensity factors for a straight crack parallel to the material interface and the interfacial crack in an anisotropic bi-material half-plane under the crack-face traction. In their study, the free boundary normal and parallel to the material interface were considered. In the half plane with the free boundary parallel to the material interface, the mode-mixity is much smaller than that of the near interface crack whereas for the free boundary perpendicular to the material interface, the mode-I stress intensity factor is dominated and exhibits the slight dependence on the material properties. In addition, the mode-I stress intensity factor is subjected to the rapid change across the material interface. Chang and Wu (2003) proposed a modified path-independent integral and the relation between the stress intensity factors and the J-integral for determining the solution for a two-dimensional, isotropic, bi-material finite body containing a surface-breaking crack normal to and terminating at the material interface. They found that the stress intensity factors are more applicable than J-integrals because values of the integrals either vanish or approach infinity when the crack tip terminates normally at the bi-material interface. Next, Xiao et al. (2005) utilized the multi-region scheme to solve an elliptical crack normal to the material interface of a transversely isotropic, infinite, bi-material. The traction-singular elements were used in the solution procedure to capture the singularity at the crack front and the field in the surrounding region. The orientations of the elliptical crack with the major and minor axes normal to the plane of isotropy were investigated. In addition, a finite cube containing an elliptical crack was analyzed and results were then compared with the solution of

the infinite case. They also pointed out that the stress intensity factors in a finite cube are significantly larger than those in the infinite domain. Hao (2006) reported the analytical solution of the stress intensity factors for a straight crack normal to the material interface of a two-dimensional, isotropic, infinite bi-material under the plane-strain condition. In the same year, Noda et al. (2006) applied the body force technique to examine an inclined elliptical crack near a bi-material interface in a three-dimensional whole space under a uniform far-field loading. The body was made from two isotropic materials and the unknown body force densities were approximated in terms of the product between fundamental densities and polynomials. In their work, the influence of the crack aspect ratio, the material contrast and the distance from cracks to the material interface on both the value and variation of the stress intensity factors were also investigated. Rungamornrat (2006) established a regularized boundary element method to solve cracks in a three-dimensional multi-material domain. The attractive feature of his technique results from the weakly singular property of all involved integrals, the symmetry of the weak formulation, and the use of special crack-tip elements along the crack edge to discretize the near-front field. Results obtained revealed that the method can yield very accurate stress intensity factors along the crack boundary even relatively coarse meshes were employed in the simulations. Later, Chang and Xu (2007) applied the extrapolation method to solve a two-dimensional, isotropic, bi-material finite body containing an inclined, straight crack terminating at the material interface. The effect of the crack orientation with respect to the material interface was also explored. In the same year, Yue et al. (2007) established a dual boundary element method (DBEM) for analysis of a square crack contained in three-dimensional, transversely isotropic, finite and infinite bi-materials. The orientation of the square crack with respect to the plane of material isotropy was assumed arbitrary. The jump in the crack-face displacements was treated as primary unknowns on the crack face. Such unknowns obtained from the DBEM were then used to extract the stress intensity factors along the crack boundary. They found that the ordinary boundary of the cracked bi-material can have the strong influence on the value of the stress intensity factors but has insignificant effect on the variation pattern of the stress intensity factors along the crack front. Marsavina and Sadowski (2008) reported the

asymptotic stress field near the tip of an inclined straight crack terminating at the bi-material interface. The numerical simulations were carried out using the analysis software FRANC2D/L and the stress intensity factors were calculated based on the extrapolation technique. For a crack inclined to the material interface, it was shown that the singular stress field can be written as a linear combination of various modes with unequal exponents. Both Chen et al. (2010) and Tu et al. (2013) examined the near interface cracks within two-dimensional, anisotropic, infinite and finite bi-materials using a single-domain boundary integral equation method. The stress intensity factors were obtained from the near-tip displacement together with the extrapolation method. The obtained solution was then utilized together with the maximum tensile stress failure criterion to predict the crack propagation direction and path under mixed-mode loadings. Recently, Liu (2015) proposed the enriched finite element procedure to analyze a crack terminating at the material interface with an arbitrary oriented angle. The two materials were assumed homogeneous and isotropic and perfectly bonded at the material interface. The enriched crack-tip elements were developed and utilized to accurately capture the stress intensity factors along the crack edge.

1.2.2 Analysis for T-stress

Compared with those concerning the stress intensity factors, studies involving the development of solution methodology for determining the T-stress of cracks in bi-materials or multi-materials is relatively few. Some of those relevant to the present investigation are briefly summarized below. Chen et al. (2003) employed the technique based on the dislocation mechanics to investigate a crack normal to the material interface of an isotropic, finite bi-material under the traction on the outer surface. A series of Chebyshev polynomials of the first kind was employed to represent the dislocation density. They pointed out that when the crack is contained in a stiffer material, the stress intensity factor is larger than that embedded in a homogenous domain and the crack path is always stable if the T-stress is negative. Later, Profant et al. (2008) applied the method of dislocation-array to determine the T-stress of a straight crack normal to and terminating at the material interface of a bi-material. The technique was established in a general framework allowing the

material anisotropy to be considered and then further specialized to the case of the orthotropic symmetry. First, the M-type integral from the far-field deformation along with an auxiliary solution was calculated. Then the near-tip data was extracted directly from the far-field deformation to determine the T-stress. Their model offered a basis for the application of the fracture criterion at the material interface when both the deflection and the penetration at the material interface must be considered. Yu et al. (2012) employed the method of interaction integrals to obtain the T-stress of an interfacial crack in the bi-material with the complex material interface and under the traction on the outer boundary. In the same year, Ševeček et al. (2012) applied the concept of the finite fracture mechanics and the matched asymptotic expansions to study the effect of the higher-order terms in the expansion of the near-front field on the competition between the delamination at the bi-material interface between two aligned orthotropic brittle materials and the crack penetration. The crack was assumed to be oriented arbitrary to the material interface. They pointed out that the T-stress significantly affects the influence of the delamination and the penetration. In addition, it was found that the crack penetration was favored by the positive T-stress. Recently, Zhou et al. (2013) presented a set of analytical solutions for an interfacial edge crack contained in a two-dimensional, isotropic, finite bi-material. A set of Hamiltonian dual equations was derived using the Hamiltonian principle of mixed energies and the final system was solved by the method of separation of variables. The symplectic expansion method was then applied to determine both the stress intensity factors and the T-stress.

On the basis of an extensive literature survey, most of existing and relevant investigations focused principally on the calculations of the stress intensity factors. Studies regarding to the development of analytical or numerical techniques capable of calculating the T-stress along the crack front for sub-interface or near-interface cracks in three-dimensional dissimilar materials has not been well recognized. In particular, the enhancement of the weakly singular boundary integral equation method similar to that proposed by Rungamornrat (2006) to compute the T-stress of cracks in bi-materials or multi-materials has not been found and this significant gap of knowledge motivates the present investigation.

1.3 OBJECTIVE

The objectives of this research are (1) to develop a numerical technique based on the weakly singular boundary integral equation method for determining the stress intensity factors and the T-stress of near-interface cracks in a three-dimensional bi-material domain and (2) to investigate the influence of the material contrast and the distance from cracks to the material interface on the value and variation of both the stress intensity factors and T-stress along the crack front.

1.4 SCOPE OF WORK

The research is conducted within the following scope: (1) a medium occupies a finite region in a three-dimensional space and can be partitioned into several regions made of homogeneous, generally anisotropic, linearly elastic materials and perfectly bonded along the interface; (2) only bodies with pre-existing cracks located near the material interface and without intersecting the material interface is considered; (3) the process of crack initiation and crack growth is not considered; (4) the boundary of the domain including the crack surface and the material interface is assumed piecewise smooth (i.e., the set of points whose normal vector is not well-defined is of measure zero); and (5) the non-overlapping crack and body force are not considered.

1.5 METHODOLOGY AND PROCEDURE

The key focus of the present work is the development of a numerical procedure and its applications to the analysis of near-interface cracks in bi-material media. A particular numerical scheme based upon the weakly singular boundary integral equation method is developed following the scope of work indicated above and its computational performance including the accuracy and convergence is fully investigated. A brief summary of the key methodology and research procedure is given below.

(1) Basis field equations are taken from a classical theory of linear elasticity and responses of cracked bodies follow the small-scale yielding assumption in classical linear elastic fracture mechanics (e.g., Anderson, 2005).

(2) A set of completely regularized boundary integral equations governing the unknown data on the ordinary boundary and crack surface (e.g., displacements, tractions, jump in the crack-face displacements, and sum of the crack-face displacements) of a homogeneous cracked body is established following the work of Rungamornrat and Mear, 2008a and Rungamornrat and Senjuntichai, 2009.

(3) A domain decomposition technique is employed to partition the multi-material domain along the material interface into several homogeneous sub-domains. A set of weakly singular weak-form boundary integral equations for both the displacement and traction is then applied to obtain a set of weak-form equations governing unknown data on the boundary, the crack surface and the material interface for each sub-domain.

(4) Continuity of the displacements and equilibrium conditions along the material interfaces are enforced, in a strong sense, to combine all sets of governing equations for each sub-domain. The final set of governing integral equations for the entire domain is in a symmetric form and involves only unknown data on the boundary, unknown displacements and tractions on the material interfaces, and unknown jump in the crack-face displacement on the crack surface.

(5) A weakly singular boundary integral equation governing the sum of the crack-face displacements for cracks embedded within each sub-domain is established by choosing a proper choice of the test functions appearing in the weak-form displacement integral equation. This integral equation involves only the unknown data within the sub-domain.

(6) A standard procedure of weakly singular symmetric Galerkin boundary element method (e.g., Rungamornrat and Mear, 2008b) along with the special near-front approximation and the conforming discretization along the material interface (to maintain the satisfaction of the continuity and equilibrium along the material interface in a strong sense) is adopted to solve a set of governing equations established in (4). An efficient numerical quadrature for weakly singular and nearly singular double surface integrals and the evaluation of kernels for general anisotropic materials are also implemented.

(7) A set of weak-form equations established in (5) is discretized using standard Galerkin technique along with the finite element procedure to form the elementwise approximation and then solved for the sum of the crack-face displacements.

(8) The sum of and jump in the crack-face displacements on elements containing the crack front are directly post-processed to obtain the stress intensity factors and T-stresses along the crack front using formula proposed by Rungamornrat and Mear, 2008b and Pham et al., 2015a; Pham et al., 2015b.

(9) Computational procedure is implemented in a form of an in-house computer code and various scenarios are employed to verify and investigate the computational performance of the implemented code.

(10) A parametric study is carried out to study the influence of material parameters and the distance from cracks to the material interface on the values and distribution of the stress intensity factors and the T-stress along the crack front.

1.6 OUTCOME AND CONTRIBUTION

The present study offers an accurate, efficient, fully verified numerical procedure for the analysis of near interface cracks in elastic multi-material domains. The technique implemented is quite general in the sense that the general geometry of cracks, material interface and bodies, general loading conditions, and general material anisotropy are considered in the underlying formulation. In addition, both the stress intensity factors (directly related to the singular part of the near-front stress field) and the T-stress (measured of non-zero, non-singular stress along the crack front) can be obtained by the proposed technique. The proposed technique of this high capability should be a potentially useful tool in the simulations of crack growth and fracture-based fatigue and failure analysis causing by near interface cracks.

CHAPTER 2
PROBLEM FORMULATION

This chapter briefly presents the problem description, a set of basic field equations governing all involved field quantities, a set of completely regularized integral representations of the displacements, stresses, and tractions for homogeneous, linear elastic, cracked bodies, and the symmetric formulation of the key governing equations for a bi-material domain containing cracks.

2.1 PROBLEM DESCPRITION

A Cartesian coordinate system $\{\boldsymbol{O}; x_1, x_2, x_3\}$ with the origin $\boldsymbol{O}$ and the orthonormal basis $\{\boldsymbol{e}_1, \boldsymbol{e}_2, \boldsymbol{e}_3\}$ is introduced for further reference in the development presented below (i.e., x_i denotes the coordinate of any point $\boldsymbol{x}$ in the direction $\boldsymbol{e}_i$ for $i = 1, 2, 3$) and, in what follows, a standard indicial notation applies for all lower case subscripts. In addition, a comma notation $f_{,i}$ is used throughout to represent a partial derivative of the function f with respect to the coordinate x_i, i.e., $\partial f / \partial x_i$.

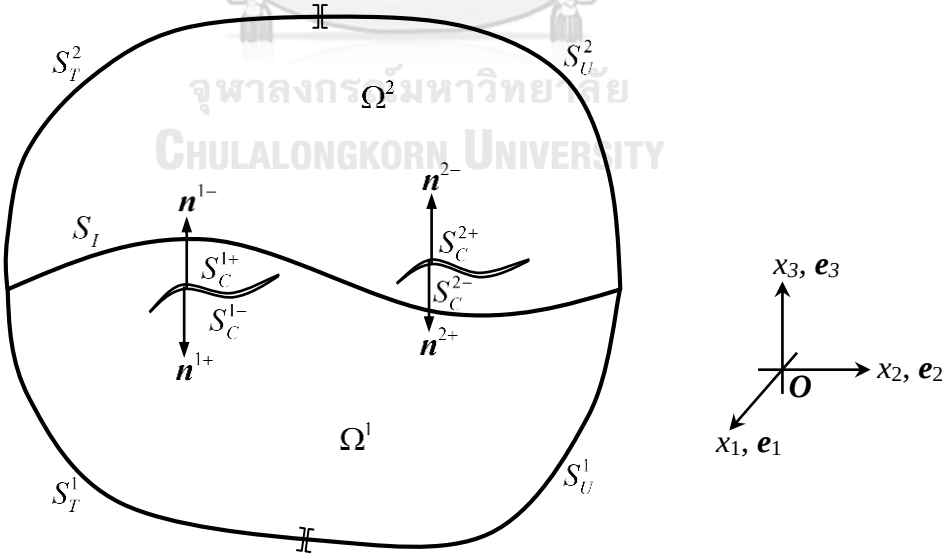

Figure 2.1: Schematic of cracked body comprising two regions made from different homogeneous linear elastic materials

Now, consider a three-dimensional, linear elastic, finite body Ω as shown in Figure 2.1. The body consists of two regions, denoted by Ω^1 and Ω^2, in which the region Ω^γ $(\gamma = 1,2)$ is made from a homogeneous, generally anisotropic, linear elastic material with the prescribed elastic constants E^γ_{ijkl} and they are perfectly bonded along the interface denoted by S_I. Here and in what follows, the superscript γ takes the value 1 and 2 and the summation is not implied for this repeated superscript. In the present study, the body is assumed to be free of the body force and only sub-interface cracks are considered (i.e., cracks intersecting or aligning with the interface S_I are not of interest). The geometry of cracks embedded in the region Ω^γ are represented by two geometrically identical, smooth surfaces $S_C^{\gamma+}$ and $S_C^{\gamma-}$. The outward unit normal vector at any point $\boldsymbol{\xi}^{\gamma+} \in S_C^{\gamma+}$ and its coincident point $\boldsymbol{\xi}^{\gamma-} \in S_C^{\gamma-}$ are denoted, respectively, by $\boldsymbol{n}^{\gamma+}$ and $\boldsymbol{n}^{\gamma-}$ and they clearly satisfy $\boldsymbol{n}^{\gamma+} = -\boldsymbol{n}^{\gamma-}$. On both crack surfaces $S_C^{\gamma+}$ and $S_C^{\gamma-}$, the traction $\boldsymbol{t}$ is fully prescribed (i.e., $\boldsymbol{t}(\boldsymbol{x}) = \boldsymbol{t}^{\gamma+}(\boldsymbol{x})\ \forall \boldsymbol{x} \in S_C^{\gamma+}$ and $\boldsymbol{t}(\boldsymbol{x}) = \boldsymbol{t}^{\gamma-}(\boldsymbol{x})\ \forall \boldsymbol{x} \in S_C^{\gamma-}$ where $\boldsymbol{t}^{\gamma+}$ and $\boldsymbol{t}^{\gamma-}$ are given functions). The ordinary boundary of the body, denoted by S_0, can be decomposed into $S_0 = S_0^1 \cup S_0^2$ where S_0^γ is the boundary of the region Ω^γ. The boundary S_0^γ can be further divided into a surface S_T^γ on which the traction $\boldsymbol{t}$ is fully prescribed (i.e., $\boldsymbol{t}(\boldsymbol{x}) = \boldsymbol{t}^{\gamma 0}(\boldsymbol{x})\ \forall \boldsymbol{x} \in S_T^\gamma$) and a surface S_U^γ on which the displacement $\boldsymbol{u}$ is fully prescribed (i.e., $\boldsymbol{u}(\boldsymbol{x}) = \boldsymbol{u}^{\gamma 0}(\boldsymbol{x})\ \forall \boldsymbol{x} \in S_U^\gamma$).

A statement of the research problem is to develop an efficient computational procedure for determining numerical solutions of the boundary value problem described above. In particular, the stress intensity factors and the T-stress along the crack front are of primary interest. In addition, the influence of the material parameters and the distance between the crack and the material interface on such fracture data along the crack front is also explored in the present study.

2.2 BASIC FIELD EQUATIONS

Mechanical responses of a three dimensional, linearly elastic body (commonly described by the displacement, strain and stress measures) can be theoretically

modeled by a classical theory of linear elasticity. From the conservation of linear and angular momentum in the absence of the body force, linear kinematics based on an infinitesimal strain theory, and linear constitutive relations, the displacement field $\boldsymbol{u} = \boldsymbol{u}(\boldsymbol{x})$, the strain field $\boldsymbol{\varepsilon} = \boldsymbol{\varepsilon}(\boldsymbol{x})$ and the stress filed $\boldsymbol{\sigma} = \boldsymbol{\sigma}(\boldsymbol{x})$ are governed by

$$\sigma_{ij}(x) = \sigma_{ji}(x), \qquad \sigma_{ij,j}(x) = 0 \tag{2.1}$$

$$\sigma_{ij}(x) = E_{ijkl}\varepsilon_{kl}(x) \tag{2.2}$$

$$\varepsilon_{ij}(x) = (u_{i,j} + u_{j,i})/2 \tag{2.3}$$

where u_i, ε_{ij} and σ_{ij} denotes components of the displacement, strain and stress referring to the coordinate system $\{\boldsymbol{O}; x_1, x_2, x_3\}$, respectively, and E_{ijkl} represents the prescribed elastic constants of a constituting material. Note that E_{ijkl} are spatially independent in the current development and essentially satisfy following symmetries $E_{ijkl} = E_{ijlk} = E_{jikl} = E_{klij}$. For the special case of isotropic materials, E_{ijkl} can be fully described by only two independent material parameters and admits a concise form

$$E_{ijkl} = \mu\left\{\delta_{ik}\delta_{jl} + \delta_{il}\delta_{jk} + \frac{2\nu}{1-2\nu}\delta_{ij}\delta_{kl}\right\} \tag{2.4}$$

where μ is the elastic shear modulus, ν is Poisson's ratio, and δ_{ij} denotes a Kronecker-delta symbol. At any point $\boldsymbol{x}$ on a smooth surface (i.e., a surface with the well-defined unit normal vector), the traction vector, denoted by $\boldsymbol{t}$, can be related to the stress at the same point by

$$t_i(x) = \sigma_{ij}(x)n_j(x) \tag{2.5}$$

where t_i and n_j are components of the traction $\boldsymbol{t}$ and a unit normal vector $\boldsymbol{n}$, respectively. A set of linear partial differential equations (2.1) and (2.3) and a set of linear algebraic equations (2.2) form the complete basic equations governing the unknown elastic fields $\boldsymbol{u} = \boldsymbol{u}(\boldsymbol{x})$, $\boldsymbol{\varepsilon} = \boldsymbol{\varepsilon}(\boldsymbol{x})$ and $\boldsymbol{\sigma} = \boldsymbol{\sigma}(\boldsymbol{x})$ for a body made of a homogeneous linearly elastic material and free of the body force.

2.3 REGULARIZED INTEGRAL EQUATIONS FOR HOMOGENEOUS DOMAIN

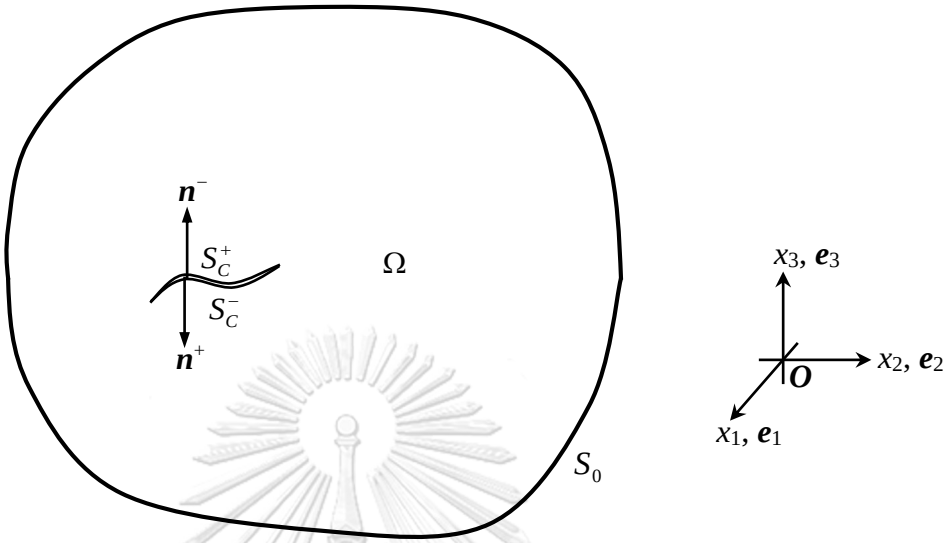

Figure 2.2 : Schematic of homogeneous, anisotropic, linearly elastic finite body containing crack

Consider a finite cracked body Ω that is made of a homogeneous, linearly elastic material and free of the body force as shown in Figure 2.2. The total boundary of the body consists of the ordinary boundary S_0 and two geometrically identical surfaces S_C^+ and S_C^-. By following the work of Rungamornrat and Mear (2008a), the boundary integral representations for the displacement and stress at any interior point $\boldsymbol{x} \in \Omega$ take the form

$$u_p(\boldsymbol{x}) = \int_S U_j^p(\boldsymbol{\xi} - \boldsymbol{x})\tau_j(\boldsymbol{\xi})dA(\boldsymbol{\xi}) - \int_S H_{ij}^p(\xi - x)\bar{n}_i(\xi)v_j(\xi)dA(\xi) + \int_S G_{mj}^p(\boldsymbol{\xi} - \boldsymbol{x})D_m v_j(\boldsymbol{\xi})dA(\boldsymbol{\xi}) \tag{2.6}$$

$$\sigma_{lk}(\boldsymbol{x}) = \varepsilon_{lrt}\frac{\partial}{\partial x_r}\left\{\int_S G_{tk}^p(\boldsymbol{\xi} - \boldsymbol{x})\tau_j(\boldsymbol{\xi})dA(\boldsymbol{\xi}) + \int_S C_{mj}^{tk}(\boldsymbol{\xi} - \boldsymbol{x})D_m v_j(\boldsymbol{\xi})dA(\boldsymbol{\xi})\right\} - \int_S H_{lk}^j(\boldsymbol{\xi} - \boldsymbol{x})\tau_j(\boldsymbol{\xi})dA(\boldsymbol{\xi}) \tag{2.7}$$

where $S = S_0 \cup S_C^+$; ε_{ism} denotes the alternating tensor; $D_m(\cdot) = n_l \varepsilon_{ism} \partial(\cdot)/\partial \xi_s$ stands for the differential operator; and the boundary and crack-face data τ_j and v_j are defined by

$$\tau_j(\boldsymbol{\xi}) = \begin{cases} t_j(\boldsymbol{\xi}), & \boldsymbol{\xi} \in S_0 \\ \Sigma t_j(\boldsymbol{\xi}) \equiv t_j^+(\boldsymbol{\xi}) + t_j^-(\boldsymbol{\xi}), & \boldsymbol{\xi} \in S_C^+ \end{cases} \tag{2.8}$$

$$v_j(\boldsymbol{\xi}) = \begin{cases} u_j(\boldsymbol{\xi}), & \boldsymbol{\xi} \in S_0 \\ \Delta u_j(\boldsymbol{y}) \equiv u_j^+(\boldsymbol{\xi}) - u_j^-(\boldsymbol{\xi}), & \boldsymbol{\xi} \in S_C^+ \end{cases} \tag{2.9}$$

in which $t_j^+(\boldsymbol{\xi})$ and $u_j^+(\boldsymbol{\xi})$ are traction and displacement components at any point $\boldsymbol{\xi} \in S_C^+$ where as $t_j^-(\boldsymbol{\xi})$ and $u_j^-(\boldsymbol{\xi})$ are traction and displacement components at its coincident point on the other crack surface S_C^-. Explicit expressions for the fundamental solutions $H_{ij}^p(\xi - x)$, $U_j^p(\boldsymbol{\xi} - \boldsymbol{x})$, $G_{mj}^p(\boldsymbol{\xi} - \boldsymbol{x})$ and $C_{mj}^{tk}(\boldsymbol{\xi} - \boldsymbol{x})$ appearing in (2.8) and (2.9) for general anisotropic, linear elastic materials are given by (see Rungamornrat and Mear (2008a) for details of derivation).

$$H_{ij}^p(\boldsymbol{\xi} - \boldsymbol{x}) = -\frac{1}{4\pi} \frac{(\xi_i - x_i)\delta_{jp}}{r^3} \tag{2.10}$$

$$U_j^p(\boldsymbol{\xi} - \boldsymbol{x}) = \frac{1}{8\pi^2 r} \oint_{\boldsymbol{z}\cdot\boldsymbol{r}=0} (\boldsymbol{z},\boldsymbol{z})_{jp}^{-1} ds(\boldsymbol{z}) \tag{2.11}$$

$$G_{ij}^p(\boldsymbol{\xi} - \boldsymbol{x}) = \varepsilon_{abm} E_{ajdc} \frac{1}{8\pi^2 r} \oint_{\boldsymbol{z}\cdot\boldsymbol{r}=0} z_b z_c (\boldsymbol{z},\boldsymbol{z})_{dp}^{-1} ds(\boldsymbol{z}) \tag{2.12}$$

$$C_{mj}^{tk}(\boldsymbol{\xi} - \boldsymbol{x}) = A_{mjdn}^{tkoe} \frac{1}{8\pi^2 r} \oint_{\boldsymbol{z}\cdot\boldsymbol{r}=0} z_o z_d (\boldsymbol{z},\boldsymbol{z})_{en}^{-1} ds(\boldsymbol{z}), \quad A_{mjdn}^{tkoe} = \varepsilon_{pam}\varepsilon_{pbt}\left(E_{bknd}E_{ajeo} - \frac{1}{3}E_{ajkb}E_{dneo} \right) \tag{2.13}$$

where $\boldsymbol{r} = \boldsymbol{\xi} - \boldsymbol{x}$; $r = \|\boldsymbol{r}\|$; $\boldsymbol{z}$ denotes a unit vector defined on a plane perpendicular to the position vector $\boldsymbol{r}$; $(\boldsymbol{z},\boldsymbol{z})$ is a matrix whose entries are defined by $(\boldsymbol{z},\boldsymbol{z})_{jp} = z_i E_{ijpl} z_l$; $(\boldsymbol{z},\boldsymbol{z})^{-1}$ is the inverse of $(\boldsymbol{z},\boldsymbol{z})$; and the line integrals appearing in (2.11)-(2.13) are defined along a unit circle on the plane $\boldsymbol{z}\cdot\boldsymbol{r} = 0$. It is evident from above expressions that the function $H_{ij}^p(\xi - x)$ is independent of the material properties and singular

only at $\boldsymbol{\xi} = \boldsymbol{x}$ of $\mathcal{O}(r^{-2})$ whereas $U_j^p(\boldsymbol{\xi} - \boldsymbol{x})$, $G_{mj}^p(\boldsymbol{\xi} - \boldsymbol{x})$ and $C_{mj}^{tk}(\boldsymbol{\xi} - \boldsymbol{x})$ are material dependent and singular only at $\boldsymbol{\xi} = \boldsymbol{x}$ of $\mathcal{O}(r^{-1})$. For the special case of isotropic materials, the functions $U_j^p(\boldsymbol{\xi} - \boldsymbol{x})$, $G_{mj}^p(\boldsymbol{\xi} - \boldsymbol{x})$ and $C_{mj}^{tk}(\boldsymbol{\xi} - \boldsymbol{x})$ admit the following closed-form expressions (also see the work of Li et al. (1998) and Rungamornrat and Mear (2008a))

$$U_j^p(\boldsymbol{\xi} - \boldsymbol{x}) = \frac{1}{16\pi(1-\nu)\mu r}\left[(3-4\nu)\delta_{pj} + \frac{(\xi_p - x_p)(\xi_j - x_j)}{r^2}\right] \tag{2.14}$$

$$G_{mj}^p(\boldsymbol{\xi} - \boldsymbol{x}) = \frac{1}{8\pi(1-\nu)r}\left[(1-2\nu)\varepsilon_{mpj} + \frac{(\xi_p - x_p)(\xi_a - x_a)}{r^2}\varepsilon_{ajm}\right] \tag{2.15}$$

$$C_{mj}^{tk}(\boldsymbol{\xi} - \boldsymbol{x}) == \frac{\mu}{4\pi(1-\nu)r}\left[(1-\nu)\delta_{tk}\delta_{mj} + 2\nu\delta_{km}\delta_{tj} - \delta_{kj}\delta_{tm} - \frac{(\xi_k - x_k)(\xi_j - x_j)}{r^2}\delta_{tm}\right] \tag{2.16}$$

where μ and ν are elastic shear modulus and Poisson ratio, respectively, and δ_{ij} denotes a standard Kronecker-delta symbol. The boundary integral relations (2.6) and (2.7) can be employed to post-process for the displacement and stress at any point within the body provided that the unknown data on the boundary and crack surface are determined.

To form a set of boundary integral equations governing all unknown information on the total boundary of the whole body, a procedure similar to that proposed by Rungamornrat and Mear (2008a) is utilized. For instance, the displacement boundary integral equation is established by first taking limit $\boldsymbol{x} \to \boldsymbol{y} \in S$ of (2.6) and then establishing the weak form via the standard weighted residual technique. Similarly, the traction boundary integral equation is formed by first using (2.7) to form a product $\sigma_{lk}(\boldsymbol{x})n_l(\boldsymbol{y})$ and taking the limit $\boldsymbol{x} \to \boldsymbol{y} \in S$ to obtain the traction boundary integral equation, then casting the weak form via the standard weighted residual technique, and finally performing the integration by parts to regularize all integrals containing strongly singular kernels. A final pair of weak-form displacement and traction boundary integral equations is given by

$$\frac{1}{2}\int_S \tilde{t}_p(\boldsymbol{y})\bar{v}_p(\boldsymbol{y})dA(\boldsymbol{y}) = \int_S \tilde{t}_p(\boldsymbol{y})\int_S U_j^p(\boldsymbol{\xi}-\boldsymbol{y})\tau_j(\boldsymbol{\xi})dA(\boldsymbol{\xi})dA(\boldsymbol{y})$$
$$-\int_S \tilde{t}_p(\boldsymbol{y})\int_S H_{ij}^p(\boldsymbol{\xi}-\boldsymbol{y})n_i(\boldsymbol{\xi})v_j(\boldsymbol{\xi})dA(\boldsymbol{\xi})dA(\boldsymbol{y}) \qquad (2.17)$$
$$+\int_S \tilde{t}_p(\boldsymbol{y})\int_S G_{mj}^p(\boldsymbol{\xi}-\boldsymbol{y})D_m v_j(\boldsymbol{\xi})dA(\boldsymbol{\xi})dA(\boldsymbol{y})$$

$$\frac{1}{2}\int_S \tilde{v}_k(\boldsymbol{y})\bar{\tau}_k(\boldsymbol{y})dA(\boldsymbol{y}) = -\int_S D_t\tilde{v}_k(\boldsymbol{y})\int_S C_{mj}^{tk}(\boldsymbol{\xi}-\boldsymbol{y})D_m v_j(\boldsymbol{\xi})dA(\boldsymbol{\xi})dA(\boldsymbol{y})$$
$$-\int_S D_t\tilde{v}_k(\boldsymbol{y})\int_S G_{tk}^j(\boldsymbol{\xi}-\boldsymbol{y})\tau_j(\boldsymbol{\xi})dA(\boldsymbol{\xi})dA(\boldsymbol{y}) \qquad (2.18)$$
$$-\int_S \tilde{v}_k(\boldsymbol{y})\int_S H_{ik}^j(\boldsymbol{\xi}-\boldsymbol{y})n_i(\boldsymbol{y})\tau_j(\boldsymbol{\xi})dA(\boldsymbol{\xi})dA(\boldsymbol{y})$$

where $\tilde{t}_p$ and $\tilde{v}_k$ are sufficiently smooth test functions rendering the integrability of all involved integrals and $\bar{v}_p$ and $\bar{\tau}_k$ are data on the boundary and crack surface defined by

$$\bar{v}_j(\boldsymbol{y}) = \begin{cases} u_j(\boldsymbol{y}), & \boldsymbol{y}\in S_0 \\ \Sigma u_j(\boldsymbol{y}) \equiv u_j^+(\boldsymbol{y}) + u_j^-(\boldsymbol{y}), & \boldsymbol{y}\in S_C^+ \end{cases} \qquad (2.19)$$

$$\tau_j(\boldsymbol{y}) = \begin{cases} t_j(\boldsymbol{y}), & \boldsymbol{y}\in S_0 \\ \Delta t_j(\boldsymbol{y}) \equiv t_j^+(\boldsymbol{y}) - t_j^-(\boldsymbol{y}), & \boldsymbol{y}\in S_C^+ \end{cases} \qquad (2.20)$$

It is important to remark that both the displacement and traction integral equations (2.17) and (2.18) contain only weakly singular kernels of $\mathcal{O}(r^{-1})$ and all involved integrals are integrable in the sense of Riemann. In addition, the displacement integral equation (2.17) contains the displacement u_j and traction t_j on the ordinary boundary S_0, the sum of the crack-face displacement Σu_j, relative crack-face displacement Δu_j, and the sum of the crack-face traction Σt_j whereas the traction integral equation (2.18) contains the displacement u_j and traction t_j on the ordinary boundary S_0, the sum of the crack-face traction Σt_j, the jump in the crack-face traction Δt_j, and the relative crack-face displacement Δu_j. .

2.4 SYMMETRIC FORMULATION FOR CRACKS IN BI-MATERIAL DOMAIN

A pair of weak-form displacement and traction boundary integral equations obtained in the previous section is utilized along with the domain decomposition technique and continuity along the material interface to form the governing integral equations for a bi-material domain containing cracks as shown in Figure 2.1. The procedure utilized here follows directly those proposed by Rungamornrat (2006)

First, the body Ω is partitioned along the material interface S_I into two sub-regions Ω^1 and Ω^2 as shown in Figure 2.3. The total boundary of each sub-region Ω^γ $(\gamma = 1,2)$ consists of the crack surfaces $S_C^{\gamma+}, S_C^{\gamma-}$ and the ordinary boundary including the surface S_T^γ on which the traction is fully prescribed, the surface $S_U^\gamma = S_0^\gamma - S_T^\gamma$ on which the displacement is fully prescribed, and the interface S_I^γ on which both the displacement and traction are unknown a priori. Remark in particular that the interfaces S_I^1 and S_I^2 resulting from the partition have the same geometry as that of the material interface S_I but possess the opposite outward unit normal vector (i.e., $\boldsymbol{n}_I^1 = -\boldsymbol{n}_I^2$).

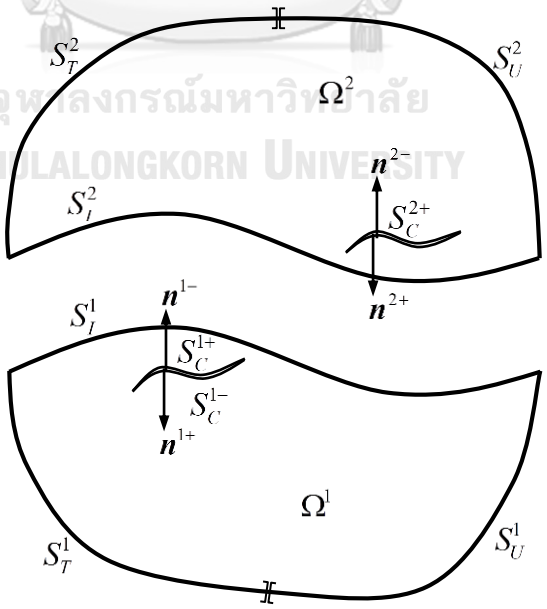

Figure 2.3: Schematic of two sub-regions resulting from partitioning of bi-material domain containing cracks shown in Figure 2.1

To establish the governing integral equations for each sub-region Ω^γ $(\gamma = 1,2)$, the weak-form displacement boundary integral equation (2.17) is utilized along the interface S_I^γ and the boundary on which the displacement is fully prescribed whereas the weak-form traction boundary integral equation (2.18) is employed along the interface S_I^γ and the boundary and crack surface on which the traction is known. More specifically, following procedures are employed: (i) apply (2.17) to S_U^γ with $\tilde{t}_p = 0$ on $S_T^\gamma \cup S_I^\gamma \cup S_C^{\gamma+}$, (ii) apply (2.18) to S_T^γ with $\tilde{v}_k = 0$ on $S_U^\gamma \cup S_I^\gamma \cup S_C^{\gamma+}$, (iii) apply (2.18) to $S_C^{\gamma+}$ with $\tilde{v}_k = 0$ on $S_U^\gamma \cup S_T^\gamma \cup S_I^\gamma$, (iv) apply (2.17) to S_I^γ with $\tilde{t}_p = 0$ on $S_T^\gamma \cup S_U^\gamma \cup S_C^{\gamma+}$, and (v) apply (2.18) to S_I^γ with $\tilde{v}_k = 0$ on $S_U^\gamma \cup S_T^\gamma \cup S_C^{\gamma+}$. A final set of weak-form boundary integral equations is given by

$$
\begin{aligned}
&\mathcal{A}_{UU}^\gamma(\tilde{\boldsymbol{t}}^\gamma,\boldsymbol{t}^\gamma)+\mathcal{B}_{UT}^\gamma(\tilde{\boldsymbol{t}}^\gamma,\boldsymbol{u}^\gamma)+\mathcal{B}_{UC}^\gamma(\tilde{\boldsymbol{t}}^\gamma,\Delta\boldsymbol{u}^\gamma)+\mathcal{A}_{UI}^\gamma(\tilde{\boldsymbol{t}}^\gamma,\boldsymbol{t}_I^\gamma)+\mathcal{B}_{UI}^\gamma(\tilde{\boldsymbol{t}}^\gamma,\boldsymbol{u}_I^\gamma)=\mathcal{R}_U^\gamma(\tilde{\boldsymbol{t}}^\gamma)\\
&\mathcal{B}_{UT}^\gamma(\boldsymbol{t}^\gamma,\tilde{\boldsymbol{v}}^\gamma)+\mathcal{C}_{TT}^\gamma(\tilde{\boldsymbol{v}}^\gamma,\boldsymbol{u}^\gamma)+\mathcal{C}_{TC}^\gamma(\tilde{\boldsymbol{v}}^\gamma,\Delta\boldsymbol{u}^\gamma)+\mathcal{B}_{IT}^\gamma(\boldsymbol{t}_I^\gamma,\tilde{\boldsymbol{v}}^\gamma)+\mathcal{C}_{TI}^\gamma(\tilde{\boldsymbol{v}}^\gamma,\boldsymbol{u}_I^\gamma)=\mathcal{R}_T^\gamma(\tilde{\boldsymbol{v}}^\gamma)\\
&\mathcal{B}_{UC}^\gamma(\boldsymbol{t}^\gamma,\tilde{\boldsymbol{v}}^\gamma)+\mathcal{C}_{TC}^\gamma(\tilde{\boldsymbol{v}}^\gamma,\boldsymbol{u}^\gamma)+\mathcal{C}_{CC}^\gamma(\tilde{\boldsymbol{v}}^\gamma,\Delta\boldsymbol{u}^\gamma)+\mathcal{B}_{IC}^\gamma(\boldsymbol{t}_I^\gamma,\tilde{\boldsymbol{v}}^\gamma)+\mathcal{C}_{CI}^\gamma(\tilde{\boldsymbol{v}}^\gamma,\boldsymbol{u}_I^\gamma)=\mathcal{R}_C^\gamma(\tilde{\boldsymbol{v}}^\gamma)\\
&\mathcal{A}_{IU}^\gamma(\tilde{\boldsymbol{t}}_I^\gamma,\boldsymbol{t}^\gamma)+\mathcal{B}_{IT}^\gamma(\tilde{\boldsymbol{t}}_I^\gamma,\boldsymbol{u}^\gamma)+\mathcal{B}_{IC}^\gamma(\tilde{\boldsymbol{t}}_I^\gamma,\Delta\boldsymbol{u}^\gamma)+\mathcal{A}_{II}^\gamma(\tilde{\boldsymbol{t}}_I^\gamma,\boldsymbol{t}_I^\gamma)+\mathcal{B}_{II}^\gamma(\tilde{\boldsymbol{t}}_I^\gamma,\boldsymbol{u}_I^\gamma)=\mathcal{R}_U^{I\gamma}(\tilde{\boldsymbol{t}}_I^\gamma)+\mathcal{D}_I^\gamma(\tilde{\boldsymbol{t}}_I^\gamma,\boldsymbol{u}_I^\gamma)\\
&\mathcal{B}_{UI}^\gamma(\boldsymbol{t}^\gamma,\tilde{\boldsymbol{u}}_I^\gamma)+\mathcal{C}_{TI}^\gamma(\tilde{\boldsymbol{u}}_I^\gamma,\boldsymbol{u}^\gamma)+\mathcal{C}_{CI}^\gamma(\tilde{\boldsymbol{u}}_I^\gamma,\Delta\boldsymbol{u}^\gamma)+\mathcal{B}_{II}^\gamma(\boldsymbol{t}_I^\gamma,\tilde{\boldsymbol{u}}_I^\gamma)+\mathcal{C}_{II}^\gamma(\tilde{\boldsymbol{u}}_I^\gamma,\boldsymbol{u}_I^\gamma)=\mathcal{R}_T^{I\gamma}(\tilde{\boldsymbol{u}}_I^\gamma)-\mathcal{D}_I^\gamma(\tilde{\boldsymbol{u}}_I^\gamma,\boldsymbol{t}_I^\gamma)
\end{aligned}
\tag{2.21}
$$

where all involved bilinear and linear integral operators, with $p,q \in \{T,U,C,I\}$ and $\gamma \in \{1,2\}$, are defined by

$$
\mathcal{A}_{pq}^\gamma(\boldsymbol{X},\boldsymbol{Y})=\int_{S_p^\gamma} X_j(\boldsymbol{y})\int_{S_q^\gamma} U_i^j(\boldsymbol{\xi}-\boldsymbol{y})Y_i(\boldsymbol{\xi})dA(\boldsymbol{\xi})dA(\boldsymbol{y}) \tag{2.22}
$$

$$
\begin{aligned}
\mathcal{B}_{pq}^\gamma(\boldsymbol{X},\boldsymbol{Y})=&\int_{S_p^\gamma} X_k(\boldsymbol{y})\int_{S_q^\gamma} G_{mj}^k(\boldsymbol{\xi}-\boldsymbol{y})D_m Y_j(\boldsymbol{\xi})dA(\boldsymbol{\xi})dA(\boldsymbol{y})\\
&-\int_{S_p^\gamma} X_k(\boldsymbol{y})\int_{S_q^\gamma} n_m(\boldsymbol{\xi})H_{mj}^k(\boldsymbol{\xi}-\boldsymbol{y})Y_j(\boldsymbol{\xi})dA(\boldsymbol{\xi})dA(\boldsymbol{y})
\end{aligned}
\tag{2.23}
$$

$$
\mathcal{C}_{pq}^\gamma(\boldsymbol{X},\boldsymbol{Y})=\int_{S_p^\gamma} D_t X_k(\boldsymbol{y})\int_{S_q^\gamma} C_{mj}^{yk}(\boldsymbol{\xi}-\boldsymbol{y})D_m Y_j(\boldsymbol{\xi})dA(\boldsymbol{\xi})dA(\boldsymbol{y}) \tag{2.24}
$$

$$
\mathcal{D}_p^\gamma(\boldsymbol{X},\boldsymbol{Y})=\frac{1}{2}\int_{S_p^\gamma} X_i(\boldsymbol{y})Y_i(\boldsymbol{y})dA(\boldsymbol{y}) \tag{2.25}
$$

$$
\mathcal{R}_U^\gamma(\tilde{\boldsymbol{t}}^\gamma)=\mathcal{D}_U^\gamma(\tilde{\boldsymbol{t}}^\gamma,\boldsymbol{u}^\gamma)-\mathcal{A}_{UT}^\gamma(\tilde{\boldsymbol{t}}^\gamma,\boldsymbol{t}^\gamma)-\mathcal{A}_{UC}^\gamma(\tilde{\boldsymbol{t}}^\gamma,\Sigma\boldsymbol{t}^\gamma)-\mathcal{B}_{UU}^\gamma(\tilde{\boldsymbol{t}}^\gamma,\boldsymbol{u}^\gamma) \tag{2.26}
$$

$$
\mathcal{R}_T^\gamma(\tilde{\boldsymbol{v}}^\gamma)=-\mathcal{D}_T^\gamma(\tilde{\boldsymbol{v}}^\gamma,\boldsymbol{t}^\gamma)-\mathcal{B}_{TT}^\gamma(\boldsymbol{t}^\gamma,\tilde{\boldsymbol{v}}^\gamma)-\mathcal{B}_{CT}^\gamma(\Sigma\boldsymbol{t}^\gamma,\tilde{\boldsymbol{v}}^\gamma)-\mathcal{C}_{TU}^\gamma(\tilde{\boldsymbol{v}}^\gamma,\boldsymbol{u}^\gamma) \tag{2.27}
$$

$$
\mathcal{R}_C^\gamma(\tilde{\boldsymbol{v}}^\gamma)=-\mathcal{D}_C^\gamma(\tilde{\boldsymbol{v}}^\gamma,\Delta\boldsymbol{t}^\gamma)-\mathcal{B}_{TC}^\gamma(\boldsymbol{t}^\gamma,\tilde{\boldsymbol{v}}^\gamma)-\mathcal{B}_{CC}^\gamma(\Sigma\boldsymbol{t}^\gamma,\tilde{\boldsymbol{v}}^\gamma)-\mathcal{C}_{CU}^\gamma(\tilde{\boldsymbol{v}}^\gamma,\boldsymbol{u}^\gamma) \tag{2.28}
$$

$$\mathcal{R}_U^{I\gamma}(\tilde{\boldsymbol{t}}_I^{\gamma}) = -\mathcal{A}_{IT}^{\gamma}(\tilde{\boldsymbol{t}}_I^{\gamma}, \boldsymbol{t}^{\gamma}) - \mathcal{A}_{IC}^{\gamma}(\tilde{\boldsymbol{t}}_I^{\gamma}, \Sigma\boldsymbol{t}^{\gamma}) - \mathcal{B}_{IU}^{r}(\tilde{\boldsymbol{t}}_I^{\gamma}, \boldsymbol{u}^{\gamma}) \tag{2.29}$$

$$\mathcal{R}_T^{I\gamma}(\tilde{\boldsymbol{u}}_I^{\gamma}) = -\mathcal{B}_{TI}^{\gamma}(\boldsymbol{t}^{\gamma}, \tilde{\boldsymbol{u}}_I^{\gamma}) - \mathcal{B}_{CI}^{\gamma}(\Sigma\boldsymbol{t}^{\gamma}, \tilde{\boldsymbol{u}}_I^{\gamma}) - \mathcal{C}_{TU}^{\gamma}(\tilde{\boldsymbol{u}}_I^{\gamma}, \boldsymbol{u}^{\gamma}) \tag{2.30}$$

By combining the boundary integral equations (2.21) for each sub-region Ω^{γ} $(\gamma = 1,2)$ and then enforcing the continuity conditions of the displacement, traction, and test functions along the interface, i.e.,

$$u_I^1 = u_I^2 \equiv u_I, \quad \tilde{u}_I^1 = \tilde{u}_I^2 \equiv \tilde{u}_I \tag{2.31}$$

$$t_I^1 = -t_I^2 \equiv t_I, \quad \tilde{t}_I^1 = -\tilde{t}_I^2 \equiv \tilde{t}_I \tag{2.32}$$

it yields a final system of boundary integral equations governing the unknown data on the boundary, the material interface, and the crack surface of cracked bi-material domains

$$\begin{array}{ccccccccccc}
\mathcal{A}_{UU}^1(\tilde{\boldsymbol{t}}^1,\boldsymbol{t}^1)+\mathcal{B}_{UT}^1(\tilde{\boldsymbol{t}}^1,\boldsymbol{u}^1)+\mathcal{B}_{UC}^1(\tilde{\boldsymbol{t}}^1,\Delta\boldsymbol{u}^1)+ & 0 & + & 0 & + & 0 & +\mathcal{A}_{UI}^1(\tilde{\boldsymbol{t}}^1,\boldsymbol{t}_I)+\mathcal{B}_{UI}^1(\tilde{\boldsymbol{t}}^1,\boldsymbol{u}_I)=\mathcal{R}_U^1(\tilde{\boldsymbol{t}}^1) \\
\mathcal{B}_{UT}^1(\boldsymbol{t}^1,\tilde{\boldsymbol{v}}^1)+\mathcal{C}_{TT}^1(\tilde{\boldsymbol{v}}^1,\boldsymbol{u}^1)+\mathcal{C}_{TC}^1(\tilde{\boldsymbol{v}}^1,\Delta\boldsymbol{u}^1)+ & 0 & + & 0 & + & 0 & +\mathcal{B}_{TI}^1(\boldsymbol{t}_I,\tilde{\boldsymbol{v}}^1)+\mathcal{C}_{TI}^1(\tilde{\boldsymbol{v}}^1,\boldsymbol{u}_I)=\mathcal{R}_T^1(\tilde{\boldsymbol{v}}^1) \\
\mathcal{B}_{UC}^1(\boldsymbol{t}^1,\tilde{\boldsymbol{v}}^1)+\mathcal{C}_{TC}^1(\tilde{\boldsymbol{v}}^1,\boldsymbol{u}^1)+\mathcal{C}_{CC}^1(\tilde{\boldsymbol{v}}^1,\Delta\boldsymbol{u}^1)+ & 0 & + & 0 & + & 0 & +\mathcal{B}_{IC}^1(\boldsymbol{t}_I,\tilde{\boldsymbol{v}}^1)+\mathcal{C}_{CI}^1(\tilde{\boldsymbol{v}}^1,\boldsymbol{u}_I)=\mathcal{R}_C^1(\tilde{\boldsymbol{v}}^1) \\
0 & + & 0 & + & 0 & +\mathcal{A}_{UU}^2(\tilde{\boldsymbol{t}}^2,\boldsymbol{t}^2)+\mathcal{B}_{UT}^2(\tilde{\boldsymbol{t}}^2,\boldsymbol{u}^2)+\mathcal{B}_{UC}^2(\tilde{\boldsymbol{t}}^2,\Delta\boldsymbol{u}^2)-\mathcal{A}_{UI}^2(\tilde{\boldsymbol{t}}^2,\boldsymbol{t}_I)+\mathcal{B}_{UI}^2(\tilde{\boldsymbol{t}}^2,\boldsymbol{u}_I)=\mathcal{R}_U^2(\tilde{\boldsymbol{t}}^2) \\
0 & + & 0 & + & 0 & +\mathcal{B}_{UT}^2(\boldsymbol{t}^2,\tilde{\boldsymbol{v}}^2)+\mathcal{C}_{TT}^2(\tilde{\boldsymbol{v}}^2,\boldsymbol{u}^2)+\mathcal{C}_{TC}^2(\tilde{\boldsymbol{v}}^2,\Delta\boldsymbol{u}^2)-\mathcal{B}_{IT}^2(\boldsymbol{t}_I,\tilde{\boldsymbol{v}}^2)+\mathcal{C}_{TI}^2(\tilde{\boldsymbol{v}}^2,\boldsymbol{u}_I)=\mathcal{R}_T^2(\tilde{\boldsymbol{v}}^2) \\
0 & + & 0 & + & 0 & +\mathcal{B}_{UC}^2(\boldsymbol{t}^2,\tilde{\boldsymbol{v}}^2)+\mathcal{C}_{TC}^2(\tilde{\boldsymbol{v}}^2,\boldsymbol{u}^2)+\mathcal{C}_{CC}^2(\tilde{\boldsymbol{v}}^2,\Delta\boldsymbol{u}^2)-\mathcal{B}_{IC}^2(\boldsymbol{t}_I,\tilde{\boldsymbol{v}}^2)+\mathcal{C}_{CI}^2(\tilde{\boldsymbol{v}}^2,\boldsymbol{u}_I)=\mathcal{R}_C^2(\tilde{\boldsymbol{v}}^2) \\
\mathcal{A}_{IU}^1(\tilde{\boldsymbol{t}}_I,\boldsymbol{t}^1)+\mathcal{B}_{IT}^{\gamma}(\tilde{\boldsymbol{t}}_I,\boldsymbol{u}^1)+\mathcal{B}_{IC}^1(\tilde{\boldsymbol{t}}_I,\Delta\boldsymbol{u}^1)-\mathcal{A}_{IU}^2(\tilde{\boldsymbol{t}}_I,\boldsymbol{t}^2)-\mathcal{B}_{IT}^{\gamma}(\tilde{\boldsymbol{t}}_I,\boldsymbol{u}^2)-\mathcal{B}_{IC}^2(\tilde{\boldsymbol{t}}_I,\Delta\boldsymbol{u}^2)+\mathcal{A}_{II}^*(\tilde{\boldsymbol{t}}_I,\boldsymbol{t}_I)+\mathcal{B}_{II}^*(\tilde{\boldsymbol{t}}_I,\boldsymbol{u}_I)=\mathcal{R}_U^I(\tilde{\boldsymbol{t}}_I) \\
\mathcal{B}_{UI}^1(\boldsymbol{t}^1,\boldsymbol{u}_I)+\mathcal{C}_{TI}^1(\tilde{\boldsymbol{u}}_I,\boldsymbol{u}^1)+\mathcal{C}_{CI}^1(\tilde{\boldsymbol{u}}_I,\Delta\boldsymbol{u}^1)+\mathcal{B}_{UI}^2(\boldsymbol{t}^2,\boldsymbol{u}_I)+\mathcal{C}_{TI}^2(\tilde{\boldsymbol{u}}_I,\boldsymbol{u}^2)+\mathcal{C}_{CI}^2(\tilde{\boldsymbol{u}}_I,\Delta\boldsymbol{u}^2)+\mathcal{B}_{II}^*(\boldsymbol{t}_I,\tilde{\boldsymbol{u}}_I)+\mathcal{C}_{II}^*(\tilde{\boldsymbol{u}}_I,\boldsymbol{u}_I)=\mathcal{R}_T^I(\tilde{\boldsymbol{u}}_I)
\end{array} \tag{2.33}$$

where additional bilinear and linear operators appearing in (2.33) are defined by

$$\mathcal{A}_{II}^*(\tilde{\boldsymbol{t}}_I,\boldsymbol{t}_I) = \mathcal{A}_{II}^1(\tilde{\boldsymbol{t}}_I,\boldsymbol{t}_I) + \mathcal{A}_{II}^2(\tilde{\boldsymbol{t}}_I,\boldsymbol{t}_I) \tag{2.34}$$

$$\mathcal{B}_{II}^*(\tilde{\boldsymbol{t}}_I,\boldsymbol{u}_I) = \mathcal{B}_{II}^1(\tilde{\boldsymbol{t}}_I,\boldsymbol{u}_I) - \mathcal{B}_{II}^2(\tilde{\boldsymbol{t}}_I,\boldsymbol{u}_I) \tag{2.35}$$

$$\mathcal{C}_{II}^*(\tilde{\boldsymbol{u}}_I,\boldsymbol{u}_I) = \mathcal{C}_{II}^1(\tilde{\boldsymbol{u}}_I,\boldsymbol{u}_I) + \mathcal{C}_{II}^2(\tilde{\boldsymbol{u}}_I,\boldsymbol{u}_I) \tag{2.36}$$

$$\mathcal{R}_U^I(\tilde{\boldsymbol{t}}_I) = \mathcal{R}_U^{I1}(\tilde{\boldsymbol{t}}_I) - \mathcal{R}_U^{I2}(\tilde{\boldsymbol{t}}_I) \tag{2.37}$$

$$\mathcal{R}_T^I(\tilde{\boldsymbol{u}}_I) = \mathcal{R}_T^{I1}(\tilde{\boldsymbol{u}}_I) + \mathcal{R}_T^{I2}(\tilde{\boldsymbol{u}}_I) \tag{2.38}$$

It should be evident from (2.33) that the boundary integral equations are in a symmetric form. It is worth noting that while the formulation presented above is developed specifically for a bi-material domain, the extension to multi-material

domain can be readily established and results for that general case is not included here for brevity.

2.5 INTEGRAL EQUATION FOR SUM OF CRACK-FACE DISPLACEMENTS

The weak-form boundary integral equation for the sum of crack-face displacement in each sub-region can be readily established from the weak-form displacement integral equation (2.17) via the proper choice of test functions. Specifically, by choosing $\tilde{t}_p = 0$ on $S_T^\gamma \cup S_U^\gamma \cup S_I^\gamma$ in the weak-form equation (2.17), it gives rise to

$$\begin{aligned}\mathscr{D}_C^\gamma(\tilde{\boldsymbol{t}}^\gamma, \Sigma \boldsymbol{u}^\gamma) = {} & \mathscr{A}_{CU}^\gamma(\tilde{\boldsymbol{t}}^\gamma, \boldsymbol{t}^\gamma) + \mathscr{A}_{CT}^\gamma(\tilde{\boldsymbol{t}}^\gamma, \boldsymbol{t}^\gamma) + \mathscr{A}_{CC}^\gamma(\tilde{\boldsymbol{t}}^\gamma, \Sigma \boldsymbol{t}^\gamma) + \mathscr{A}_{CI}^\gamma(\tilde{\boldsymbol{t}}^\gamma, \boldsymbol{t}_I^\gamma) \\ & + \mathscr{B}_{CU}^\gamma(\tilde{\boldsymbol{t}}^\gamma, \boldsymbol{u}^\gamma) + \mathscr{B}_{CT}^\gamma(\tilde{\boldsymbol{t}}^\gamma, \boldsymbol{u}^\gamma) + \mathscr{B}_{CC}^\gamma(\tilde{\boldsymbol{t}}^\gamma, \Delta \boldsymbol{u}^\gamma) + \mathscr{B}_{CI}^\gamma(\tilde{\boldsymbol{t}}^\gamma, \boldsymbol{u}_I^\gamma)\end{aligned} \tag{2.39}$$

It should be remarked that integrals appearing on the right hand side of (2.39) involve the prescribed displacement and traction on the boundary, the known sum of the crack-face traction, the unknown relative crack-face displacement, and unknown displacement and traction along the material interface. Clearly, once the system of boundary integral equations (2.33) is solved, all unknowns on the right hand sided of (2.39) are determined and (2.39) can be then used to post-process for the sum of the crack-face displacement in each sub-region.

2.6 NEAR-FRONT STRESS FIELD

In linear elastic fracture analysis, two essential fracture parameters, commonly termed the stress intensity factors and the T-stresses, are of primary interest in addition to the elastic field induced within the domain. The former is known to sufficiently describing the singular part of the near-front stress field whereas the latter represents the non-zero nonsingular part of stress along the crack front. By following the primitive work of admits the Williams, 1957, the near-front stress field in a region surrounding a point x_c representation (see also the work of Rungamornrat and Pinitpanich, 2016)

$$\bar{\sigma}_{ij}(\boldsymbol{x}_c; \bar{r}, \bar{\theta}) = \frac{1}{\sqrt{2\pi \bar{r}}} \sum_{n=1}^{3} K_n(\boldsymbol{x}_c) \bar{\sigma}_{ij}^{K(n)}(\bar{\theta}) + T_{ij}(\boldsymbol{x}_c) + \sum_{m=1}^{\infty} \bar{r}^{m/2} \bar{\sigma}_{ij}^{(m)}(\boldsymbol{x}_c; \bar{\theta}) \tag{2.40}$$

where all quantities appearing in (2.40) are referred to the local Cartesian coordinate system $\{\boldsymbol{x}_c; \bar{x}_1, \bar{x}_2, \bar{x}_3\}$ with origin at point x_c and a set of orthonormal basis vectors $\{\bar{\boldsymbol{e}}_1, \bar{\boldsymbol{e}}_2, \bar{\boldsymbol{e}}_3\}$ shown in Figure 2.4 (in particular, $\bar{\boldsymbol{e}}_1$ is normal to the crack front and contained in the tangent plane of the crack surface at x_c, $\bar{\boldsymbol{e}}_2 = -\boldsymbol{n}^+(\boldsymbol{x}_c)$, and $\bar{\boldsymbol{e}}_3 = \bar{\boldsymbol{e}}_1 \times \bar{\boldsymbol{e}}_2$); $(\bar{r}, \bar{\theta})$ are polar coordinates associated with the local two-dimensional Cartesian coordinate system $\{\boldsymbol{x}_c; \bar{x}_1, \bar{x}_2\}$; $K_1(\boldsymbol{x}_c)$, $K_2(\boldsymbol{x}_c)$, $K_3(\boldsymbol{x}_c)$ are mode-I, mode-II, and mode-III stress intensity factors at point x_c; $T_{ij}(\boldsymbol{x}_c)$ are components of the T-stress tensor; and $\bar{\sigma}_{ij}^{K(n)}$ and $\bar{\sigma}_{ij}^{(m)}$ are angular-dependent functions that can be completely obtained from the near-front eigen-analysis. It is apparent from the expansion (2.40) that the first term is singular at x_c of $\mathcal{O}(r^{-1/2})$, the second term is independent of the coordinates $\bar{r}$ and $\bar{\theta}$, and all remaining terms identically vanish along the crack front.

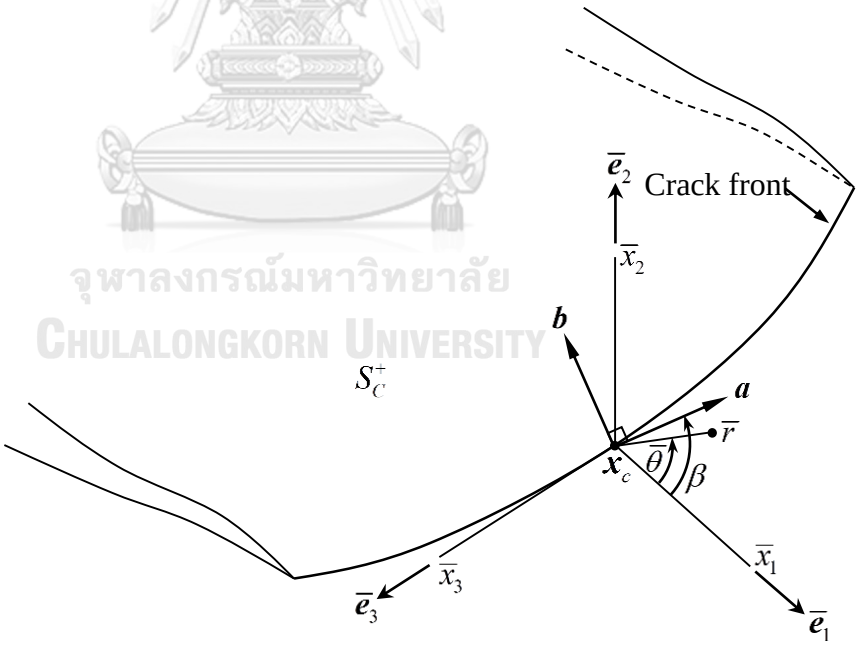

Figure 2.4: Local coordinate system utilized in determination of stress intensity factors and T-stress components

Based on the representation (2.40) and the known information of the angular dependent functions $\bar{\sigma}_{ij}^{K(n)}$, the stress intensity factors $K_1(\boldsymbol{x}_c)$, $K_2(\boldsymbol{x}_c)$ and $K_3(\boldsymbol{x}_c)$ can be related to the stress field in the neighborhood of x_c by

$$K_1(\boldsymbol{x}_c) = \lim_{\bar{r}\to 0} \sqrt{2\pi\bar{r}}\,\bar{\sigma}_{22}(\boldsymbol{x}_c;\bar{r},\bar{\theta}=0) \tag{2.41}$$

$$K_2(\boldsymbol{x}_c) = \lim_{\bar{r}\to 0} \sqrt{2\pi\bar{r}}\,\bar{\sigma}_{12}(\boldsymbol{x}_c;\bar{r},\bar{\theta}=0) \tag{2.42}$$

$$K_3(\boldsymbol{x}_c) = \lim_{\bar{r}\to 0} \sqrt{2\pi\bar{r}}\,\bar{\sigma}_{23}(\boldsymbol{x}_c;\bar{r},\bar{\theta}=0) \tag{2.43}$$

While the relations (2.41)-(2.43) can be used to post-process for the stress intensity factors, the requirement of the complete stress field within the cracked body renders them not suitable to be employed in the present study. This is due mainly to that the primary unknowns chosen in the formulation of boundary value problems correspond directly to quantities on the boundary, the crack surface and the material interface, and that the post-process for stress at any interior point using the stress integral relation along with the limiting process is non-trivial and can be computationally inefficient. To circumvent this issue, an alternative formula for the stress intensity factors, proposed by Barnett and Asaro, 1972 and Xu, 2000, is employed. Such expression allows $K_1(\boldsymbol{x}_c)$, $K_2(\boldsymbol{x}_c)$ and $K_3(\boldsymbol{x}_c)$ to be calculated directly in terms of the relative crack-face displacements in the vicinity of the crack front as follows

$$k_i(\boldsymbol{x}_c) = \frac{\sqrt{2\pi}}{4} B_{ij} \lim_{\bar{x}_1\to 0^-,\,\bar{\boldsymbol{x}}\to \boldsymbol{x}_c} \left(\frac{\Delta\bar{u}_j(\bar{\boldsymbol{x}})}{\sqrt{-\bar{x}_1}} \right) \tag{2.44}$$

where $k_1(\boldsymbol{x}_c) = K_2(\boldsymbol{x}_c)$, $k_2(\boldsymbol{x}_c) = K_1(\boldsymbol{x}_c)$, $k_3(\boldsymbol{x}_c) = K_3(\boldsymbol{x}_c)$, $\Delta\bar{u}_j$ are components of the relative crack-face displacements referring to the local coordinate system $\{\boldsymbol{x}_c;\bar{x}_1,\bar{x}_2,\bar{x}_3\}$; and B_{ij} are material-dependent constants defined by

$$B_{ij} = \frac{1}{2\pi}\int_0^{2\pi} [(\boldsymbol{a},\boldsymbol{a})_{ij} - (\boldsymbol{a},\boldsymbol{b})_{im}(\boldsymbol{b},\boldsymbol{b})^{-1}_{mn}(\boldsymbol{b},\boldsymbol{a})_{nj}]d\beta \tag{2.45}$$

in which $\boldsymbol{a}$ and $\boldsymbol{b}$ are orthonormal vectors contained in the plane $\bar{x}_3 = 0$; β is the angle between $\boldsymbol{a}$ and $\bar{\boldsymbol{e}}_1$ as indicated in Figure 2.4; and $(\boldsymbol{a},\boldsymbol{b})_{ij} = a_m E_{mijn} b_n$.

From the continuity of the finite part of stress at any point $\boldsymbol{x}_c$ along the crack front, it can be readily verified that the three components T_{22}, T_{12} and T_{23} of the T-stress tensor can be obtained in terms of the prescribed crack-face traction at the limiting point $\boldsymbol{x}_c$ on the crack surface, i.e.,

$$T_{22}(\boldsymbol{x}_c) = -\lim_{\boldsymbol{x}\to\boldsymbol{x}_c} \bar{t}_2^{+}(\boldsymbol{x}) \tag{2.46}$$

$$T_{12}(\boldsymbol{x}_c) = -\lim_{\boldsymbol{x}\to\boldsymbol{x}_c} \bar{t}_1^{+}(\boldsymbol{x}) \tag{2.47}$$

$$T_{23}(\boldsymbol{x}_c) = -\lim_{\boldsymbol{x}\to\boldsymbol{x}_c} \bar{t}_3^{+}(\boldsymbol{x}) \tag{2.48}$$

where $\bar{t}_i^{+}$ are components of the prescribed crack-face traction referring to the local coordinate system $\{\boldsymbol{x}_c; \bar{x}_1, \bar{x}_2, \bar{x}_3\}$. From the symmetry of the T-stress tensor, the remaining three components T_{11}, T_{33} and T_{13} must be determined to obtain the complete description of the second term in the expansion (2.40) and such three components are referred to the T-stress components. From the structure of the near-front stress field (2.40) along with standard differentiation and limiting process, the T-stress components can be obtained from

$$T_{11}(\boldsymbol{x}_c) = 2\lim_{\bar{r}\to 0}\left\{\sqrt{\bar{r}}\,\frac{\partial}{\partial \bar{r}}\left[\sqrt{\bar{r}}\,\bar{\sigma}_{11}(\boldsymbol{x}_c;\bar{r},\bar{\theta}=0)\right]\right\} \tag{2.49}$$

$$T_{33}(\boldsymbol{x}_c) = 2\lim_{\bar{r}\to 0}\left\{\sqrt{\bar{r}}\,\frac{\partial}{\partial \bar{r}}\left[\sqrt{\bar{r}}\,\bar{\sigma}_{33}(\boldsymbol{x}_c;\bar{r},\bar{\theta}=0)\right]\right\} \tag{2.50}$$

$$T_{13}(\boldsymbol{x}_c) = 2\lim_{\bar{r}\to 0}\left\{\sqrt{\bar{r}}\,\frac{\partial}{\partial \bar{r}}\left[\sqrt{\bar{r}}\,\bar{\sigma}_{13}(\boldsymbol{x}_c;\bar{r},\bar{\theta}=0)\right]\right\} \tag{2.51}$$

If the expressions (2.49)-(2.51) are utilized to post-process for the T-stress components, the computational cost associated with the calculation of stresses at interior points and the numerical differentiations and limits must be paid. To avoid such difficulty, an alternative scheme based upon the boundedness of the T-stress

tensor is introduced. It can be seen from the representation (2.40) that $T_{ij}(\boldsymbol{x}_c)$ represents, in fact, the local components of a finite part of the stress at a point $\boldsymbol{x}_c$ along the crack front. As a direct consequence, $T_{ij}(\boldsymbol{x}_c)$ can be related to a finite part of the strain at a point $\boldsymbol{x}_c$ via the following constitutive relation

$$T_{ij}(\boldsymbol{x}_c) = \bar{E}_{ijkl}\bar{\varepsilon}^*_{kl}(\boldsymbol{x}_c) \tag{2.52}$$

where $\bar{E}_{ijkl}$ are elastic moduli referring to the local coordinate system and $\bar{\varepsilon}^*_{kl}(\boldsymbol{x}_c)$ denote local components of the finite part of the strain at $\boldsymbol{x}_c$. From the closure condition at the point $\boldsymbol{x}_c$ (i.e., $\Delta u_i(\boldsymbol{x}_c) = 0$), the local in-plane components $\bar{\varepsilon}^*_{11}(\boldsymbol{x}_c)$, $\bar{\varepsilon}^*_{13}(\boldsymbol{x}_c)$, and $\bar{\varepsilon}^*_{33}(\boldsymbol{x}_c)$ can be related to the sum of the crack-face displacements in the neighborhood of the point $\boldsymbol{x}_c$ by

$$\bar{\varepsilon}^*_{11}(\boldsymbol{x}_c) = \frac{1}{2}\lim_{\bar{\boldsymbol{x}}\to\boldsymbol{x}_c}\frac{\partial\Sigma\bar{u}_1(\bar{\boldsymbol{x}})}{\partial\bar{x}_1} = \frac{1}{2}\frac{\partial\Sigma\bar{u}_1}{\partial\bar{x}_1}(\boldsymbol{x}_c) \tag{2.53}$$

$$\bar{\varepsilon}^*_{13}(\boldsymbol{x}_c) = \frac{1}{4}\lim_{\bar{\boldsymbol{x}}\to\boldsymbol{x}_c}\left(\frac{\partial\Sigma\bar{u}_1(\bar{\boldsymbol{x}})}{\partial\bar{x}_3} + \frac{\partial\Sigma\bar{u}_3(\bar{\boldsymbol{x}})}{\partial\bar{x}_1}\right) = \frac{1}{4}\left(\frac{\partial\Sigma\bar{u}_1}{\partial\bar{x}_3}(\boldsymbol{x}_c) + \frac{\partial\Sigma\bar{u}_3}{\partial\bar{x}_1}(\boldsymbol{x}_c)\right) \tag{2.54}$$

$$\bar{\varepsilon}^*_{33}(\boldsymbol{x}_c) = \frac{1}{2}\lim_{\bar{\boldsymbol{x}}\to\boldsymbol{x}_c}\frac{\partial\Sigma\bar{u}_3(\bar{\boldsymbol{x}})}{\partial\bar{x}_3} = \frac{1}{2}\frac{\partial\Sigma\bar{u}_3}{\partial\bar{x}_3}(\boldsymbol{x}_c) \tag{2.55}$$

From the prescribed conditions (2.46)-(2.48) along with the relations (2.53)-(2.55), a system of linear algebraic equations (2.52) is sufficient for determining the T-stress components $T_{11}(\boldsymbol{x}_c)$, $T_{33}(\boldsymbol{x}_c)$ and $T_{13}(\boldsymbol{x}_c)$ in terms of the sum of the crack-face displacements. This methodology for determining the T-stress along the crack front can also be found in the work of Pham et al. (2015a).

CHAPTER 3
SOLUTION PROCEDURE

This chapter presents the numerical procedure for constructing approximate solutions of the system of boundary integral equations (2.33) and the weak-form integral equation for the sum of the crack-face displacement (2.39). The discretization of both geometry and solution and other essential components such as the quadrature and evaluation of kernels are briefly discussed. Finally, the post process for the stress intensity factors and the T-stress components are addressed.

3.1 DETERMINATION OF JUMP IN CRACK-FACE DISPLACEMENTS

A system of boundary integral equations (2.33) involves three sets of unknown functions including the displacement and traction on the ordinary boundary, the displacement and traction on the material interface, and the jump in the crack-face displacement, and two sets of prescribed data including the known displacement and traction on the ordinary boundary and the sum of and jump in the crack-face tractions.

A well-known, weakly singular, symmetric Galerkin boundary element method (SGBEM) is utilized to construct approximate solutions of (2.33). Standard Galerkin approximation together with the finite element procedure is utilized in the discretization of the unknown data, test functions, and geometries of the ordinary boundary S_0, the material interface S_I and the crack surfaces S_C^{1+} and S_C^{2+}. In particular, all unknown data and test functions for each sub-region Ω^γ and on the material interface are approximated by

$$\boldsymbol{u}^\gamma = (\boldsymbol{\Phi}_t^\gamma)^T \boldsymbol{U}^\gamma, \tilde{\boldsymbol{v}}^\gamma = (\boldsymbol{\Phi}_t^\gamma)^T \boldsymbol{V}^{t\gamma} \quad \text{on } S_t^\gamma \tag{3.1}$$

$$\boldsymbol{t}^\gamma = (\boldsymbol{\Phi}_u^\gamma)^T \boldsymbol{T}^\gamma, \tilde{\boldsymbol{t}}^\gamma = (\boldsymbol{\Phi}_u^\gamma)^T \tilde{\boldsymbol{T}}^\gamma \quad \text{on } S_u^\gamma \tag{3.2}$$

$$\Delta\boldsymbol{u}^\gamma = (\boldsymbol{\Phi}_c^\gamma)^T \Delta\boldsymbol{U}^\gamma, \tilde{\boldsymbol{v}}^\gamma = (\boldsymbol{\Phi}_c^\gamma)^T \boldsymbol{V}^{c\gamma} \quad \text{on } S_C^{\gamma+} \tag{3.3}$$

$$\boldsymbol{u}_I = (\boldsymbol{\Phi}_I)^T \boldsymbol{U}_I, \tilde{\boldsymbol{u}}_I = (\boldsymbol{\Phi}_I)^T \tilde{\boldsymbol{U}}_I \quad \text{on } S_I \tag{3.4}$$

$$\boldsymbol{t}_I = (\boldsymbol{\Phi}_I)^T \boldsymbol{T}_I, \tilde{\boldsymbol{t}}_I = (\boldsymbol{\Phi}_I)^T \tilde{\boldsymbol{T}}_I \quad \text{on } S_I \tag{3.5}$$

where $\boldsymbol{\Phi}_t^\gamma$, $\boldsymbol{\Phi}_u^\gamma$, $\boldsymbol{\Phi}_c^\gamma$, and $\boldsymbol{\Phi}_I$ are vectors of nodal basis functions defined on the surfaces S_T^γ, S_U^γ, S_C^γ, and S_I, respectively; $\boldsymbol{U}^\gamma$, $\boldsymbol{T}^\gamma$, $\Delta\boldsymbol{U}^\gamma$, $\boldsymbol{U}_I$, and $\boldsymbol{T}_I$ are vectors of unknown nodal quantities associated with the displacement on S_T^γ, the traction on S_U^γ, the relative crack-face displacement on $S_C^{\gamma+}$, the displacement on S_I, and the traction on S_I, respectively; $\boldsymbol{V}^{t\gamma}$, $\tilde{\boldsymbol{T}}^\gamma$, $\boldsymbol{V}^{c\gamma}$, $\tilde{\boldsymbol{U}}_I$ and $\tilde{\boldsymbol{T}}_I$ are vectors of arbitrary nodal quantities; and $(\cdot)^T$ denotes the transpose operator. Due to the weakly singular nature of all involved integrals, all nodal basis functions are constructed locally on each C^0-element in a finite element mesh using standard finite element procedure. In addition, to enhance the near-front approximation, special local C^0-interpolation functions defined over special crack-tip elements (see details in the work of Xiao, 1998 and Rungamornrat and Mear (2008b)) are employed to discretize the relative crack-face displacement in all elements adjacent to the crack front.

Substituting the approximations (3.1)-(3.5) into the system of governing equations (2.33) and then exploiting the arbitrariness of $\boldsymbol{V}^{t\gamma}$, $\tilde{\boldsymbol{T}}^\gamma$, $\boldsymbol{V}^{c\gamma}$, $\tilde{\boldsymbol{U}}_I$ and $\tilde{\boldsymbol{T}}_I$ lead to the following system of linear algebraic equations

$$\begin{bmatrix}
\mathbf{A}_{UU}^1 & \mathbf{B}_{UT}^1 & \mathbf{B}_{UC}^1 & \mathbf{0} & \mathbf{0} & \mathbf{0} & \mathbf{A}_{UI}^1 & \mathbf{B}_{UI}^1 \\
(\mathbf{B}_{UT}^1)^T & \mathbf{C}_{TT}^1 & \mathbf{C}_{TC}^1 & \mathbf{0} & \mathbf{0} & \mathbf{0} & (\mathbf{B}_{IT}^1)^T & \mathbf{C}_{TI}^1 \\
(\mathbf{B}_{UC}^1)^T & (\mathbf{C}_{TC}^1)^T & \mathbf{C}_{CC}^1 & \mathbf{0} & \mathbf{0} & \mathbf{0} & (\mathbf{B}_{IC}^1)^T & \mathbf{C}_{CI}^1 \\
\mathbf{0} & \mathbf{0} & \mathbf{0} & \mathbf{A}_{UU}^2 & \mathbf{B}_{UT}^2 & \mathbf{B}_{UC}^2 & \mathbf{A}_{UI}^2 & \mathbf{B}_{UI}^2 \\
\mathbf{0} & \mathbf{0} & \mathbf{0} & (\mathbf{B}_{UT}^2)^T & \mathbf{C}_{TT}^2 & \mathbf{C}_{TC}^2 & (\mathbf{B}_{IT}^2)^T & \mathbf{C}_{TI}^2 \\
\mathbf{0} & \mathbf{0} & \mathbf{0} & (\mathbf{B}_{UC}^2)^T & (\mathbf{C}_{TC}^2)^T & \mathbf{C}_{CC}^2 & (\mathbf{B}_{IC}^2)^T & \mathbf{C}_{CI}^2 \\
(\mathbf{A}_{UI}^1)^T & \mathbf{B}_{IT}^1 & \mathbf{B}_{IC}^1 & (\mathbf{A}_{UI}^2)^T & \mathbf{B}_{IT}^2 & \mathbf{B}_{IC}^2 & \mathbf{A}_{II}^* & \mathbf{B}_{II}^* \\
(\mathbf{B}_{UI}^1)^T & (\mathbf{C}_{TI}^1)^T & (\mathbf{C}_{CI}^1)^T & (\mathbf{B}_{UI}^2)^T & (\mathbf{C}_{TI}^2)^T & (\mathbf{C}_{CI}^2)^T & (\mathbf{B}_{II}^*)^T & \mathbf{C}_{II}^*
\end{bmatrix}
\begin{bmatrix} \boldsymbol{T}^1 \\ \mathbf{U}^1 \\ \Delta\mathbf{U}^1 \\ \mathbf{T}^2 \\ \mathbf{U}^2 \\ \Delta\mathbf{U}^2 \\ \mathbf{T}_I \\ \mathbf{U}_I \end{bmatrix}
=
\begin{bmatrix} \mathbf{R}_U^1 \\ \mathbf{R}_T^1 \\ \mathbf{R}_C^1 \\ \mathbf{R}_U^2 \\ \mathbf{R}_T^2 \\ \mathbf{R}_C^2 \\ \mathbf{R}_U^I \\ \mathbf{R}_T^I \end{bmatrix} \tag{3.6}$$

where the sub-matrices $\mathbf{A}_{pq}^\gamma$, $\mathbf{B}_{pq}^\gamma$, $\mathbf{C}_{pq}^\gamma$, $\mathbf{A}_{II}^*$, $\mathbf{B}_{II}^*$ and $\mathbf{C}_{II}^*$ for $p,q \in \{T,U,C,I\}$ are obtained from the discretization of the bilinear integral operators $\mathcal{A}_{pq}^\gamma$, $\mathcal{B}_{pq}^\gamma$, $\mathcal{C}_{pq}^\gamma$, $\mathcal{A}_{II}^*$, $\mathcal{B}_{II}^*$ and $\mathcal{C}_{II}^*$, respectively and the sub-vectors $\mathbf{R}_p^\gamma$ and $\mathbf{R}_p^I$ for $p \in \{T,U,C,I\}$ are obtained from the discretization of the linear integral operators $\mathcal{R}_p^\gamma$ and $\mathcal{R}_p^I$, respectively. To construct the involved coefficient matrix and know vector, two computational issues, one associated with the numerical integration of weakly

singular and nearly singular double surface integrals and the other corresponding to the numerical evaluation of kernels for general anisotropy, must be properly treated. In the present study, the former is achieved by adopting the special quadrature combining a series of variable transformations and Gaussian quadrature proposed by Xiao, 1998 whereas the latter is handled by utilizing the interpolation technique based on a finite element interpolant proposed by Rungamornrat and Mear (2008b) to mainly avoid the direct integration of the closed contour integral. The system of linear equations (3.6) is essentially symmetric resulting from the symmetry of the formulation and is solved numerically using selected indirect linear solvers such as a conjugate gradient method. The relative crack-face displacement for cracks in each sub-region is then obtained once $\Delta \boldsymbol{U}^{\gamma}$ is determined.

3.2 DETERMINATION OF SUM OF CRACK-FACE DISPLACEMENTS

After the solution of the system of boundary integral equations (2.33) is obtained, the weak-form integral equation (2.39) contains only one unknown associated with the sum of the crack-face displacement and is then solved by using standard finite element procedure.

First, the additional approximation of the sum of the crack-face displacements $\Sigma \boldsymbol{u}^{\gamma}$ and the test function $\tilde{\boldsymbol{t}}^{\gamma}$ on the crack surface $S_C^{\gamma+}$ is introduced

$$\Sigma \boldsymbol{u}^{\gamma} = (\boldsymbol{\Phi}_{\Sigma}^{\gamma})^T \Sigma \boldsymbol{U}^{\gamma}, \quad \tilde{\boldsymbol{t}}^{\gamma} = (\boldsymbol{\Phi}_{\Sigma}^{\gamma})^T \tilde{\boldsymbol{T}}^{\Sigma\gamma} \tag{3.7}$$

where $\boldsymbol{\Phi}_{\Sigma}^{\gamma}$ denotes a vector of nodal basis functions constructed locally on standard two-dimensional elements by the finite element procedure; $\Sigma \boldsymbol{U}^{\gamma}$ is a vector of unknown nodal quantities associated with the sum of the crack-face displacements; and $\tilde{\boldsymbol{T}}^{\Sigma\gamma}$ is a vector of arbitrary nodal quantities. By applying (3.7) along with results from solving the system (2.39), the weak-from equation (2.39) for each sub-region can be discretized into

$$\boldsymbol{D}_C^{\gamma} \Sigma \boldsymbol{U}^{\gamma} = \boldsymbol{R}_{\Sigma}^{\gamma} + \boldsymbol{A}_{CU}^{\gamma} \boldsymbol{T}^{\gamma} + \boldsymbol{A}_{CI}^{\gamma} \boldsymbol{T}_I + \boldsymbol{B}_{CT}^{\gamma} \boldsymbol{U}^{\gamma} + \boldsymbol{B}_{CC}^{\gamma} \Delta \boldsymbol{U}^{\gamma} + \boldsymbol{B}_{CI}^{\gamma} \boldsymbol{U}_I \tag{3.8}$$

where the matrices $\boldsymbol{D}_C^{\gamma}$, $\boldsymbol{A}_{CU}^{\gamma}$, $\boldsymbol{A}_{CI}^{\gamma}$, $\boldsymbol{B}_{CT}^{\gamma}$, $\boldsymbol{B}_{CC}^{\gamma}$ and $\boldsymbol{B}_{CI}^{\gamma}$ result directly from the discretization of the bilinear integral operators $\mathscr{D}_C^{\gamma}$, $\mathscr{A}_{CU}^{\gamma}$, $\mathscr{A}_{CI}^{\gamma}$, $\mathscr{B}_{CT}^{\gamma}$, $\mathscr{B}_{CC}^{\gamma}$ and $\mathscr{B}_{CI}^{\gamma}$

, respectively, and the vector $\boldsymbol{R}_{\Sigma}^{\gamma}$ is obtained from the discretization of the combined linear operator $\mathcal{A}_{CT}^{\gamma}+\mathcal{A}_{CC}^{\gamma}+\mathcal{B}_{CU}^{\gamma}$. Again, the same procedure of numerical integration and evaluation of kernels is applied to construct all involved matrices and vectors. From the symmetry of the bilinear integral operator $\mathcal{D}_{C}^{\gamma}$, the coefficient matrix $\boldsymbol{D}_{C}^{\gamma}$ is clearly symmetric and the system of linear algebraic equations (3.8) can be solved for $\Sigma\boldsymbol{U}^{\gamma}$ for each sub-region.

3.3 POST PROCESS FOR STRESS INTENSITY FACTORS AND T-STRESSES

To post process for the stress intensity factors and T-stress components along the crack front, the relative crack-face displacement and the sum of the crack-face displacements obtained in Section 3.1 and Section 3.2 are employed, respectively.

By employing the formula (2.44) along with the near-front approximation of the relative crack-face displacement on special 9-node crack-tip elements (see Li and Mear, 1998 and Rungamornrat and Mear (2008b)) and Taylor series expansion, the explicit expression for the stress intensity factors takes the form

$$k_i(\boldsymbol{x}_c)=\sqrt{\frac{\pi}{2\gamma}}B_{ij}\left[\hat{\boldsymbol{u}}(\boldsymbol{x}_c)\cdot\bar{\boldsymbol{e}}_j\right] \tag{3.9}$$

where all involved parameters are defined by

$$\gamma=-\bar{\boldsymbol{e}}_1\cdot\frac{\partial\boldsymbol{r}_c}{\partial\eta}(\xi_c,-1) \tag{3.10}$$

$$\boldsymbol{r}_c=\sum_{i=1}^{9}\boldsymbol{x}^{(i)}\psi^{(i)}(\xi,\eta)-\boldsymbol{x}_c \tag{3.11}$$

$$\hat{\boldsymbol{u}}(\boldsymbol{x}_c)=\sum\Delta\boldsymbol{u}^{(i)}\psi^{(i)}(\xi_c,-1) \tag{3.12}$$

in which $(\xi,\eta)\in[-1,1]\times[-1,1]$ are natural coordinates used to define the master element; $\boldsymbol{x}^{(i)}$ denotes the i^{th} nodal point of the crack-tip element; $\psi^{(i)}(\xi,\eta)$ are shape functions associated with the i^{th} node of a standard 9-node quadratic element; $\Delta\boldsymbol{u}^{(i)}$ denotes the extra degree of freedom associated with the i^{th} node of the crack-tip element located along the crack front; and the summation appearing in (3.12) is taken only for nodes along the crack front. It is apparent from (3.9) that once $\Delta\boldsymbol{U}^{\gamma}$

for each sub-region is obtained, the information $\Delta \boldsymbol{u}^{(i)}$ can be readily obtained and used to directly post-process the stress intensity factor without carrying out the limiting process.

For the T-stress components, once the unknown $\Sigma \boldsymbol{U}^{\gamma}$ for each sub-region is solved from (3.8), the sum of the crack-face displacements $\Sigma \boldsymbol{u}^{\gamma}$ on elements adjacent to the crack front is first computed. Then, its components referring to the local coordinate system defined in Figure 2.4 (i.e., $\Sigma \overline{u}_i^{\gamma}$) are obtained and substituted into (2.53)-(2.55) to calculate the finite part of the strain $\overline{\varepsilon}_{11}^{*\gamma}(\boldsymbol{x}_c)$, $\overline{\varepsilon}_{13}^{*\gamma}(\boldsymbol{x}_c)$, $\overline{\varepsilon}_{33}^{*\gamma}(\boldsymbol{x}_c)$ at any point $\boldsymbol{x}_c$. Finally, the T-stress components at any point $\boldsymbol{x}_c$ are obtained by solving a system of six linear algebraic equations (2.52) along with the prescribed conditions (2.46)-(2.48) and the computed finite part of the strain.

CHAPTER 4
NUMERICAL RESULTS AND DISCUSSION

The convergence and accuracy of numerical results obtained from the implemented numerical procedure are first verified by a set of reference solutions for problems associated with cracked multi-material bodies. Both isotropic and anisotropic materials are considered in the numerical experiments. A series of meshes with different levels of refinement is adopted and used in the numerical study to ensure the convergence of numerical solutions. The solution on ordinary boundary (e.g., unknown displacements and tractions), on the material interface (e.g., unknown displacements and tractions), and on the majority of the crack surface (e.g., jump in and sum of the crack-face displacements) are discretized using standard, two-dimensional, isoparametric, quadratic elements. For the solution along the crack front, the jump in the crack-face displacements is approximated by special 9-node crack-tip elements whereas the sum of the crack-face displacements is approximated by standard 9-node quadratic elements. After the implemented technique is fully tested, a preliminary parametric study is conducted to investigate the influence of the material stiffness and the distance between the crack and the material interface on the stress intensity factors and the T-stress. In such investigation, a sufficiently fine mesh is employed to ensure the convergence of numerical results.

4.1 VERIFICATION

In this section, results for two particular problems associated with a three-layer cylinder containing an elliptical crack parallel to the material interface and a three-layer cube containing a penny-shape crack parallel to the material interface are obtained and then compared with existing reference solutions for both stress intensity factors and T-stress.

4.1.1 Elliptical Crack in Three-layer Cylinder

Consider a three-layer cylinder of radius R and length $6d$ as shown schematically in Figure 4.1. Each layer has the same length $2d$ and they are fully bonded with the material interface perpendicular to the axis of the cylinder. All three layers are made of transversely isotropic, linear elastic materials with the axis of material symmetry

directing along the axis of the cylinder. An elliptical crack with the major semi-axis a and the minor semi-axis b is embedded in the center of the middle layer and oriented parallel to the material interface as shown in Figure 4.1. For convenience, a reference Cartesian coordinate system is chosen such that its origin coincides with the center of the crack, the x_3-axis directs along the axis of the cylinder, and the x_1-axis and x_2-axis direct along the major and minor axes of the crack, respectively. With this choice of the coordinate system, the crack front can be parameterized by

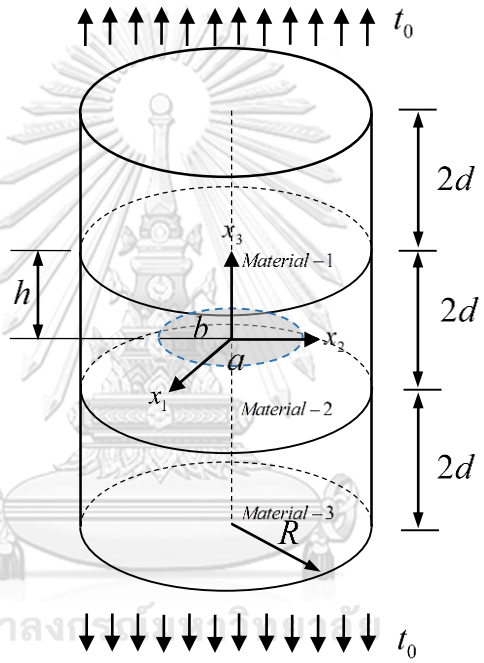

Figure 4.1 Schematic of three-layer cylinder containing elliptical crack in the middle layer with its orientation parallel to material interface

$$x_1 = a\cos\theta,\ x_2 = b\cos\theta,\ x_3 = 0 \tag{4.1}$$

where $\theta \in [0, 2\pi]$ denotes the angular position of point along the crack front. In the analysis, three meshes of the ordinary boundary, the material interfaces, and the crack surface are adopted as shown in Figure 4.2. To allow the comparison with the reference solution generated by a single domain boundary integral equation method proposed by Rungamornrat and Mear (2008b), the material constants of all layers are chosen to be identical to those of transversely isotropic-1 shown in Table 4.1.

The discretization of the ordinary boundary and the crack surface obtained from the Mesh-3 is used to generate the reference solution. In addition, the ratios $d/a=2, a/b=2, R/d=1, h/d=1$ are employed in the numerical study.

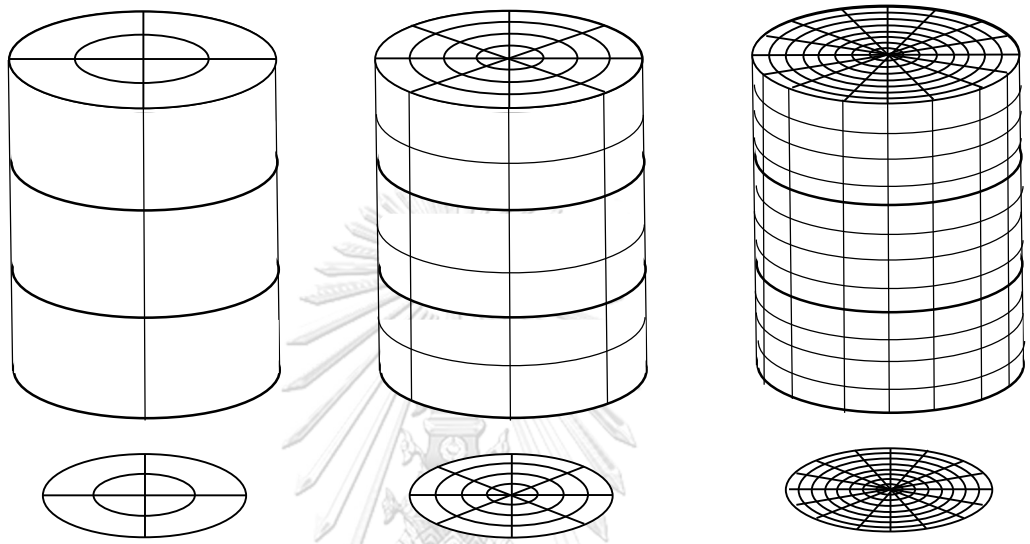

Figure 4.2 Three meshes adopted in the analysis of three-layer cylinder containing elliptical crack; mesh of the crack surface is shown below that of the boundary and mesh for the material interface is taken to be identical to that of the top surface.

Table 4.1 Elastic moduli for two transversely isotropic, linear elastic materials sued in numerical study.

Material type	E_{1111} $\times 10^9$ Pa	E_{1122} $\times 10^9$ Pa	E_{1133} $\times 10^9$ Pa	E_{3333} $\times 10^9$ Pa	E_{1313} $\times 10^9$ Pa
Transversely Isotropic 1	126.00	55.00	53.00	117.00	35.30
Transversely Isotropic 2	139.00	77.80	74.30	113.00	25.60

The normalized mode-I stress intensity factor K_I and the non-zero T-stress components T_{11}, T_{33} obtained from proposed technique for all three meshes are reported as a function of angular position θ along the crack front in Figures 4.3, 4.4 and 4.5, respectively. The reference solutions generated by the technique proposed by Rungamornrat and Mear (2008b) with the Mesh-3 are also reported in those figures. It is seen from this set of results that the implemented technique yields the converged numerical solution which is generally in good agreement with the reference solution. In particular, meshes required to achieve such accurate stress intensity factors are relatively coarse; only few elements employed to discretize the solution along the crack front can accurately capture the fracture data. This is due mainly to the use of special crack-tip element to approximate the near-front relative crack face displacement and the explicit formula used to post-process for the stress intensity factors and the T-stress.

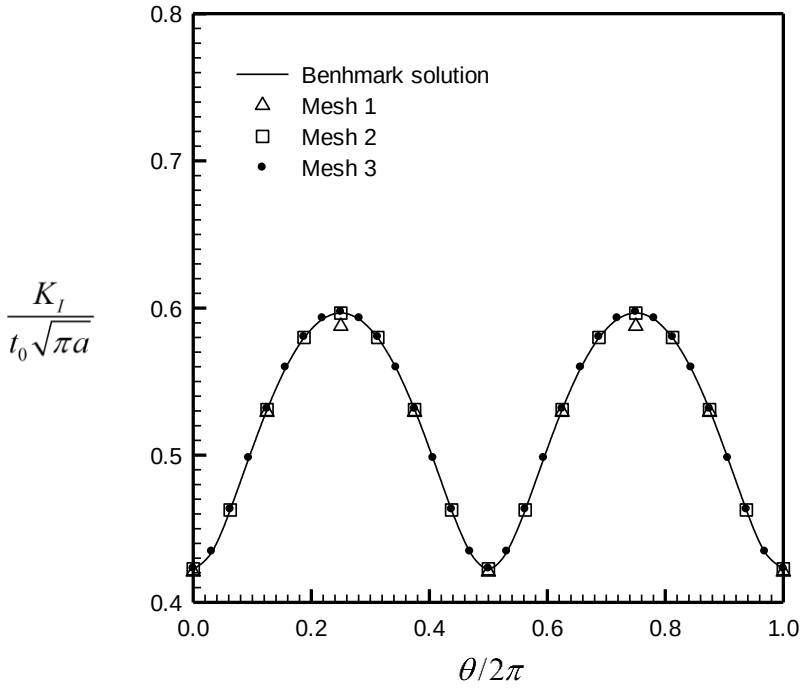

Figure 4.3 Normalized stress intensity factor of elliptical crack contained in three-layer cylinder under uniformly distributed normal traction t_0 at the top and bottom surfaces

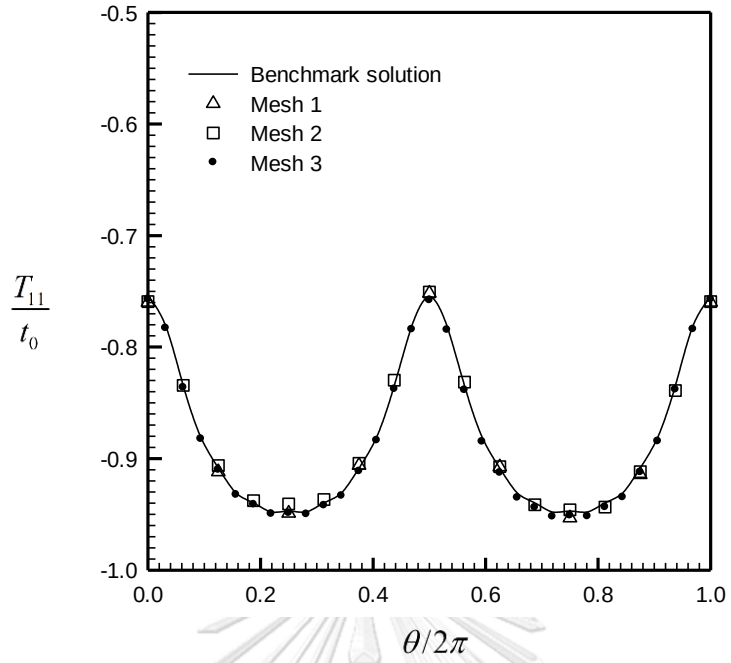

Figure 4.4 Normalized T-stress T_{11} of elliptical crack in three-layer cylinder under uniformly distributed normal traction t_0 at the top and bottom surfaces

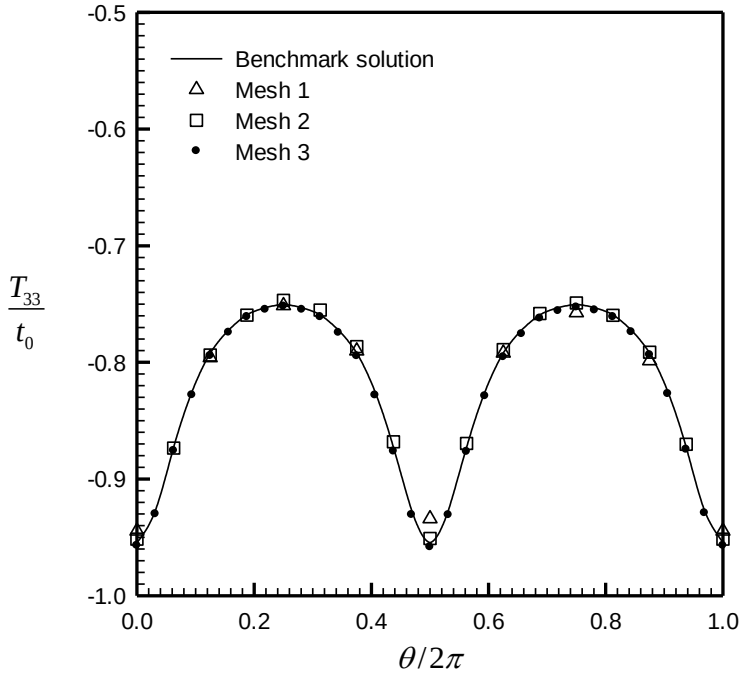

Figure 4.5 Normalized T-stress T_{33} of elliptical crack in three-layer cylinder under uniformly distributed normal traction t_0 at the top and bottom surfaces

4.1.2 Penny-shaped Crack in Three-layer Cube

Consider a three-layer prism with dimensions $2l \times 2s \times 6d$ as shown schematically in Figure 4.6. Each layer has the same thickness $2d$ and they are fully bonded at the material interface perpendicular to the cross section of the cube. Each layer is made of either an isotropic material with given Young modulus and Poisson ratio or a transversely isotropic material with the axis of material symmetry perpendicular to the material interface. The crack contained in the center of the middle layer assumes an elliptical shape with the major semi-axis a and the minor semi-axis b and is oriented parallel to the material interface with the major and minor semi-axes normal to the side face of the prism as shown in Figure 4.6. Again, a reference Cartesian coordinate system is chosen such that its origin coincides with the center of the crack, the x_3-axis directs normal to the material interface, and the x_1-axis and x_2-axis direct along the major and minor axes of the crack, respectively. With this choice of the coordinate system, the crack front can be parameterized by (4.1). The prism is subjected to uniformly distributed normal tractions t_3 on the top and bottom surfaces and uniformly distributed normal tractions t_{11}, t_{12}, t_{13} on the two side faces of each layer. Three meshes for the outer boundary, the material interfaces and the crack surface shown in Figure 4.7 and the following geometric data $d/a = 3, h/d = 1$ are employed in the simulations.

4.1.2.1 Three identical material layers under $t_{11} = t_{12} = t_{13}$

First, consider the case that each layer is made of the same isotropic material with Young modulus $E = 1\ GPa$ and Poisson ratio $\nu = 0.3$, the prism is subjected to the uniform normal traction $t_{11} = t_{12} = t_{13} = t_0$, $t_3 = 0$, and the crack is of a penny shape (i.e., $a/b = 1$). For this particular case, the jump in the crack-face displacements identically vanishes and, as the result, all the stress intensity factors vanish for the entire crack front whereas the closed-form solution of the T-stress components can be readily obtained and used, here, as the benchmark solutions. Numerical results for the stress intensity factors obtained from all three meshes agree very well with the reference solution; in particular, results are nearly zero up to several digits. For the T-stress components, the computed solutions from the three meshes after

normalized by the applied load, are reported along with the exact solution in Figures 4.8, 4.9 and 4.10 for T_{11}, T_{33}, T_{13}, respectively.

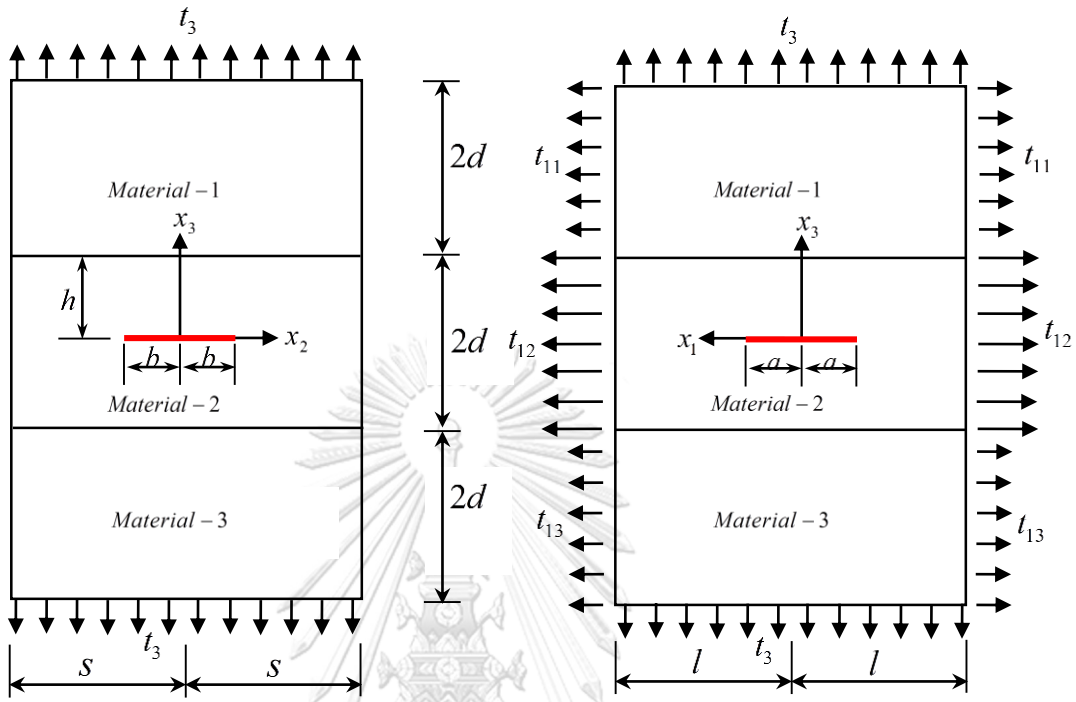

Figure 4.6 Schematic of three-layer cube containing elliptical crack parallel to material interface under uniformly distributed normal tractions t_{10} and t_{20}.

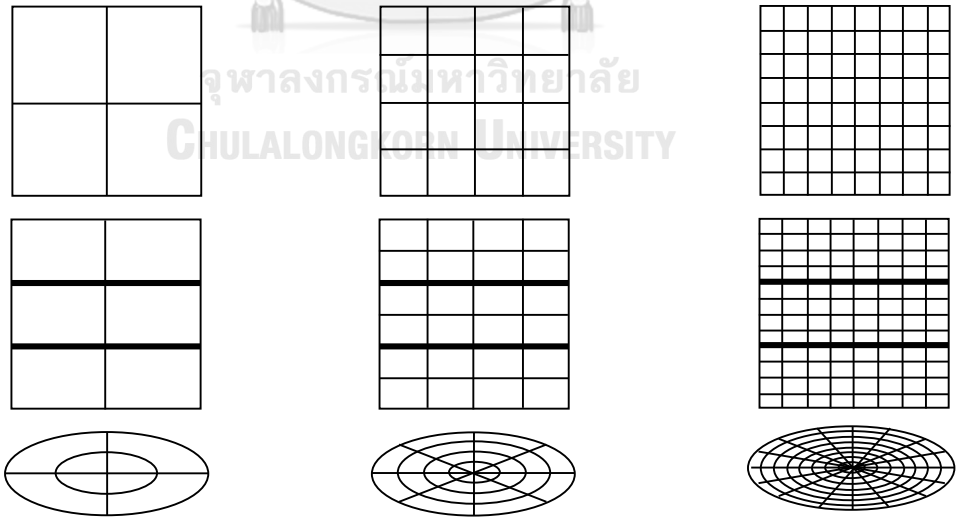

Mesh-1 Mesh-2 Mesh-3

Figure 4.7 Three meshes adopted in the analysis of three-layer prism containing elliptical crack; mesh of the crack surface is shown below that of the side faces and mesh for the top and bottom faces and the material interface is shown at the top.

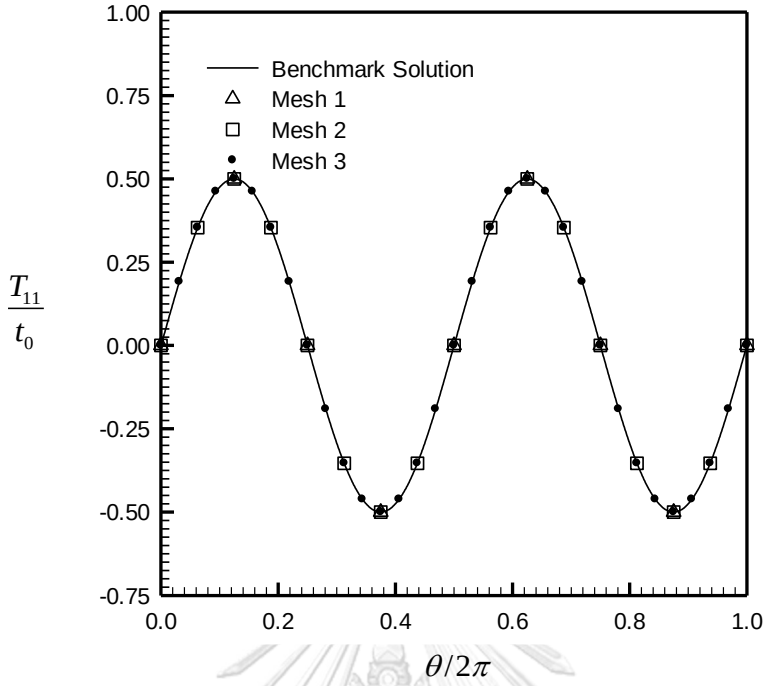

Figure 4.8 Normalized T-stress T_{11} of penny-shaped crack in three-layer isotropic prism under uniform normal traction t_0 at the two side faces

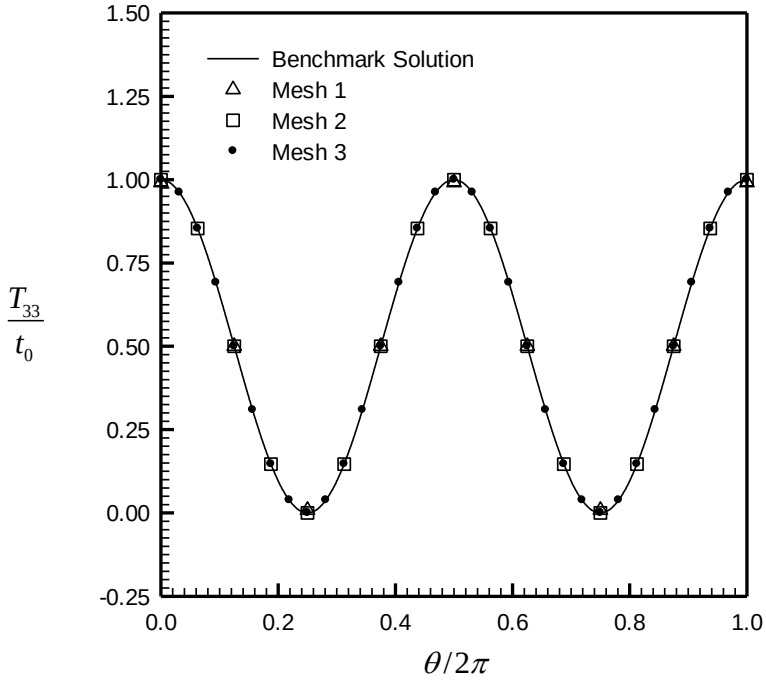

Figure 4.9 Normalized T-stress T_{33} of penny-shaped crack in three-layer isotropic prism under uniform normal traction t_0 at the two side faces

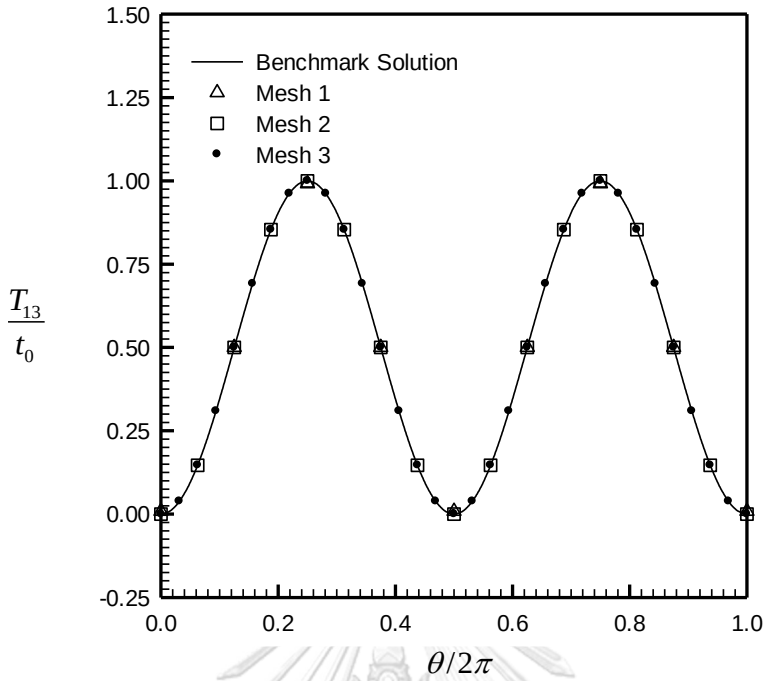

Figure 4.10 Normalized T-stress T_{13} of penny-shaped crack in three-layer isotropic prism under uniform normal traction t_0 at the two side faces

Next, consider the same prism as indicated above except that each layer is made of the same transversely isotropic material (i.e., transversely isotropic 1 with material constant shown in Table 4.1). Similar to the previous case, the jump in the crack-face displacements identically vanishes and all the stress intensity factors are zero for the entire crack front whereas the closed-form solution of the T-stress components can be obtained in the same manner. Again, the computed stress intensity factors from the proposed technique are nearly zero up to several digits and results are not presented here for brevity. Figures 4.11, 4.12 and 4.13 report the T-stress components for the three meshes along with the exact solutions.

It can be seen for both cases of isotropic and transversely isotropic that results obtained exhibit the good convergence behavior; in particular, the T-stress components are slightly dependent on the level of refinement. In addition, the convergence of the solution shows the excellent agreement with the exact solution. The coarsest mesh with only few elements can also capture the solution with sufficient accuracy.

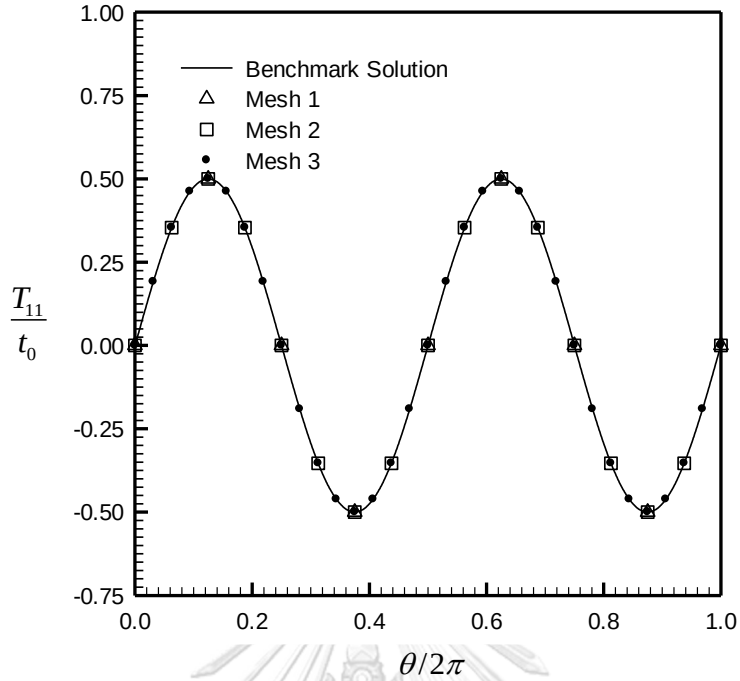

Figure 4.11 Normalized T-stress T_{11} of penny-shaped crack in three-layer transversely isotropic prism under uniform normal traction t_0 at the two side faces

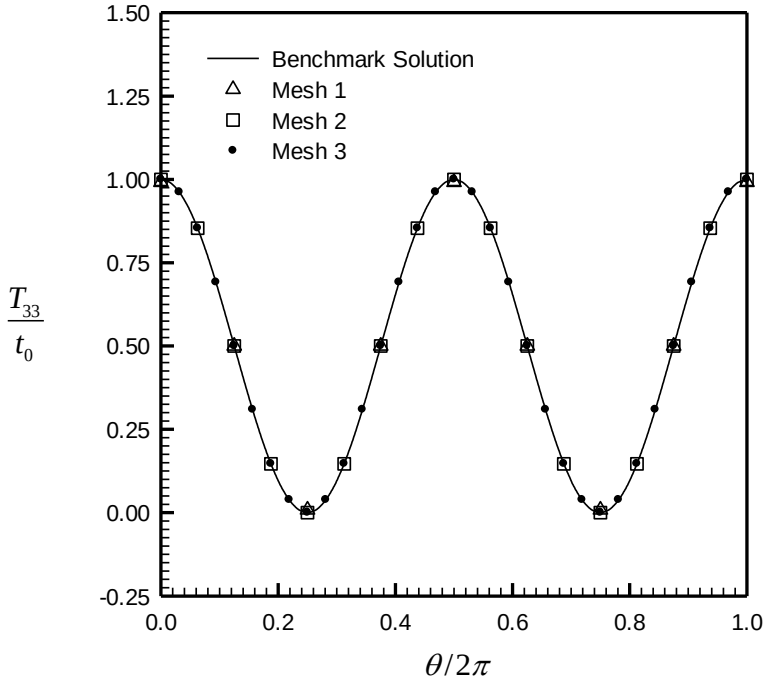

Figure 4.12 Normalized T-stress T_{33} of penny-shaped crack in three-layer transversely isotropic prism under uniform normal traction t_0 at the two side faces

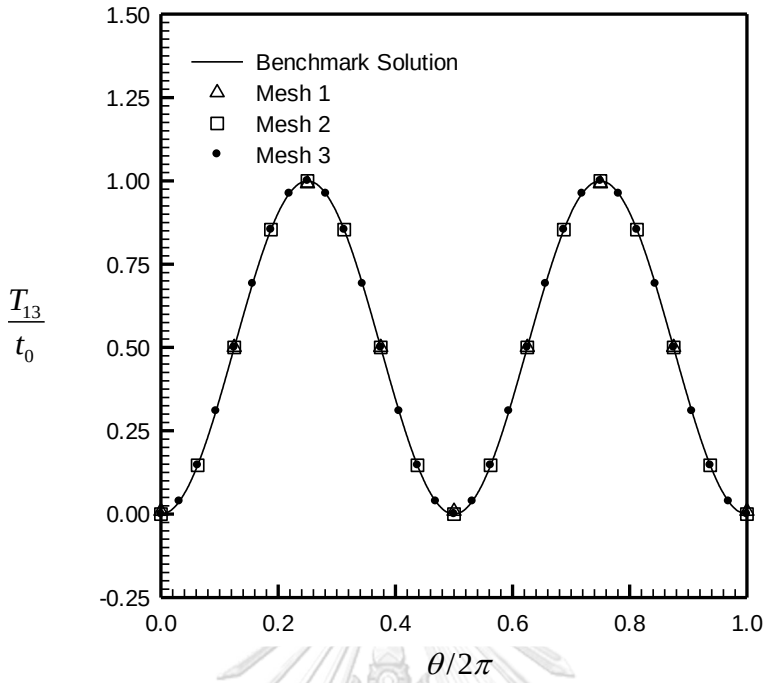

Figure 4.13 Normalized T-stress T_{13} of penny-shaped crack in three-layer transversely isotropic prism under uniform normal traction t_0 at the two side faces

4.1.2.2 Different material layers under t_{12} and $t_{11} = t_{13}$

Next, consider the case that the top and bottom layers are made of the same materials, either the isotropic material with Young modulus $E = 1\ GPa$ and Poisson ratio $\nu = 0.3$ or the transversely isotropic material with material constants identical to the transversely isotropic 1 reported in Table 4.1, whereas the middle layer is made from the different material. The prism is subjected to the uniform normal traction $t_{11} = t_{13} = 2t_0, t_{12} = t_0$, and contained the penny-shaped crack (i.e., $a/b = 1$). As the purpose of verification, the material constituting the middle layer is chosen such that the crack is completely closed under the applied traction and the T-stress components can be readily obtained in a closed-form. For the isotropic case, Young modulus $E = 2\ GPa$ and Poisson ratio $\nu = 0.3$ are chosen whereas for the transversely isotropic case, the material constants are chosen such that $E_{1111} = 252$ GPa, $E_{1122} = 110$ GPa, $E_{1133} = 106$ GPa, $E_{3333} = 234$ GPa, $E_{1313} = 35.3$ GPa. As expected, the computed stress intensity factors from all three meshes for both the isotropic and transversely isotropic cases are nearly zero up to several digits. For the

T-stress components, results for T_{11}, T_{33}, T_{13} along the crack front obtained from the three meshes are normalized and then reported along with the analytical solution in Figures 4.14-4.16 for the isotropic case and Figures 4.17-4.19 for the transversely isotropic case. Again, this set of results confirms both the convergence and accuracy of the numerical solutions obtained from the proposed boundary integral equation method and the post-process for determining the T-stress components from the sum of the crack-face displacement data. In particular, the obtained solutions are highly accurate and almost indistinguishable from the reference solutions. The coarse mesh containing only few elements can also capture the solution slightly different from the exact solution. This finding confirms the advantage of using special crack-tip elements to approximate the near-front jump in the crack-face displacement.

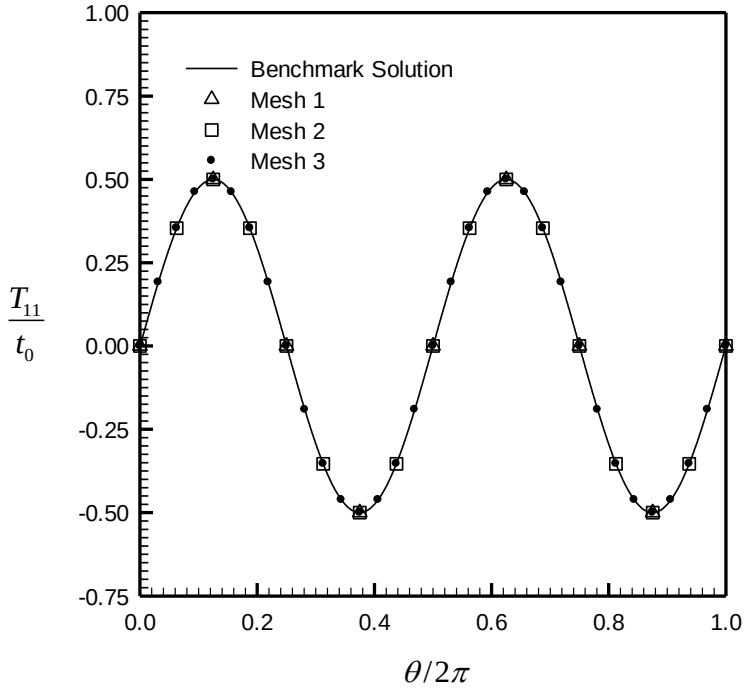

Figure 4.14 Normalized T-stress T_{11} of penny-shaped crack in three-layer isotropic prism under $t_{11} = t_{13} = 2t_0, t_{12} = t_0$ at the two side faces

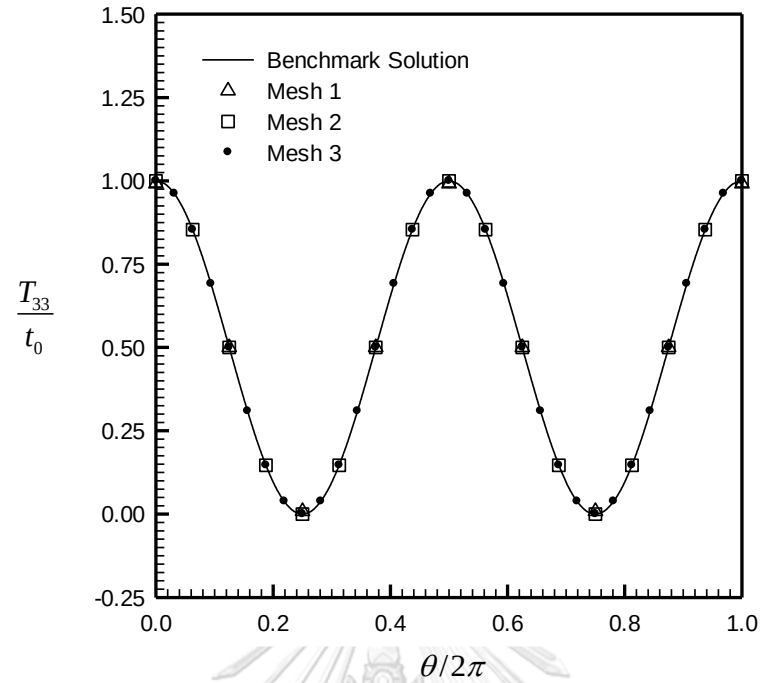

Figure 4.15 Normalized T-stress T_{33} of penny-shaped crack in three-layer isotropic prism under $t_{11} = t_{13} = 2t_0, t_{12} = t_0$ at the two side faces

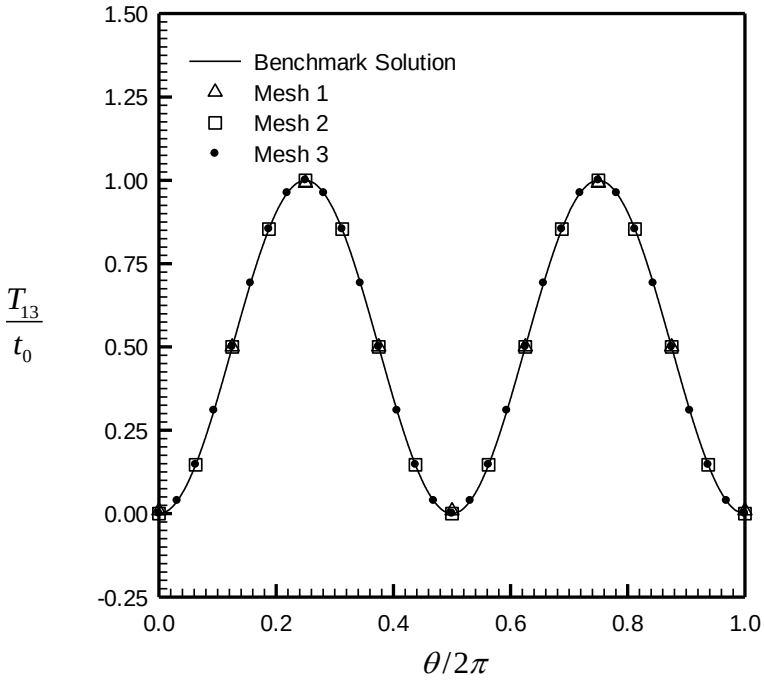

Figure 4.16 Normalized T-stress T_{13} of penny-shaped crack in three-layer isotropic prism under $t_{11} = t_{13} = 2t_0, t_{12} = t_0$ at the two side faces

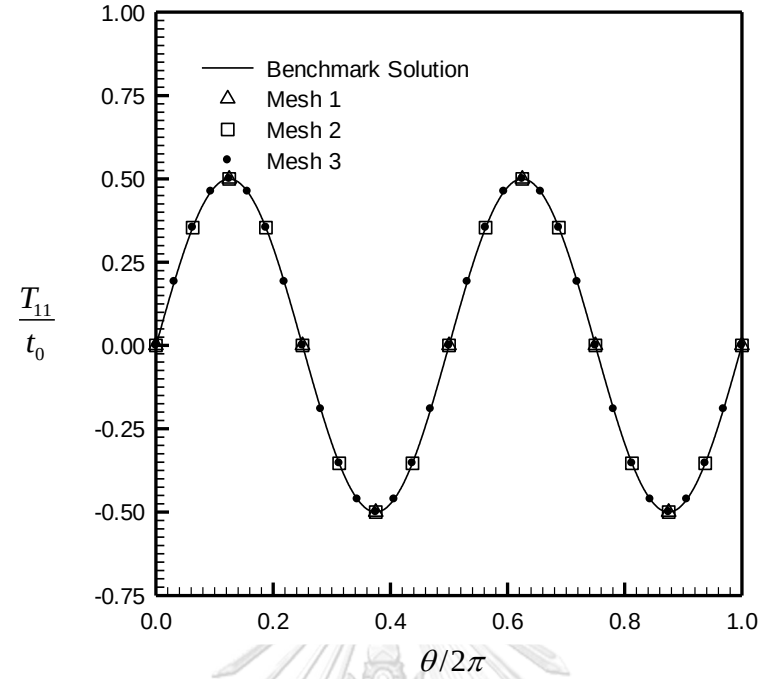

Figure 4.17 Normalized T-stress T_{11} of penny-shaped crack in three-layer transversely isotropic prism under $t_{11} = t_{13} = 2t_0, t_{12} = t_0$ at the two side faces

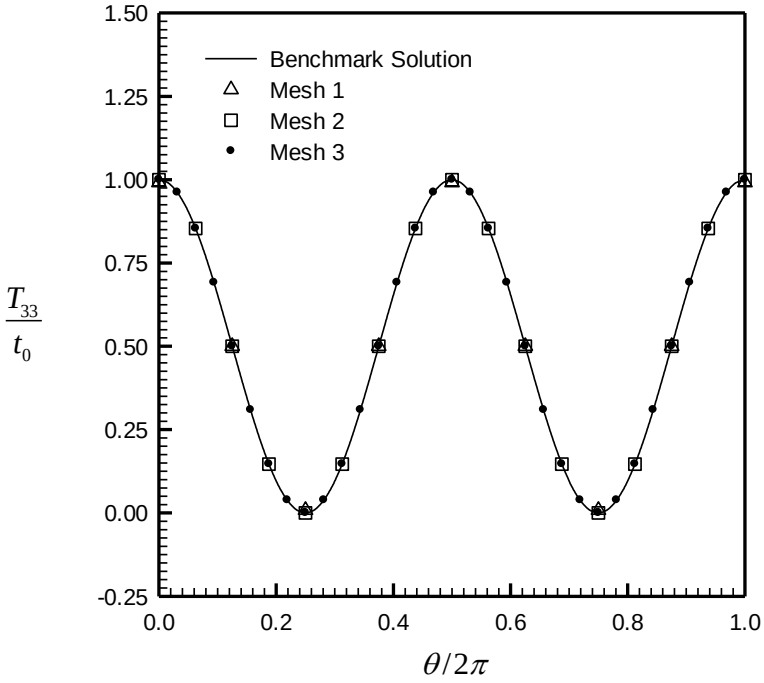

Figure 4.18 Normalized T-stress T_{33} of penny-shaped crack in three-layer transversely isotropic prism under $t_{11} = t_{13} = 2t_0, t_{12} = t_0$ at the two side faces

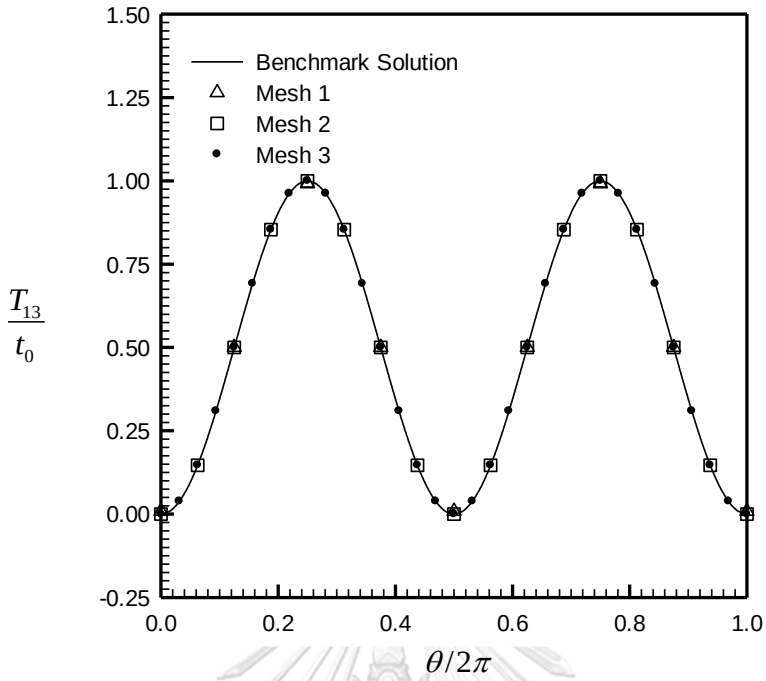

Figure 4.19 Normalized T-stress T_{13} of penny-shaped crack in three-layer transversely isotropic prism under $t_{11} = t_{13} = 2t_0, t_{12} = t_0$ at the two side faces

4.1.2.3 Three identical material layers under t_3

Finally, consider the case that all three layers are made of the same materials, either the isotropic material with Young modulus $E = 1\ GPa$ and Poisson ratio $\nu = 0.3$ or the transversely isotropic material with material constants identical to the transversely isotropic 1 reported in Table 4.1. The prism is subjected only to the uniform normal traction $t_3 = t_0$ with $t_{11} = t_{12} = t_{13} = 0$ and contained the elliptical crack with aspect ratio $a/b = 2$. Due to the symmetry with respect to the crack plane, only the mode-I stress intensity factor K_I and the two T-stress components T_{11}, T_{33} are non-zero along the crack front. Results for K_I and T_{11}, T_{33} obtained from the three meshes shown in Figure 4.8 are reported in Figures 4.20-4.22 for the isotropic case and Figures 4.23-4.25 for the transversely isotropic case. Computed solutions are compared with the reference solutions generated by the technique proposed by Rungamornrat and Mear (2008b) using the single domain formulation.

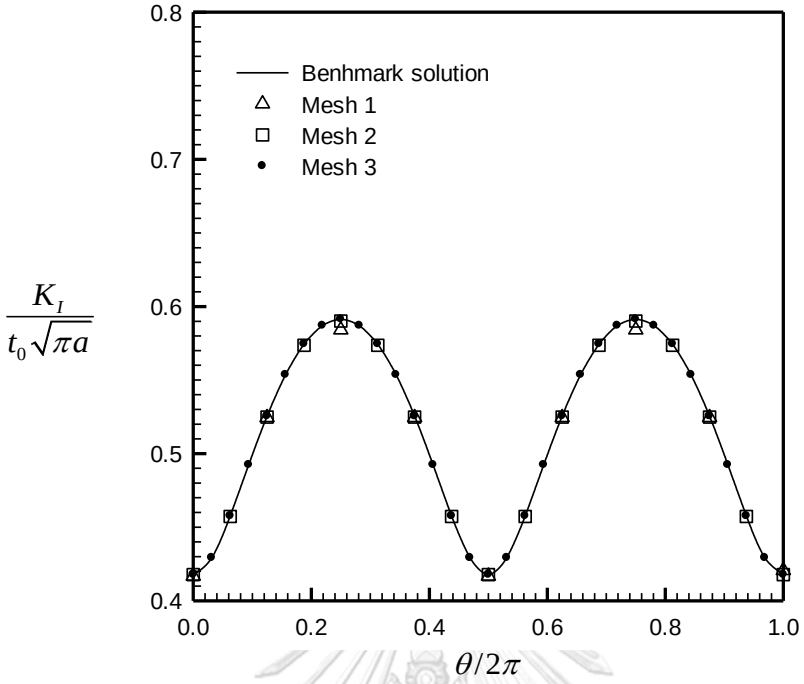

Figure 4.20 Normalized stress intensity factor K_I for elliptical crack in three-layer isotropic prism under uniform normal traction $t_3 = t_0$ at top and bottom surfaces

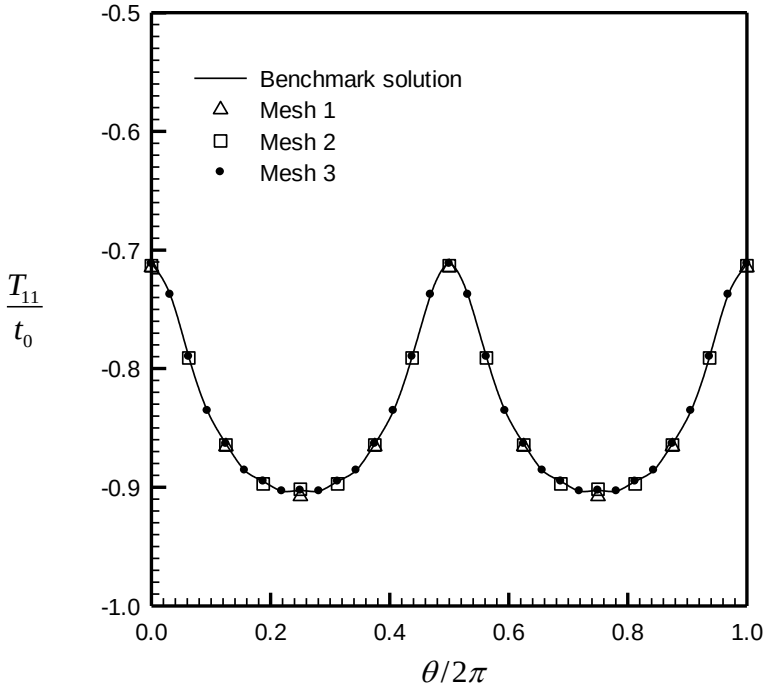

Figure 4.21 Normalized T-stress T_{11} for elliptical crack in three-layer isotropic prism under uniform normal traction $t_3 = t_0$ at top and bottom surfaces

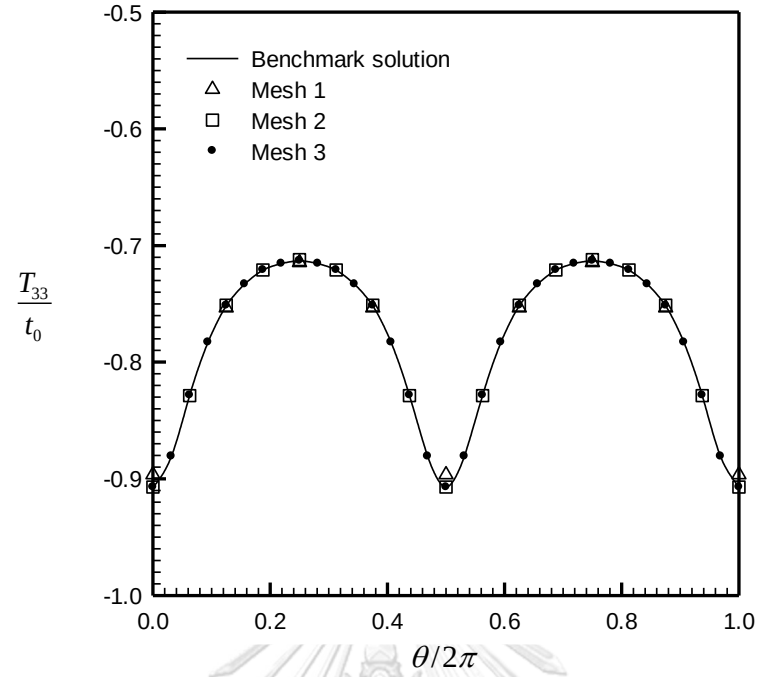

Figure 4.22 Normalized T-stress T_{33} for elliptical crack in three-layer isotropic prism under uniform normal traction $t_3 = t_0$ at top and bottom surfaces

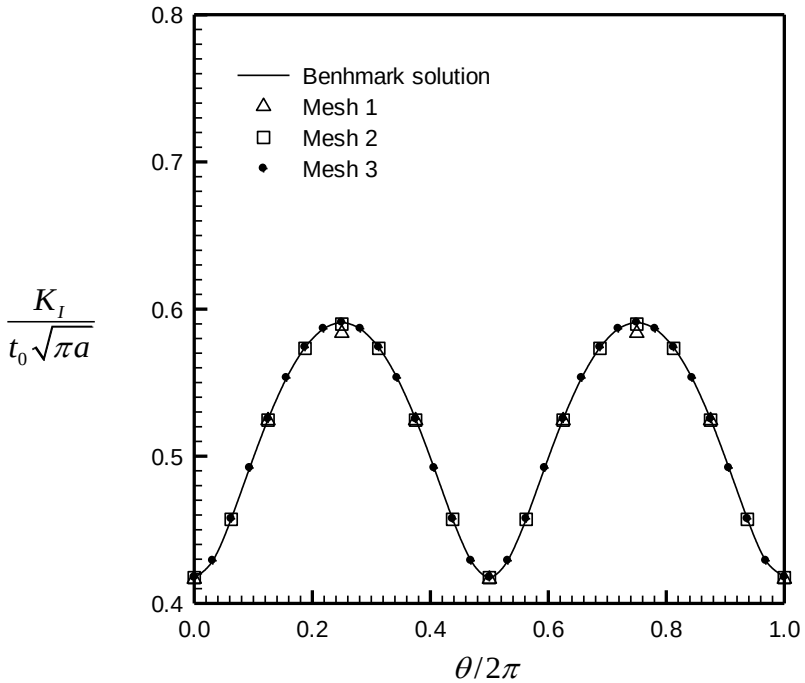

Figure 4.23 Normalized K_I for elliptical crack in transversely isotropic three-layer prism under uniform normal traction $t_3 = t_0$ at top and bottom surfaces

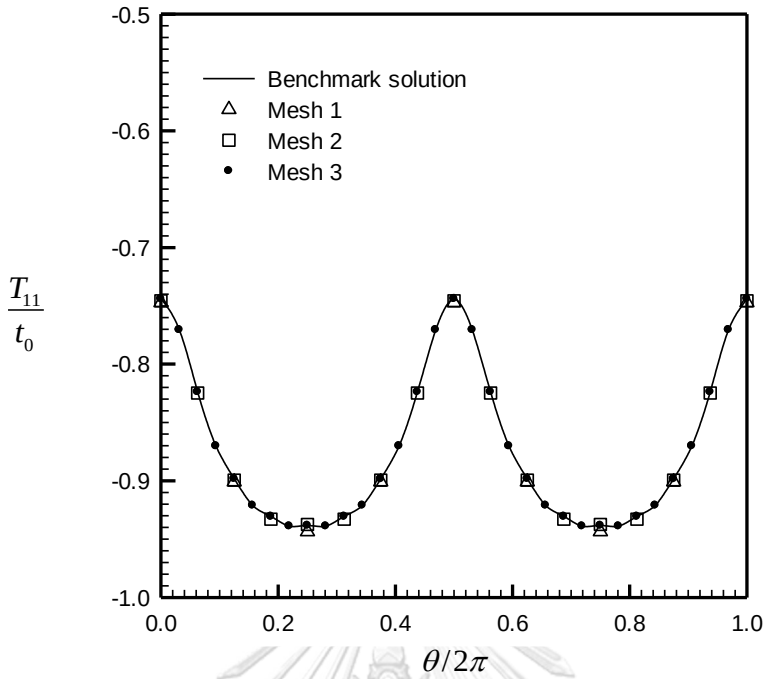

Figure 4.24 Normalized T-stress T_{11} for elliptical crack in three-layer prism under uniform normal traction $t_3 = t_0$ at top and bottom surfaces

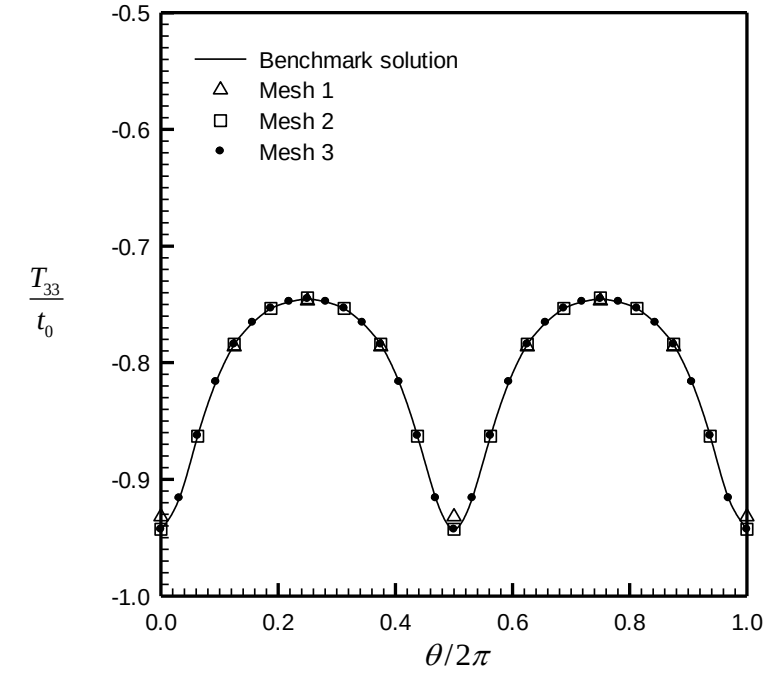

Figure 4.25 Normalized T-stress T_{33} for elliptical crack in three-layer prism under uniform normal traction $t_3 = t_0$ at top and bottom surfaces

Again, it can be concluded from the last set of results that implemented technique yields the converged numerical solutions and they are in excellent agreement with the benchmark solution for both stress intensity factors and T-stress components.

4.1.3 Elliptical Crack in Two-layer Cube

Consider a two-layer cube occupying the region $[-2d,2d]\times[-2d,2d]\times[-2d,2d]$ as shown in Figure 4.26. The two layers are of the same height $2d$, made of transversely isotropic, linear elastic materials with the axis of material symmetry along the x_3-axis, and fully bonded with the material interface perpendicular to the x_3-axis. An elliptical crack with the major semi-axis a and the minor semi-axis b is embedded in the bottom layer and oriented perpendicular to the material interface as shown in Figure 4.26. In particular, the crack front can be described by

$$x_1 = 0,\ x_2 = a\cos\theta,\ x_3 = -h - b\sin\theta \tag{4.2}$$

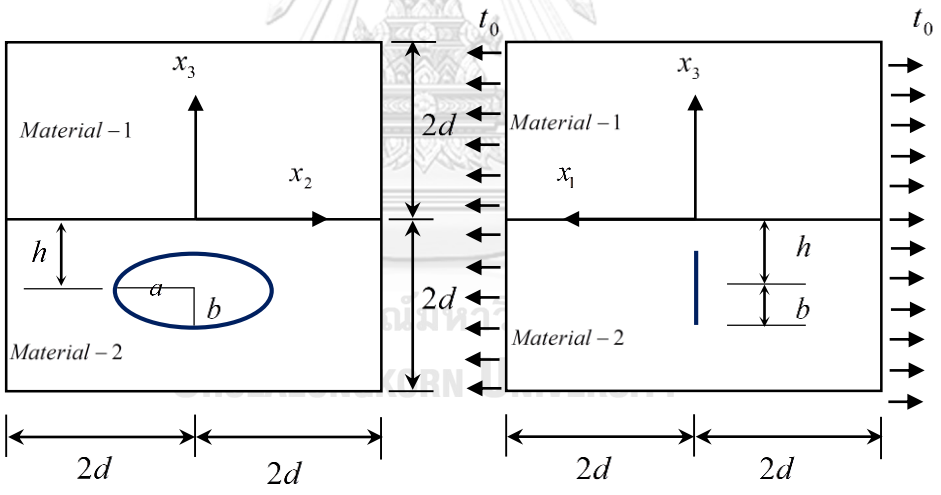

Figure 4.26 Two-layer cube containing elliptical crack perpendicular to interface under uniform traction on ordinary boundary in x_2 direction.

where h is the distance from the crack center to the material interface and $\theta\in[0,2\pi]$ denotes the angular position of point along the crack front. The body is free of the body force and loaded by a uniformly distributed normal traction t_0 on the two side faces normal to the x_1-axis. Meshes used in the analysis are indicated in Figure 4.27, the material constants of all layers are chosen to be identical to those

of transversely isotropic-1 shown in Table 4.1. The discretization of the ordinary boundary and the crack surface obtained from the Mesh-3 is used along with the technique proposed by Rungamornrat and Mear (2008b) to generate the reference. In particular, the ratios $d/a=1, a/b=2, h/d=1$ are employed in the numerical study.

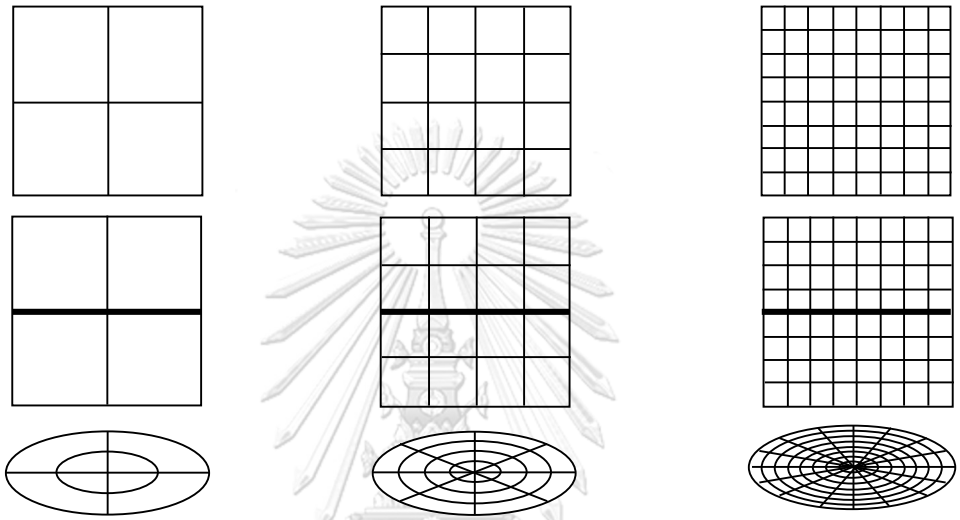

Figure 4.27 Three meshes adopted in the analysis of two-layer cube containing elliptical crack; mesh of the crack surface is shown below that of the side faces whereas mesh for the top and bottom faces and the material interface is shown at the top.

The normalized mode-I stress intensity factor K_I and the non-zero normalized T-stress components T_{11}, T_{33} obtained from proposed technique for all three meshes are reported as a function of the angular position θ along the crack front in Figures 4.28-4.30, respectively. It is seen from these results that the computed solutions show the good agreement with the reference solutions; in particular, the numerical solutions generated by the Mesh-2 and the Mesh-3 are almost indistinguishable from the reference solution whereas only slight difference is observed for those generated from the Mesh-1.

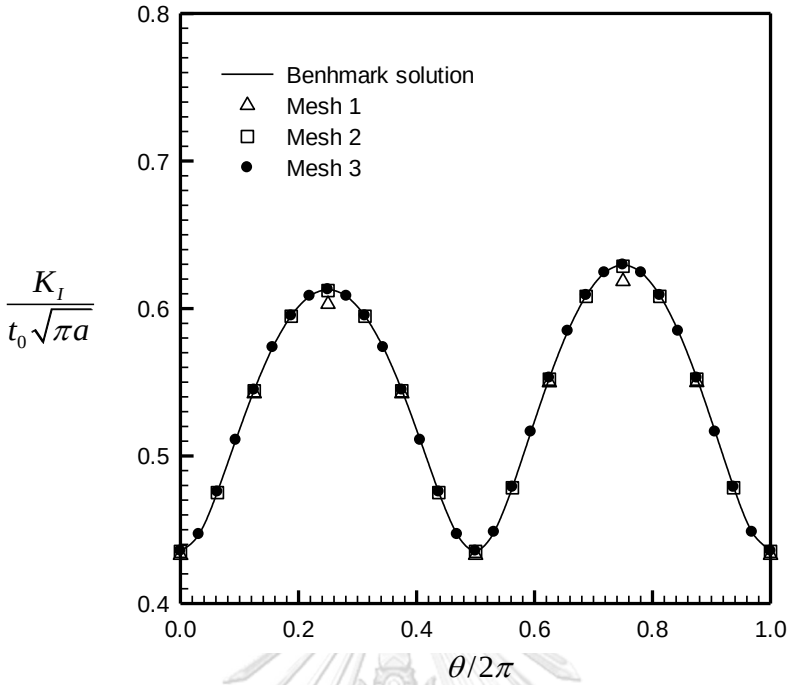

Figure 4.28 Normalized mode-I stress intensity factor for elliptical-shaped crack in two-layer cube under uniform normal traction t_0 at two side faces

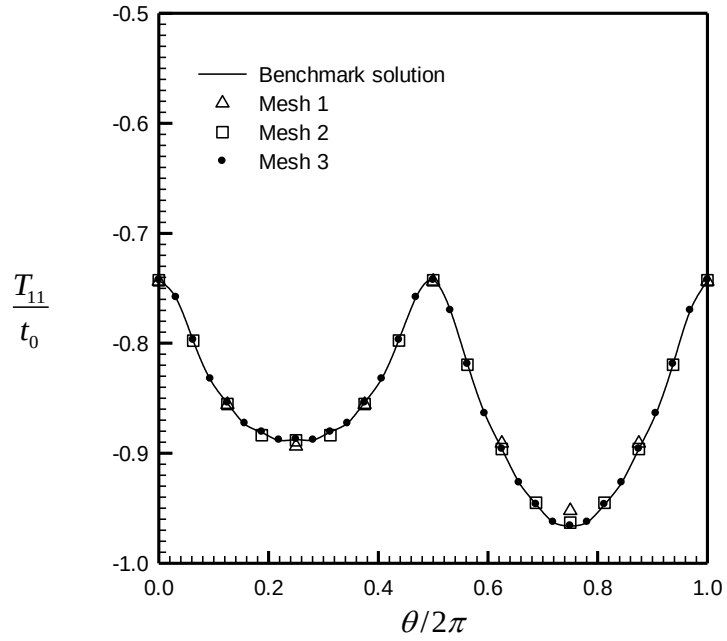

Figure 4.29 Normalized T-stress T_{11} of elliptical crack in two-layer cube under uniformly distributed normal traction t_0 at two side faces

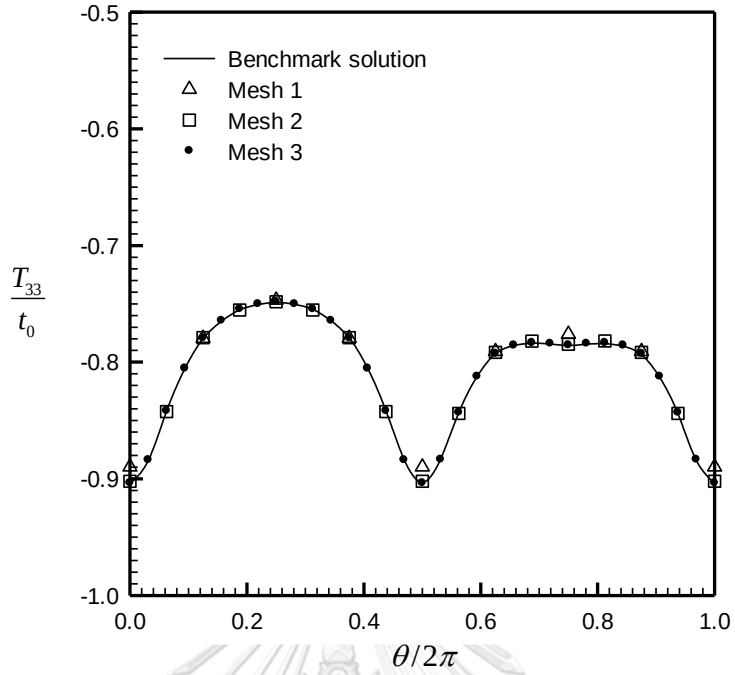

Figure 4.30 Normalized T-stress T_{33} of elliptical crack in two-layer cube under uniformly distributed normal traction t_0 at two side faces

4.2 PARAMETRIC STUDY

After the proposed technique is fully tested, it is then used to investigate the influence of material stiffness and the distance between the crack and the material interface on the stress intensity factors and the T-stress along the crack front. Sufficiently fine meshes suggested from the verification process are employed to ensure the convergence of numerical solutions.

4.2.1 Elliptical Crack in Three-layer Cylinder

To investigate the influence of the contrast between the material stiffness constituting a region containing the crack and those containing no crack on the two essential fracture data (i.e., the stress intensity factors and the T-stress components), the three-layer cylinder containing an elliptical crack as shown schematically in Figure 4.1 is considered as the representative problem. In the numerical study, the top and bottom layers are made of the same material with Young modulus E_1 and Poisson ratio $\nu = 0.3$ whereas the middle layer is made of the different isotropic material with Young modulus E_2 and Poisson ratio $\nu = 0.3$. The elliptical crack is

located at the center of the middle layer (i.e., $h/d=1$) and the cylinder is subjected to the uniformly distributed tractions at the top and bottom surfaces.

First, the stress intensity factors and the T-stress components are generated for the case of a penny-shaped crack ($a/b=1, a/d=0.5$) for various values of the Young modulus ratio E_1/E_2. Results of the mode-I stress intensity factor K_I and the non-zero T-stress T_{11}, T_{33} are reported as a function of E_1/E_2 in Figures 4.31 and 4.32, respectively. It is seen that as the stiffness of the material for the top and bottom layers decreases relative to that of the material for the layer containing crack, both the stress intensity factor and the magnitude of the both T-stress components decreases monotonically. Results are also established for the case of an elliptical crack with $a/b=1, a/d=0.5$ for various values of E_1/E_2. The stress intensity factors and the non-zero T-stress components are reported along the crack front for different values of the Young modulus ratio in Figures 4.33-4.35.

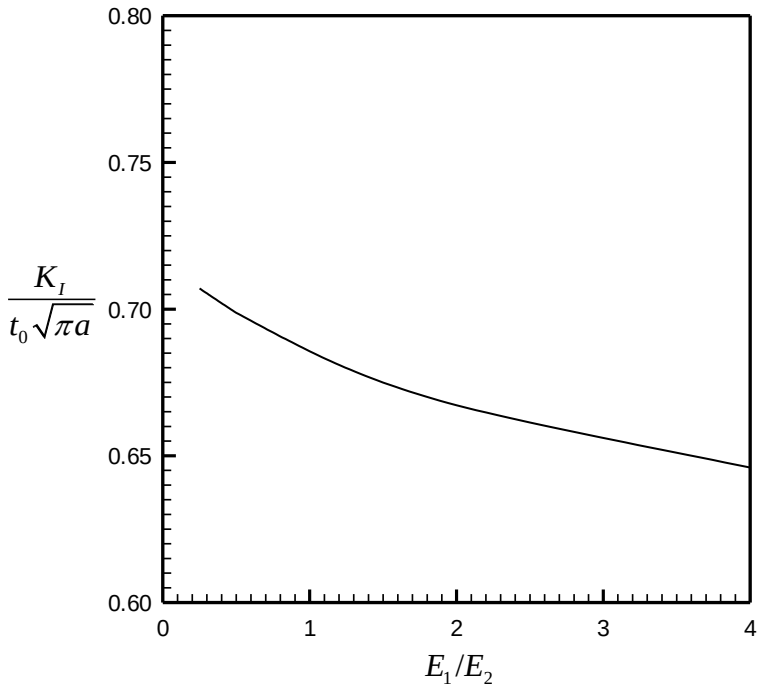

Figure 4.31 Normalized mode-I stress intensity factor for penny-shaped crack in three-layer cylinder under uniform normal traction t_0 as function of E_1/E_2

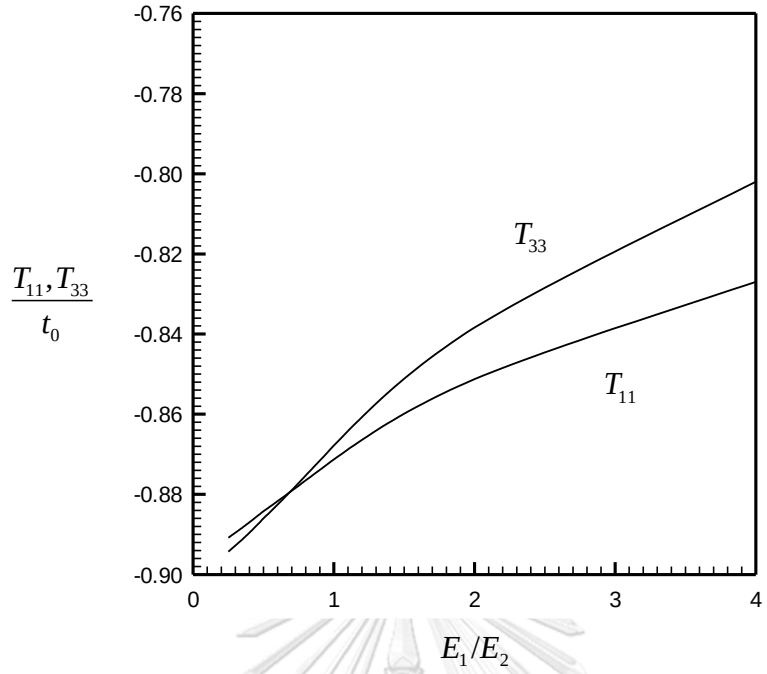

Figure 4.32 Normalized T-stress components T_{11}, T_{33} for penny-shaped crack in three-layer cylinder under uniform normal traction t_0 as function of E_1/E_2

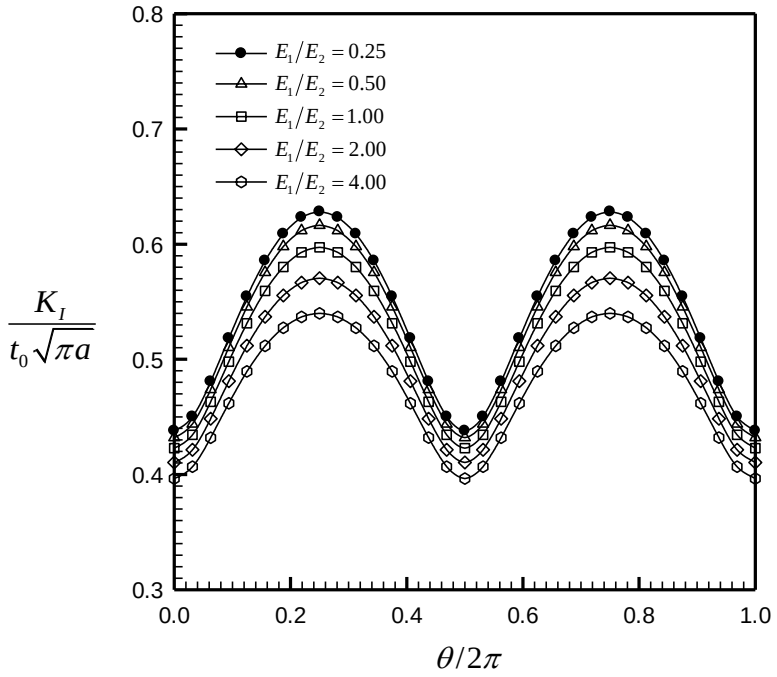

Figure 4.33 Normalized mode-I stress intensity factor for elliptical crack in three-layer cylinder under uniform normal traction t_0 for various values of E_1/E_2

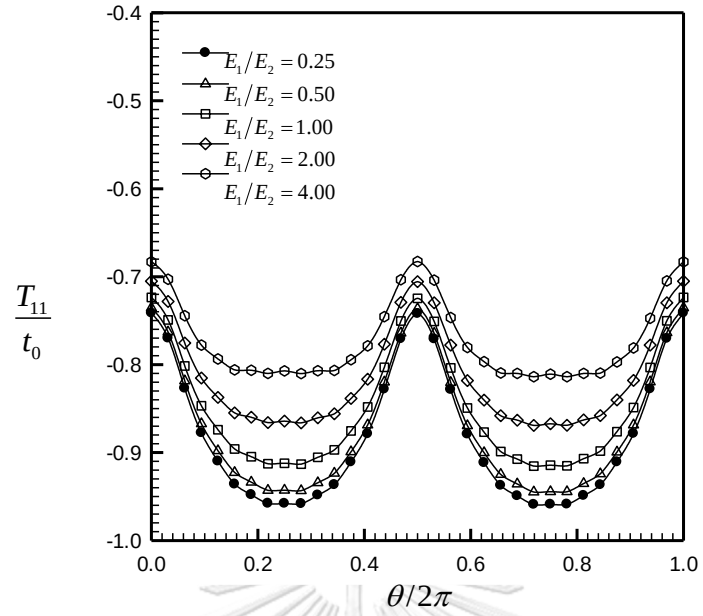

Figure 4.34 Normalized T-stress T_{11} for elliptical crack in three-layer cylinder under uniform normal traction t_0 for various values of E_1/E_2

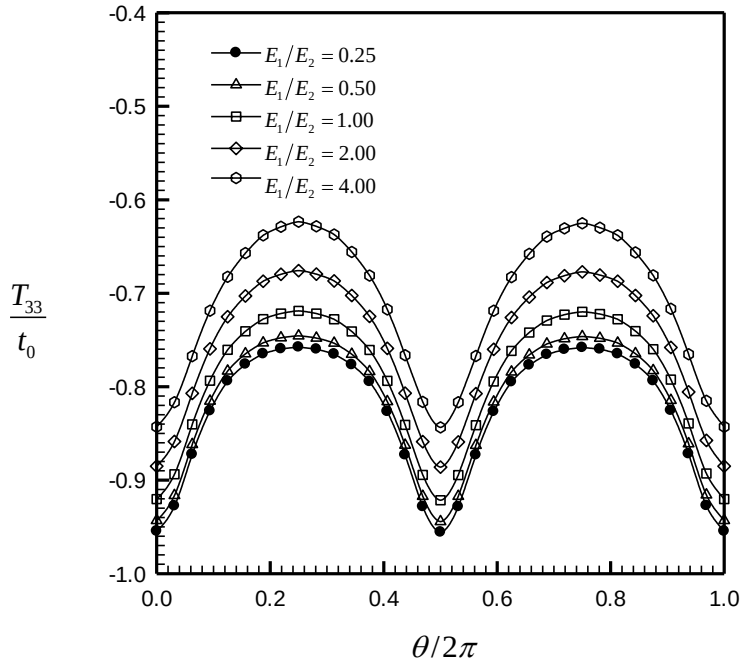

Figure 4.35 Normalized T-stress T_{33} for elliptical crack in three-layer cylinder under uniform normal traction t_0 for various values of E_1/E_2

It is seen that as the material of the layer containing crack becomes stiffer relative to that of the top and bottom layers, the stress intensity factors and the T-stress decreases. While the observed results have the same trend as that for case of the penny-shaped crack, the behavior strongly depends on the location along the crack front.

4.2.2 Penny-shaped Crack in Two-layer Prism

To further investigate the influence of the distance between the crack and the material interface on the stress intensity factors and the T-stress along the crack front, a two-layer prism containing a penny-shaped crack shown in Figure 4.36 is considered. The whole body occupies the region $[-2d,2d]\times[-2d,2d]\times[-8d,2d]$ where its upper part (occupying the region $[-2d,2d]\times[-2d,2d]\times[0,2d]$) is made of an isotropic material with Young's modulus E_1 and Poisson's ratio $\nu = 0.3$ and the remaining part occupying the region $[-2d,2d]\times[-2d,2d]\times[-8d,0]$) is made of an isotropic material with Young's modulus E_2 and Poisson's ratio $\nu = 0.3$. A penny-shaped crack of radius a is embedded within the bottom layer and oriented perpendicular to the material interface with the crack front parameterized by (4.2). In the numerical study, a mesh shown in Figure 4.37 with $d/a = 2$ is used.

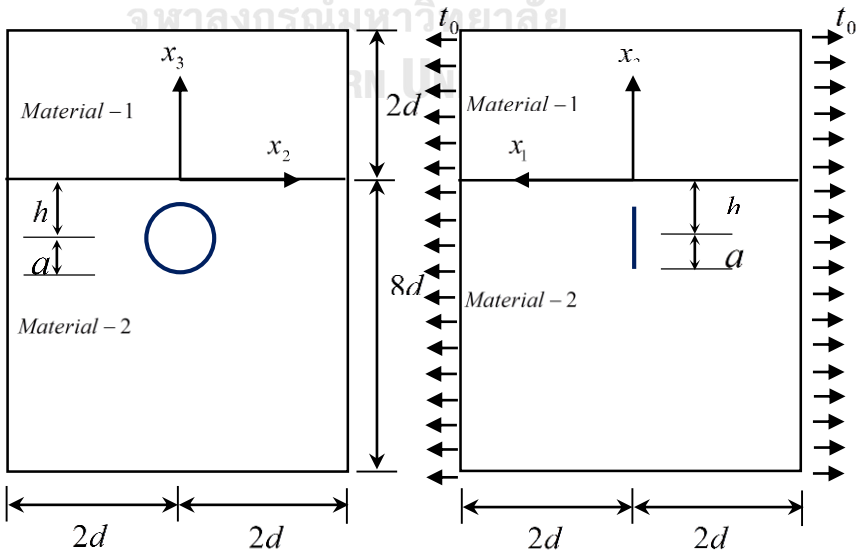

Figure 4.36 Two-layer prism containing penny shaped crack perpendicular to material interface under uniform traction at two side faces

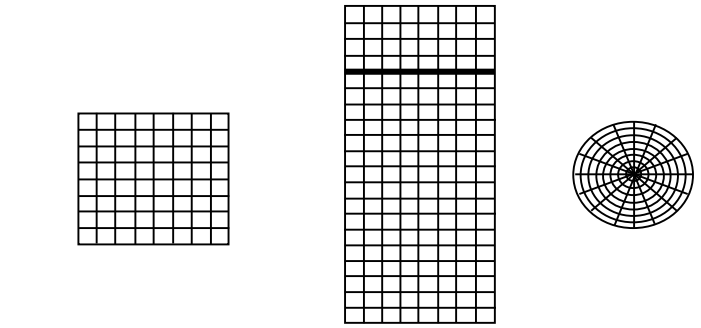

Figure 4.37 Mesh of boundary and crack surface adopted in the analysis of penny-shaped crack in two-layer prism

First, the influence of the distance h on the stress intensity factor and the T-stress components is investigated for $E_1/E_2 = 2$. Computed results for non-zero stress intensity factors and T-stress are reported along the crack front in Figures 4.38-4.40 for various values of $h/2a$ (i.e., $h/2a = 0.6, 0.8, 1.0, 1.2, 1.4, 3.0, 4.0$). Results obtained indicate that when the distance from the crack center to the material interface increases, the mode-I stress intensity factor increases whereas the T-stress components are negative and increase in magnitude for the entire crack front. Both the stress intensity factor and the T-stress components achieves the maximum and minimum values at $\theta = 3\pi/2$ and $\theta = \pi/2$, respectively. Clearly, the influence of the material contrast on the value and distribution of the two fracture parameters is significant when crack is located relatively close to the material interface, and such the influence decays as the normalized distance from the material interface $h/2a$ increases. Both the stress intensity factor and the T-stress components tend to converge asymptotically to the solution of the same crack embedded in a sufficiently long prism made of a single material with Young's modulus E_2 and Poisson's ratio ν. Quantitatively, when the distance from the material interface is greater than about three times of the size of the crack, the influence of the material contrast can be neglected in the modeling without loss of the accuracy.

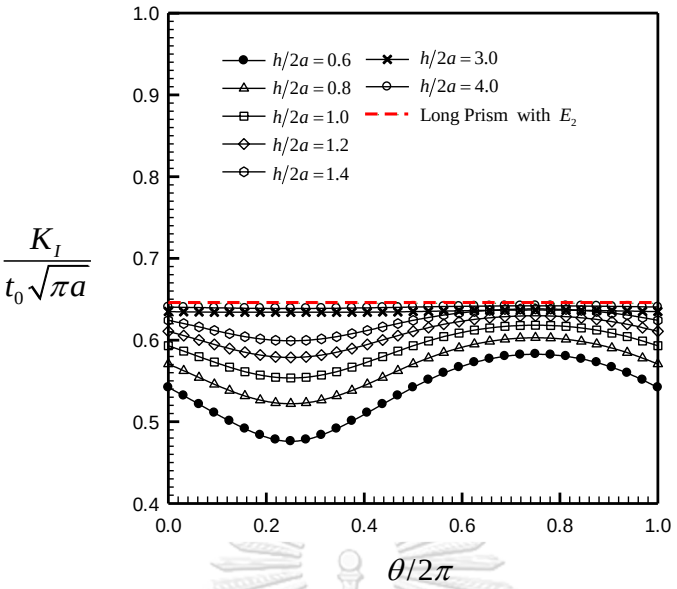

Figure 4.38 Normalized mode-I stress intensity factor for penny-shaped crack in two-layer isotropic prism under uniform normal traction t_0 for $E_1/E_2 = 2$ and various values of $h/2a$

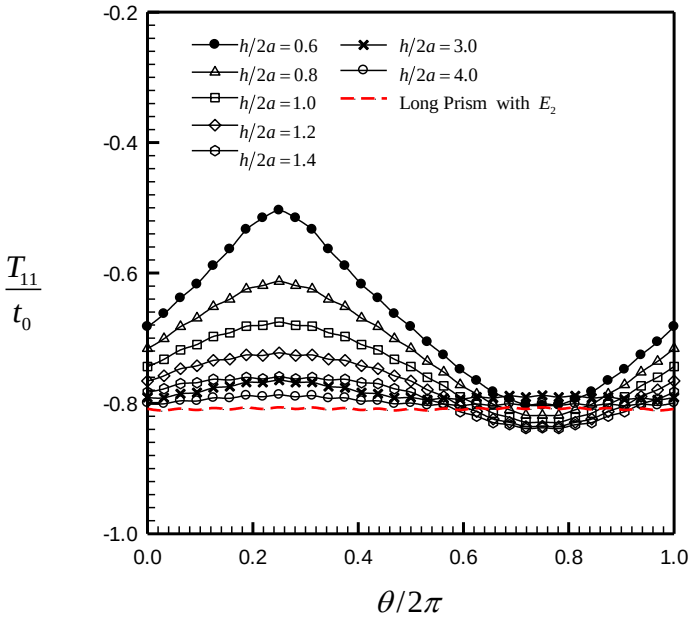

Figure 4.39 Normalized T-stress component T_{11} for penny-shaped crack in two-layer isotropic prism under uniform normal traction t_0 for $E_1/E_2 = 2$ and various values of $h/2a$

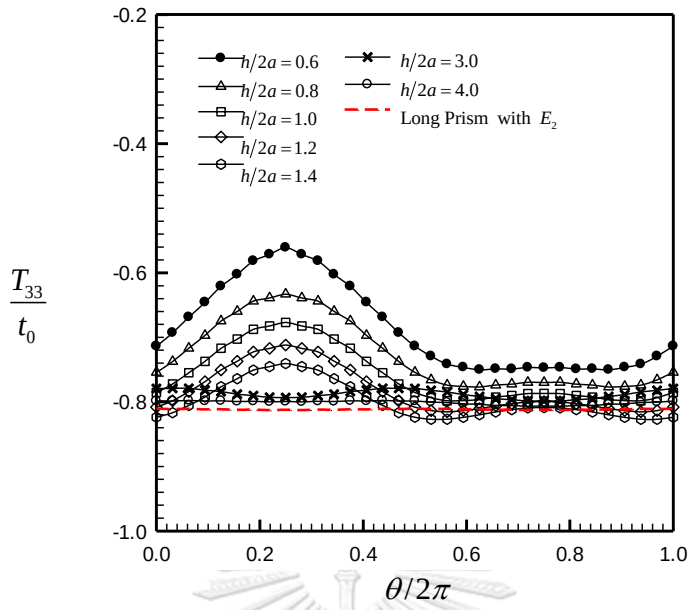

Figure 4.40 Normalized T-stress components T_{33} for penny-shaped crack in two-layer isotropic prism under uniform normal traction t_0 for $E_1/E_2 = 2$ and various values of $h/2a$

The influence of the distance h on the stress intensity factor and the T-stress components is also investigated for the different material contrast $E_1/E_2 = 0.5$. Results for the mode-I stress intensity factors and T-stress components are reported along the crack front in Figures 4.41-4.43 for various values of $h/2a$ (i.e., $h/2a = 0.6, 0.8, 1.0, 1.2, 1.4, 3.0, 4.0$). It is seen that when the crack is contained in a layer made of a stiffer material, both the stress intensity factor and the T-stress components decrease in magnitude as the normalized distance $h/2a$ increases. In addition, the locations along the crack front where the stress intensity factor and the T-stress components achieve their maximum and minimum values switch from the case of $E_1/E_2 = 2$. Similar to the previous case, it is observed that the presence of the material contrast shows the strong influence on both the variation and value of the two fracture data along the crack front when cracks are close to the material interface relative to the crack size and when the normalized distance $h/2a > 3$, such influence seems insignificant and the obtained solutions are nearly identical to the same crack embedded in a long prism without the material contrast.

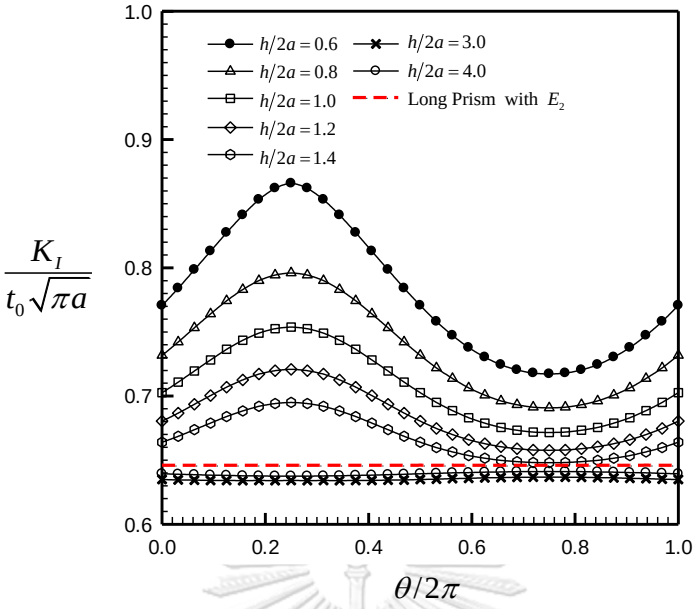

Figure 4.41 Normalized mode-I stress intensity factor for penny-shaped crack in two-layer isotropic prism under uniform normal traction t_0 for $E_1/E_2 = 0.5$ and various values of $h/2a$

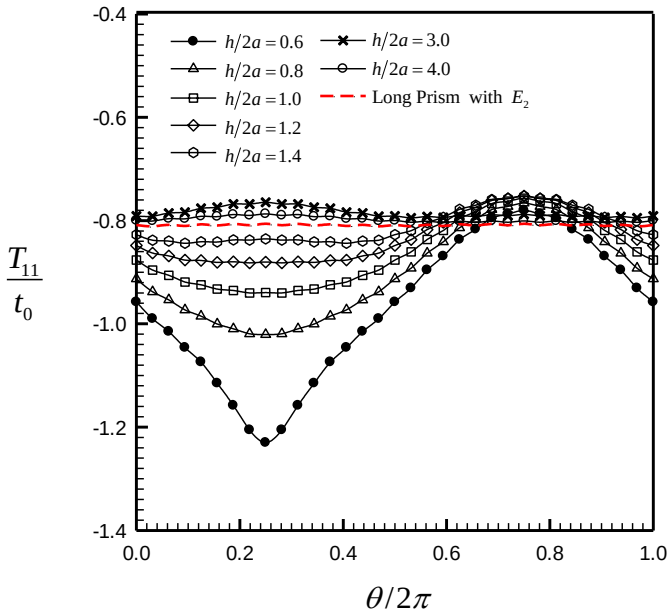

Figure 4.42 Normalized T-stress component T_{11} for penny-shaped crack in two-layer isotropic prism under uniform normal traction t_0 for $E_1/E_2 = 0.5$ and various values of $h/2a$

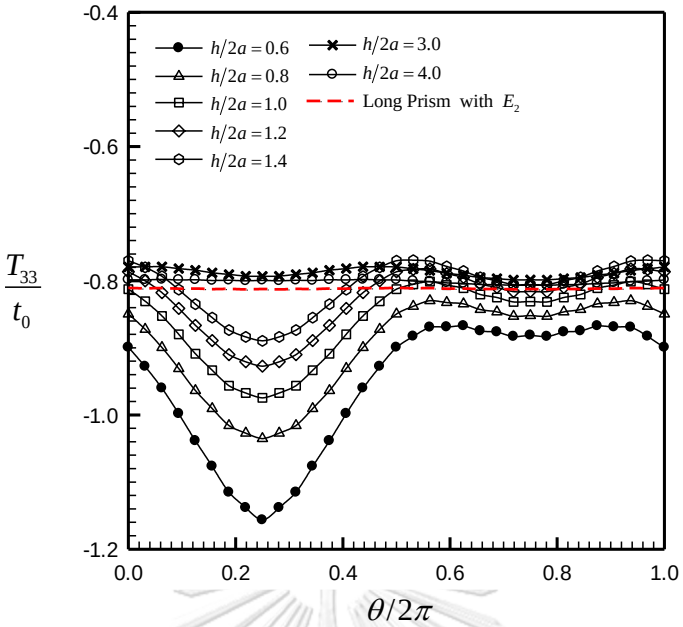

Figure 4.43 Normalized T-stress component T_{33} for penny-shaped crack in two-layer isotropic prism under uniform normal traction t_0 for $E_1/E_2 = 0.5$ and various values of $h/2a$

Results for the stress intensity factors and the T-stress components at certain points along the crack front (i.e., at $\theta = 0, \pi/2, 3\pi/2$) are also reported as a function of $h/2a$ in Figure 4.44-4.52 for four values of the material contrast (i.e., $E_1/E_2 = 0.1, 0.5, 2.0, 10.0$). It is seen that for small $h/2a$ (i.e., $h/2a < 2$), both the mode-I stress intensity factor and the T-stress components decrease in magnitude for $E_1/E_2 < 1$ and increase in magnitude for $E_1/E_2 > 1$ as the normalized distance $h/2a$ increases. Results also indicate that the rate of change of K_I, T_{11}, T_{33} with respect to $h/2a$ for the small value of $h/2a$ depends strongly on the material contrast E_1/E_2 ; for instance, the rate of decrease and increase in K_I, T_{11}, T_{33} increases as E_1/E_2 decreases and increases, respectively. This set of results also confirms that as the normalized distance $h/2a$ is larger than three the influence of the material contrast is insignificant.

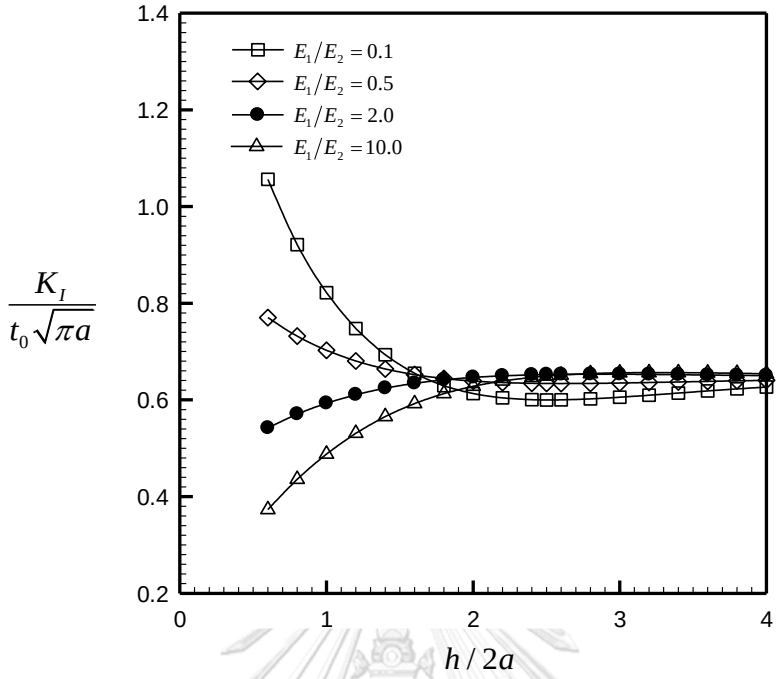

Figure 4.44 Normalized mode-I stress intensity factor at $\theta = 0$ for penny-shaped crack in two-layer isotropic prism under normal traction t_0

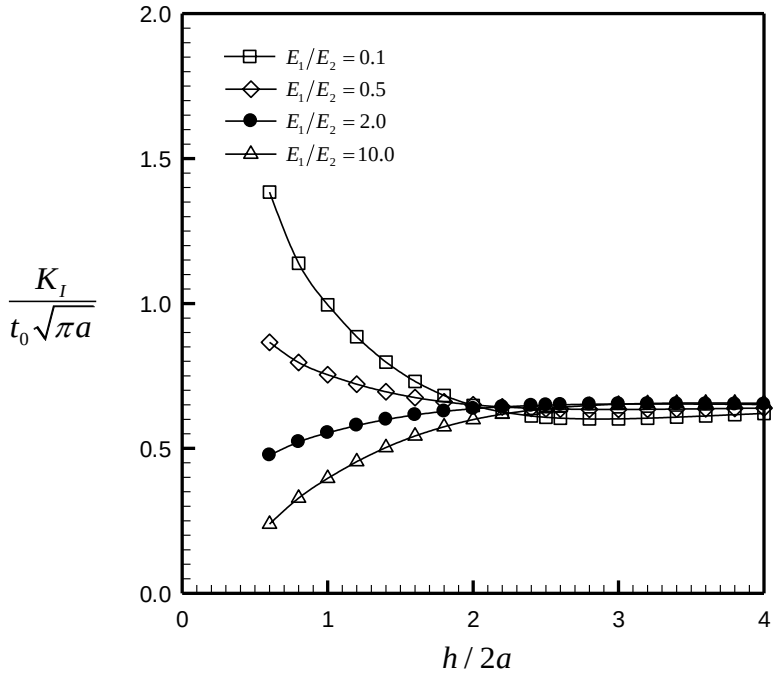

Figure 4.45 Normalized mode-I stress intensity factor at $\theta = \pi/2$ for penny-shaped crack in two-layer isotropic prism under normal traction t_0

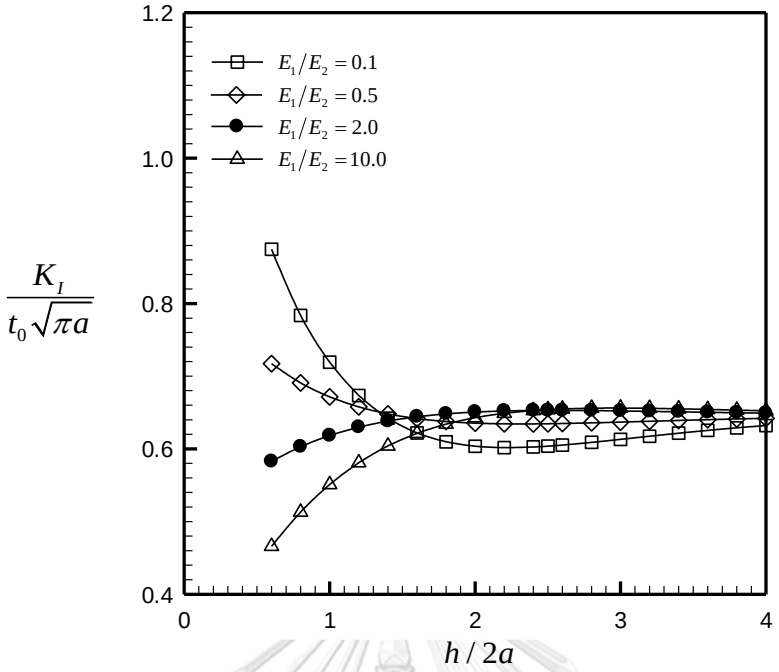

Figure 4.46 Normalized mode-I stress intensity factor at $\theta = 3\pi/2$ for penny-shaped crack in two-layer isotropic prism under normal traction t_0

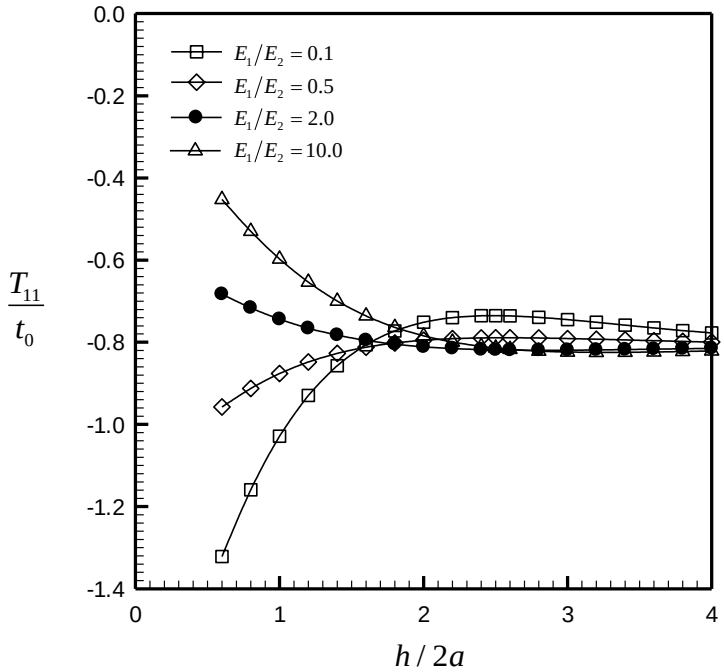

Figure 4.47 Normalized T-stress component T_{11} at $\theta = 0$ for penny-shaped crack in two-layer isotropic prism under normal traction t_0

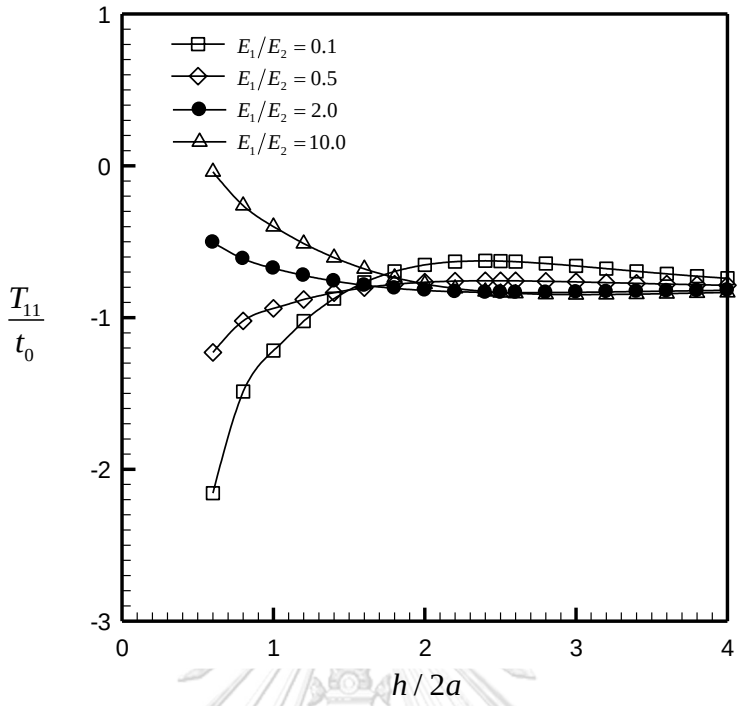

Figure 4.48 Normalized T-stress component T_{11} at $\theta = \pi/2$ for penny-shaped crack in two-layer isotropic prism under normal traction t_0

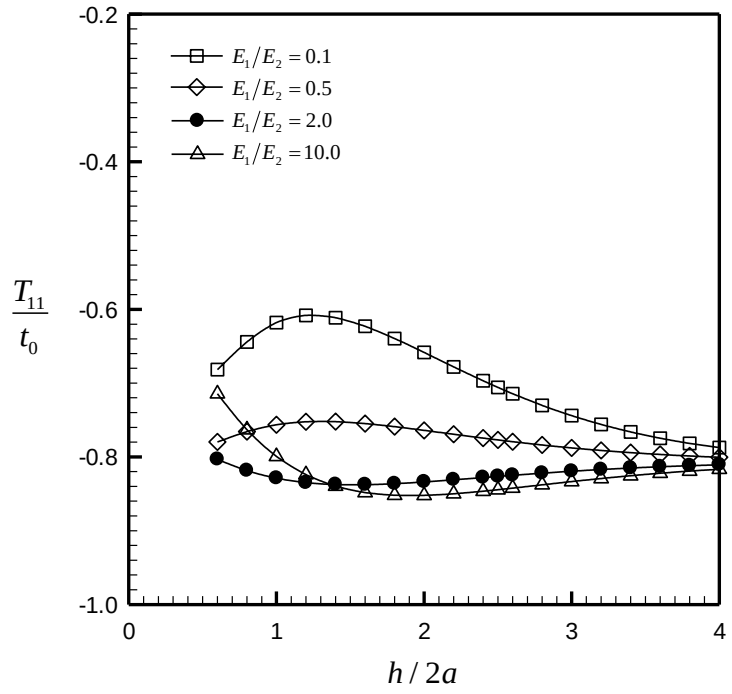

Figure 4.49 Normalized T-stress component T_{11} at $\theta = \pi/2$ for penny-shaped crack in two-layer isotropic prism under normal traction t_0

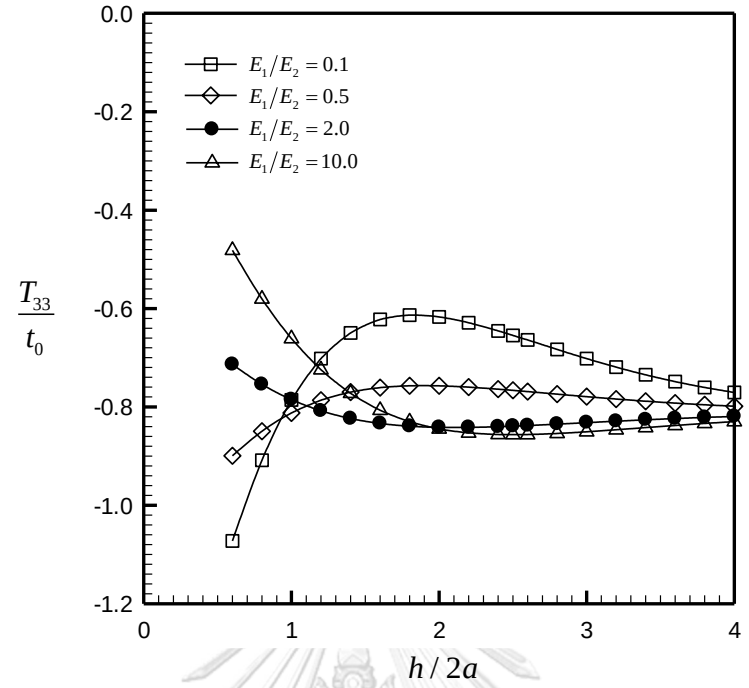

Figure 4.50 Normalized T-stress component $T_{33} = 0$ at $\theta = 0$ for penny-shaped crack in two-layer isotropic prism under normal traction t_0

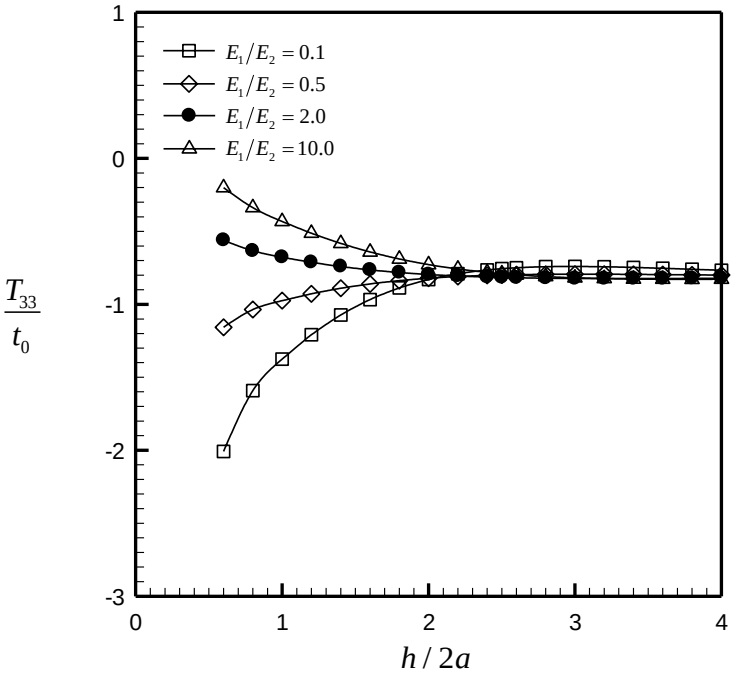

Figure 4.51 Normalized T-stress component $T_{33} = 0$ at $\theta = \pi/2$ for penny-shaped crack in two-layer isotropic prism under normal traction t_0

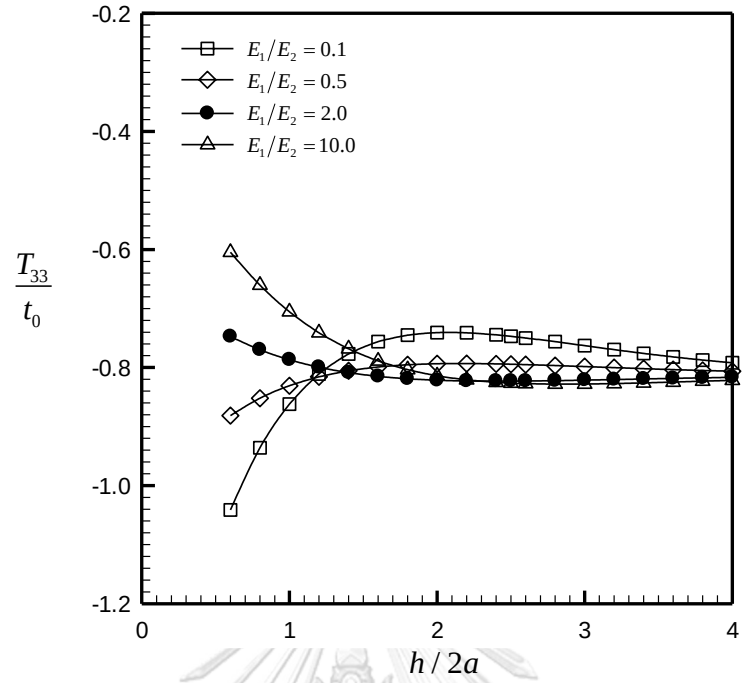

Figure 4.52 Normalized T-stress component $T_{33} = 0$ at $\theta = 3\pi / 2$ for penny-shaped crack in two-layer isotropic prism under normal traction t_0

CHAPTER 5
CONCLUSION AND REMARKS

An efficient and robust numerical technique, based upon the weakly singular boundary integral equation method, has been successfully implemented for the analysis of near interface or sub-interface cracks in multi-material finite bodies. The formulation has been established within a general framework allowing general data such as the body and crack geometries, general material anisotropy, general loading and boundary conditions to be treated. Both of the weakly-singular weak-form displacement and traction boundary integral equations is employed along with the domain decomposition technique to obtain a system of equations governing the unknown data on the ordinary boundary (i.e., the displacements and tractions), the material interfaces (i.e., the displacements and tractions) and the crack surface (i.e., jump in and sum of the crack-face displacements) for cracks in multi-material domains. The positive feature of the governing integral equations, in addition to its symmetry and applicability to treat material anisotropy and general crack configuration and loading conditions, is the weakly singular nature of all integral involved.

Standard Galerkin scheme has been utilized to discretize the resulting system of equations. The accuracy of the proposed technique has been further enhanced by exploiting special interpolations along the crack front to capture the dominant near-front field. In addition, all involved weakly singular and nearly singular integrals over pairs of elements resulting from the discretization have been carefully treated via the special numerical quadrature and the interpolation technique has been adopted to evaluate kernels for general anisotropic materials. Results from the present study have indicated that the integration of the special type of elements in the solution discretization significantly reduces the requirement of exploiting very fine mesh to accurately capture the near-front field. In addition, it also provides the direct means to post-process for the stress intensity factors from the jump in the crack-face displacement and for the T-stress components from the sum of crack-face displacement in the vicinity of the crack front. It is remarked also that the implemented technique yields highly accurate converged results as compared with

the reliable benchmark solutions and, in particular, the weak dependence on the level of mesh refinement has been observed for various scenarios.

Results from a parametric study have indicated that the contrast of the material stiffness and the distance between the crack and the material interface has the strong effect on both the magnitude and variation of the stress intensity factors and the T-stress components along the crack front. For examples considered, when the material containing no crack is stiffer than that containing crack, the stress intensity factors and the magnitude of the T-stress increase as the crack moves away from the material interface. In addition, as the material containing crack becomes stiffer than that containing no crack, both the stress intensity factor and the magnitude of the T-stress decreases monotonically. It can be concluded also that as the distance from the material interface is about three times greater than the size of the crack, the presence of the material contrast show the insignificant influence on the value and variation of the two fracture data along the crack front. This implies that the treatment of the material contrast in the modeling is essential only when cracks are relatively close to the material interface in comparison with the characteristic size of the crack.

Finally, it is remarked that the ingredients presented in this study provide an essential and sufficient basis for the extension of the technique to be capable of treating more complex multi-material domains such as cracks in piezoelectric layers.

REFERENCES

Anderson, T. L. (2005). Fracture mechanics : Fundamentals and applications 3rd edition. CRC Press: Boca Raton.

Barnett, D., and Asaro, R. (1972), The fracture mechanics of slit-like cracks in anisotropic elastic media. *Journal of the Mechanics and Physics of Solids,* **20**(6), 353-366.

Chang, J., and Wu, D. (2003), Calculation of mixed-mode stress intensity factors for a crack normal to a bimaterial interface using contour integrals. *Engineering Fracture Mechanics,* **70**(13), 1675-1695.

Chang, J., and Xu, J.-Q. (2007), The singular stress field and stress intensity factors of a crack terminating at a bimaterial interface. *International Journal of Mechanical Sciences,* **49**(7), 888-897.

Chen, C.-S., Tu, C.-H., and Yang, C.-C. (2010), Analysis of crack propagation path on the anisotropic bi-material rock. *Mathematical Problems in Engineering,* **2010**.

Chen, S., Wang, T., and Kao-Walter, S. (2003), A crack perpendicular to the bimaterial interface in finite solid. *International Journal of Solids and Structures*, **40**(11), 2731-2755.

Chen, S., Wang, T., and Kao-Walter, S. (2005), Finite boundary effects in problem of a crack perpendicular to and terminating at a bimaterial interface. *Acta Mechanica Sinica*, **21**(1), 56-64.

Hao, T. (2006), Exact solution of plane isolated crack normal to a bimaterial interface of infinite extent. *Acta Mechanica Sinica,* **22**(5), 455-468.

Huang, H., and Kardomateas, G. (2001), Mixed-mode stress intensity factors for cracks located at or parallel to the interface in bimaterial half planes. *International Journal of Solids and Structures,* **38**(21), 3719-3734.

Lee, J., Farris, T., and Keer, L. (1987), Stress intensity factors for cracks of arbitrary shape near an interfacial boundary. *Engineering Fracture Mechanics*, **27**(1), 27-41.

Li, S., and Mear, M. E. (1998), Singularity-reduced integral equations for displacement discontinuities in three-dimensional linear elastic media. *International journal of fracture,* **93**(1-4), 87-114.

Liu, X. (2015), Asymptotic fields for cracks terminating at bi-material interface with arbitrary angles.

Marsavina, L., and Sadowski, T. (2008), Asymptotic stress field at the tip of an inclined crack terminating to an interface. *Budownictwo i Architektura,* **2**, 111-124.

Noda, N.-A., Kouyama, T., and Kinoshita, Y. (2006), Stress intensity factors of an inclined elliptical crack near a bimaterial interface. *Engineering Fracture Mechanics,* **73**(10), 1292-1320.

Pham, T., Rungamornrat, J., Pansuk, W., and Sato, Y. (2015b), BIEs for modelling of discontinuities in linear multi-field half-space. *Boundary Elements and Other Mesh Reduction Methods XXXVIII,* **61**, 125.

Pham, T. N., Rungamornrat, J., Pansuk, W., and Sato, Y. (2015a). "Analysis of cracks in isotropic linear elastic half-space under various boundary conditions by weakly singular SGBEM". Proceedings of The 2015 World Congress on Advances in Structural Engineering and Mechanics (ASEM15), Incheon Korea, August 25-29

Profant, T., Ševeček, O., and Kotoul, M. (2008), Calculation of K-factor and T-stress for cracks in anisotropic bimaterials. *Engineering Fracture Mechanics,* **75**(12), 3707-3726.

Rungamornrat, J. (2006), Analysis of 3D cracks in anisotropic multi-material domain with weakly singular SGBEM. *Engineering analysis with boundary elements,* **30**(10), 834-846.

Rungamornrat, J., and Mear, M. E. (2008a), Weakly-singular, weak-form integral equations for cracks in three-dimensional anisotropic media. *International Journal of Solids and Structures,* **45**(5), 1283-1301.

Rungamornrat, J., and Mear, M. E. (2008b), A weakly-singular SGBEM for analysis of cracks in 3D anisotropic media. *Computer Methods in Applied Mechanics and Engineering,* **197**(49), 4319-4332.

Rungamornrat, J., and Pinitpanich, M (2016), T-stress solution of penny-shaped cracks in transversely isotropic elastic media. *Engineering Fracture Mechanics*, **158**, 194-208.

Rungamornrat, J., and Senjuntichai, T. (2009), Regularized boundary integral representations for dislocations and cracks in smart media. *Smart Materials and Structures*, **18**(7), 074010.

Ševeček, O., Kotoul, M., and Profant, T. (2012), Effect of higher order asymptotic terms on the competition between crack penetration and debond at a bimaterial interface between aligned orthotropic materials. *Engineering Fracture Mechanics,* **80**, 28-51.

Tu, C.-H., Dong, J.-J., Chen, C.-S., Ke, C.-C., Jhan, J.-Y., and Yu, H. J. (2013), Two-dimensional stress intensity factor analysis of cracks in anisotropic bimaterial. *Mathematical Problems in Engineering*, **2013**.

Williams, M. (1957), On the stress distribution at the base of a stationary crack.

Xiao, H., Yue, Z., Tham, L., and Lee, C. (2005), Analysis of elliptical cracks perpendicular to the interface of two joined transversely isotropic solids. *International journal of fracture*, **133**(4), 329-354.

Xiao, L. (1998). Symmetric weak-form integral equation method for three-dimensional fracture analysis. *Ph D. Dissertation*, The University of Texast Austin.

Xu, G. (2000), A variational boundary integral method for the analysis of three-dimensional cracks of arbitrary geometry in anisotropic elastic solids. *Journal of Applied Mechanics*, **67**(2), 403-408.

Yu, H., Wu, L., and Li, H. (2012), T-stress evaluations of an interface crack in the materials with complex interfaces. *International journal of fracture*, 1-13.

Yue, Z., Xiao, H., and Pan, E. (2007), Stress intensity factors of square crack inclined to interface of transversely isotropic bi-material. *Engineering analysis with boundary elements*, **31**(1), 50-65.

Zhou, Z., Xu, X., Leung, A. Y., and Huang, Y. (2013), Stress intensity factors and T-stress for an edge interface crack by symplectic expansion. *Engineering Fracture Mechanics*, **102**, 334-347.

APPENDIX

VITA

Pisit Watanavit was born on July 20, 1993 in Nakhon Ratchasima, Thailand,. He graduate bachelor of engineering of Civil engineering department from Kasetsart University. Next, he continue Master's degree at Chulalongkorn University for Structural engineering. He investigated in computational technique and fracture mechanic. he join the research unit and do the research under the guideline of Associate Professor Dr. Jaroon Rungamornrat and Assistant Profressor Watanachai Smittakorn.